

**FLEXIBLE MAGNETIC COMPOSITE FOR ANTENNA APPLICATIONS
IN RADIO FREQUENCY IDENTIFICATION (RFID)**

A Dissertation
Presented to
The Academic Faculty

by

Lara Jean Martin

In Partial Fulfillment
of the Requirements for the Degree
Doctor of Philosophy in Material Science and Engineering

Georgia Institute of Technology

April 2008

**FLEXIBLE MAGNETIC COMPOSITE FOR ANTENNA APPLICATIONS
IN RADIO FREQUENCY IDENTIFICATION (RFID)**

Approved by:

Dr. C. P. Wong, Advisor
School of Materials Science and
Engineering
Georgia Institute of Technology

Dr. Manos Tentzeris, Co-Advisor
School of Electrical and Computer
Engineering
Georgia Institute of Technology

Dr. Meilin Liu
School of Materials Science and
Engineering
Georgia Institute of Technology

Dr. Z. L. Wang
School of Materials Science and
Engineering
Georgia Institute of Technology

Dr. Hamid Garmestani
School of Materials Science and
Engineering
Georgia Institute of Technology

Date Approved: March 7, 2008

For Emily, Malcolm, and Tom

ACKNOWLEDGEMENTS

I express my sincere gratitude to Dr. C. P. Wong, whose support has not only enabled me to have a successful academic experience but also a successful career in industry. Dr. Wong encouraged me to pursue this degree, and without Dr. Wong, I may not be completing it. I am indebted to Dr. Wong for the active support has given me throughout the years and his contributions to making the quality of my life better. It is an honor to work for Dr. Wong.

I thank Dr. Manos Tentzeris for his first invitation to work with him and the work that has followed through collaboration with his research team. I appreciate the creativity of Dr. Tentzeris, which has been major inspiration for this work.

I thank Dr. Meilin Liu who has supported me throughout my academic career. Since my Master's degree, Dr. Meilin Liu has maintained contact and given me the opportunity to support the School of Materials Science and Engineering and Dr. C. P. Wong. I appreciate having Dr. Meilin Liu as one of my professors and also a committee member for both my Master's and Ph. D. degrees.

I thank Dr. Zhong Lin 'Z. L.' Wang as one of my professors and also as a committee member. I express my appreciation to work with Dr. Hamid Garmestani and having him as a committee member.

Special thanks go to some of my colleagues whose expertise has significantly affected this work. Thank you to my fellow Motorolan Dr. Soo Liam 'S. L.' Ooi. Thank you to Dr. Michael D. Hill from Trans-Tech and Hongjin Jiang from Dr. C. P. Wong's team at Georgia Tech. Also, thanks to Dr. Haiying Li at Motorola. Special thanks to Dr. Daniela

Staiculescu from Dr. Tentzeris' team for the work we have done together over the years and making our work extremely pleasant and successful. Thanks to Li Yang also from Dr. Tentzeris' team.

I acknowledge the support of others for making this work possible. Thanks to David Meyer at Motorola for his inputs, assistance, and willingness to work together. I appreciate several technical discussions with Dr. Nicholas 'Nick' Buris of Motorola and Dr. Jack Moon from Dr. C. P. Wong's team. Thanks to Justine Lu from Dr. C. P. Wong's team. Also, thanks to Barry Treadway of Trans-Tech and Scott Smith of Steward.

I give thanks to some others at Georgia Tech for their assistance. Thank you to Dr. Grace Li from Dr. C. P. Wong's team. Thanks to Susan Bowman for her guidance throughout my academic career.

I give special thanks to Jack Barreto who has supported me in both my academic and Motorola careers. My graduation and completion of this work would not be possible without Jack. Jack has made the quality of my life better, and I consider him not only a mentor, but also a friend.

I also give special thanks to John Frei who has been one of my best teachers for working in the real world of practical application. I use concepts and skills that John taught me, including both technical and interpersonal, in my livelihood, in my daily life, and throughout this thesis. John has been a mentor and generous in his willingness to pass some of his experience to me. It was an honor to work side-by-side with John at Motorola.

Thanks to Dr. Ann Ensley who has been a best friend since our early years at Georgia Tech. I greatly value Ann's friendship and generosity.

I dedicate this thesis to Emily, Malcolm, and Tom. I believe my accomplishments are rooted from my mother Emily Martin who truly believes and tells me that I can achieve anything I pursue. I also attribute my accomplishments to my father Malcolm Martin for his constant understanding and encouragement to take calculated risks. The final dedication is to Tom Swirbel for his unwavering love and support, in every goal and life aspiration, and who has forever positively affected my life.

TABLE OF CONTENTS

ACKNOWLEDGEMENTS	IV
LIST OF TABLES	XII
LIST OF FIGURES	XIV
NOMENCLATURE	XX
SUMMARY	XXV
CHAPTER I: INTRODUCTION	1
CHAPTER II: BACKGROUND	5
RFID SYSTEMS	5
RFID COMMUNICATION PRINCIPLES	6
NEAR FIELD COMMUNICATION AND MAGNETIC MATERIAL BENEFITS	7
FAR FIELD COMMUNICATION AND MAGNETIC MATERIAL BENEFITS	8
MATERIAL CONSIDERATIONS	9
<i>Magnetic Particles</i>	9
<i>Matrix Processability and Properties</i>	10
<i>Particle Size</i>	11
EXPERIMENTAL OBJECTIVE	12
CHAPTER III: CHARACTERIZATION OF MAGNETIC PARTICLES	14
INTRODUCTION	14
MATERIALS	14
<i>Magnetic Particles</i>	14
<i>NiZn Ferrite</i>	16

<i>BaCo Ferrite</i>	17
ANALYTICAL EQUIPMENT AND METHODS	23
<i>Scanning Electron Microscopy</i>	23
<i>Energy Dispersive Spectroscopy</i>	23
<i>X-ray Diffraction</i>	24
<i>Impedance Analysis</i>	24
RESULTS	25
<i>Morphology and Topography</i>	25
<i>Elemental Composition</i>	30
<i>Microstructure</i>	33
<i>Permittivity</i>	40
DISCUSSION	44
CONCLUSIONS	47
CHAPTER IV: FORMULATION AND CHARACTERIZATION OF MAGNETIC COMPOSITES	48
INTRODUCTION	48
MATERIALS AND METHODS	51
<i>Composite Formulation</i>	51
<i>Substrate Fabrication</i>	53
ANALYTICAL EQUIPMENT AND METHODS	56
<i>Impedance Analysis</i>	56
<i>Thermomechanical Analysis</i>	58
<i>Dynamic Mechanical Thermal Analysis</i>	58

RESULTS	59
<i>Effect of Ferrite Type</i>	59
Permittivity	59
Permeability	63
<i>Sources of Variation</i>	67
Variation of Measurements	67
Variation of Composite Formulations	73
<i>Effect of Coupling Agent</i>	76
Coefficient of Thermal Expansion	76
Complex Young's Modulus	77
Permittivity	79
Permeability	82
<i>Effect of Particle Size Distribution</i>	85
Permittivity and Permeability	85
DISCUSSION	99
CONCLUSIONS	102
CHAPTER V: ANTENNA EM SIMULATION AND EVALUATION	103
INTRODUCTION	103
MATERIALS AND CHARACTERIZATION	103
<i>Material Formulation</i>	103
<i>Substrate Preparation</i>	103
<i>Impedance Analysis</i>	104
<i>Applied Material Properties</i>	104

ANALYTICAL EQUIPMENT AND METHODS	107
<i>Figures of Merit</i>	107
<i>Measurement Methodology</i>	107
ANTENNA STRUCTURE AND DESIGN METHODOLOGY	111
<i>Benchmark Antenna Structure</i>	111
<i>Design Methodology</i>	111
<i>Final Antenna Designs</i>	112
RESULTS	115
<i>Reflection Coefficients</i>	115
<i>Radiation Patterns</i>	115
<i>Summary of Figures of Merit</i>	117
EFFECTS OF MATERIAL VARIATION ON ANTENNA PERFORMANCE	117
<i>Statistical Methodology and Objectives</i>	117
<i>Experiment</i>	123
<i>Final Statistical Models</i>	127
Resonant Frequency	127
Return Loss at 386 MHz	131
Maximum Gain at 386 MHz	136
Model Contour Plots	139
<i>Simulated Antenna Performance Capability</i>	140
DISCUSSION	149
<i>Radiation Pattern Comparisons</i>	149
<i>Antenna Performance Comparison</i>	149

<i>Antenna Performance Capability</i>	150
CONCLUSIONS	151
CHAPTER VI: CONCLUSIONS AND FUTURE RECOMMENDATIONS	153
APPENDIX A	158
AUTHOR’S AWARDS, HONORS, PATENTS, AND PUBLICATIONS	158
REFERENCES	163

LIST OF TABLES

TABLE 3.1: MATERIAL STRUCTURE INFORMATION OF FERRITE USED IN THIS WORK	15
TABLE 3.2: BATCH INFORMATION OF FERRITE PARTICLES USED IN THIS WORK	15
TABLE 3.3: COMPOSITION OF NiZn FERRITE USED IN THIS WORK BY COMPONENT	17
TABLE 3.4: COMPOSITION OF NiZn FERRITE USED IN THIS WORK BY ELEMENT	17
TABLE 3.5: CHEMICAL FORMULAE AND SOME CRYSTALLOGRAPHICAL PROPERTIES, INCLUDING LATTICE STRUCTURE DESCRIBED IN FIGURE 3.3, FOR THE M-, W-, Y-, AND Z- PHASES	21
TABLE 3.6: COMPOSITION OF BaCo FERRITE USED IN THIS WORK BY ELEMENT	21
TABLE 3.7: NOMINAL PARTICLE SIZE DISTRIBUTIONS FOR BATCHES OF BaCo FERRITE PARTICLES	22
TABLE 3.8: ATOMIC% DETECTED BY EDS FOR NiZn FERRITE AND DEVIATION FROM NOMINAL	32
TABLE 3.9: ATOMIC% DETECTED BY EDS FOR BaCo FERRITE AND DEVIATION FROM NOMINAL	32
TABLE 3.10: SAMPLE THICKNESSES OF PRESSED FERRITE POWDER DISKS FOR PERMITTIVITY MEASUREMENTS	41
TABLE 4.1: SUMMARY OF MEASUREMENTS FOR ϵ' , μ' , $\text{TAN}\delta_\epsilon$, AND $\text{TAN}\delta_\mu$ AT 400 MHz FOR COMPOSITES MADE FROM BaCo FERRITE 02L AND BaCo FERRITE 02	92
TABLE 4.2: SUMMARY OF P-VALUES FOR NONPARAMETRIC TESTS TO TEST DIFFERENCES IN ϵ' AT 400 MHz FOR TWO GROUPS OF PARTICLE SIZE DISTRIBUTIONS	95
TABLE 4.3: SUMMARY OF P-VALUES FOR NONPARAMETRIC TESTS TO TEST DIFFERENCES IN μ' AT 400 MHz FOR TWO GROUPS OF PARTICLE SIZE DISTRIBUTIONS	96
TABLE 4.4: SUMMARY OF P-VALUES FOR NONPARAMETRIC TESTS TO TEST DIFFERENCES IN $\text{TAN}\delta_\epsilon$ AT 400 MHz FOR TWO GROUPS OF PARTICLE SIZE DISTRIBUTIONS	97
TABLE 4.5: SUMMARY OF P-VALUES FOR NONPARAMETRIC TESTS TO TEST DIFFERENCES IN $\text{TAN}\delta_\mu$ AT 400 MHz FOR TWO GROUPS OF PARTICLE SIZE DISTRIBUTIONS	98
TABLE 5.1: MATERIAL PROPERTIES FOR PURE SILICONE	105
TABLE 5.2: INITIAL DESIGN RULES FOR PATCH ANTENNAS	111

TABLE 5.3: SUMMARY OF ANTENNA PERFORMANCE	117
TABLE 5.4: VARIATION ASSUMED FOR THE MATERIAL PROPERTIES AT 386 MHz	119
TABLE 5.5: DOE EXPERIMENTAL DESIGN	125
TABLE 5.6: RSM EXPERIMENTAL RUNS AND RESULTS FOR f_r , RL AT 386 MHz, AND MAX GAIN AT 386 MHz	125
TABLE 5.7: RSM CONFIRMATION RUNS AND RESULTS FOR f_r , RL AT 386 MHz, AND MAX GAIN AT 386 MHz	126
TABLE 5.8: RESULTS FOR f_r , RL AT 386 MHz, AND MAX GAIN AT 386 MHz ASSUMING $\tan\delta_\epsilon$ AND $\tan\delta_\mu$ EQUAL TO ZERO	126
TABLE 5.9: STATISTICAL DIAGNOSTICS FOR FIT OF THE f_r MODEL	128
TABLE 5.10: STATISTICAL SIGNIFICANCE OF PARAMETER ESTIMATES FOR THE f_r MODEL	128
TABLE 5.11: CONFIRMATION RESULTS FOR THE f_r MODEL	130
TABLE 5.12: STATISTICAL DIAGNOSTICS FOR FIT OF THE RL AT 386 MHz MODEL	132
TABLE 5.13: STATISTICAL SIGNIFICANCE OF PARAMETER ESTIMATES FOR THE RL AT 386 MHz MODEL	133
TABLE 5.14: CONFIRMATION RESULTS FOR THE RL AT 386 MHz MODEL	135
TABLE 5.15: STATISTICAL DIAGNOSTICS FOR FIT OF THE MAXIMUM GAIN AT 386 MHz MODEL	137
TABLE 5.16: STATISTICAL SIGNIFICANCE OF PARAMETER ESTIMATES FOR THE MAXIMUM GAIN AT 386 MHz MODEL	137
TABLE 5.17: CONFIRMATION RESULTS FOR THE MAXIMUM GAIN AT 386 MHz MODEL	139
TABLE 5.18: SUMMARY OF PROCESS SPECIFICATION LIMITS AND CAPABILITY METRICS FOR f_r , RL AT 386 MHz, AND MAXIMUM GAIN AT 386 MHz	146

LIST OF FIGURES

FIGURE 1.1: ESTIMATED VOLUME USAGE FOR SOME RFID LICENSED FREQUENCY BANDS	2
FIGURE 1.2: DEGREE OF FUNCTIONALITY VERSUS MEMORY SIZE FOR VARIOUS SYSTEMS DESCRIBED BY CORRESPONDING ISO OPERATING STANDARDS AND OPERATING FREQUENCIES	3
FIGURE 2.1: RFID SYSTEM COMPRISED OF A READER AND TRANSPONDER AND COUPLING BY RADIO WAVES TO TRANSFER DATA	5
FIGURE 2.2: (A) SCHEMATIC OF A TYPICAL READER-TRANSPONDER OPERATING BY NEAR FIELD COMMUNICATION PRINCIPLE, OR MUTUAL INDUCTANCE, AND (B) EQUIVALENT CIRCUIT	7
FIGURE 3.1: SCHEMATIC OF THE SPINEL STRUCTURE, SHOWING THE OXYGEN ANIONS FORMING TETRAHEDRAL AND OCTAHEDRAL SITES OCCUPIED BY A AND B CATIONS, RESPECTIVELY	16
FIGURE 3.2: TERNARY DIAGRAM OF BaO·MeO·Fe ₂ O ₃ SYSTEM IN MOLAR % (A) SHOWING THE COMPLETE SYSTEM, INCLUDING 0-100 MOLAR % FOR ALL THREE CONSTITUENTS AND (B) SHOWING ONLY TOP SECTION, INCLUDING 0-50 MOLAR % FOR BaO AND MeO AND 50-100 MOLAR % FOR Fe ₂ O ₃	19
FIGURE 3.3: CROSS-SECTION THROUGH A PLANE OF SYMMETRY OF THE “BLOCKS” M ₅ , W ₇ , AND Y ₆ , WHICH COMPRISE THE CRYSTAL STRUCTURE OF THE M-, W-, Y-, AND Z-PHASES OF THE TERNARY BaO·MeO·Fe ₂ O ₃ SYSTEM	20
FIGURE 3.4: SEM IMAGES AT 500X MAGNIFICATION OF MAGNETIC PARTICLES IN SE MODE	26
FIGURE 3.5: SEM IMAGES AT 1500X MAGNIFICATION OF MAGNETIC PARTICLES IN SE MODE	27
FIGURE 3.6: SEM IMAGES AT 1500X MAGNIFICATION OF MAGNETIC PARTICLES IN BSE MODE	28
FIGURE 3.7: SEM IMAGES AT 5000X MAGNIFICATION OF MAGNETIC PARTICLES IN SE MODE	29
FIGURE 3.8: EDS OF MAGNETIC PARTICLES	31
FIGURE 3.9: XRD PATTERN FOR NiZn FERRITE 01	34
FIGURE 3.10: PCPDFWIN CARD 08-2034 (NiZn)Fe ₂ O ₄ SHOWING 2θ PEAK POSITIONS	35

FIGURE 3.11: XRD PATTERN FOR BaCo FERRITE 01	36
FIGURE 3.12: XRD PATTERN FOR BaCo FERRITE 02	37
FIGURE 3.13: XRD PATTERN FOR BaCo FERRITE 04	38
FIGURE 3.14: PCPDFWIN CARD 19-0097 Ba ₃ Co ₂ Fe ₂₄ O ₄₁ SHOWING 2θ PEAK POSITIONS	39
FIGURE 3.15: ε' VERSUS FREQUENCY FOR FERRITE POWDERS PRESSED INTO DISK SHAPES	42
FIGURE 3.16: ε'' VERSUS FREQUENCY FOR FERRITE POWDERS PRESSED INTO DISK SHAPES	42
FIGURE 3.17: TANδ _ε VERSUS FREQUENCY FOR FERRITE POWDERS PRESSED INTO DISK SHAPES	43
FIGURE 4.1: PROPOSED MECHANISM TO INCREASE RESISTIVITY AT PARTICLE-MATRIX INTERFACE BY SILANE FUNCTIONAL GROUP	49
FIGURE 4.2: GENERALIZED ILLUSTRATION OF FERRITE PARTICLE FUNCTIONALIZED BY SAM MOLECULES, WHERE X = Si FROM THE SILANE FUNCTION GROUP	50
FIGURE 4.3: VINYLTRIETHOXY SILANE CHEMICAL STRUCTURE	52
FIGURE 4.4: EQUIPMENT AND SETUP USED IN THE COMPOSITE FORMULATION PROCESS	52
FIGURE 4.5: CRITICAL DIMENSIONS OF MOLD DESIGN ON 305 X 457 X 1.6 MM FR-4 PANEL INCLUDING ONE 180 X 180 MM AND FOUR 77 X 77 MM CAVITIES WITH SURROUNDING RESERVOIRS	55
FIGURE 4.6: CURING TEMPERATURE PROFILE, INCLUDING SET POINT AND ACTUAL TEMPERATURES FOR A TYPICAL CURING PROCESS	55
FIGURE 4.7: SHAPE OF DISK WITH A CONCENTRIC CIRCULAR CENTER CUT FOR μ* MEASUREMENTS WITH OUTER DIAMETER (a), INNER DIAMETER (b), AND THICKNESS (h)	57
FIGURE 4.8: PICTURE OF ACTUAL SAMPLES FOR IMPEDANCE ANALYSIS	57
FIGURE 4.9: ε' VERSUS FREQUENCY FOR COMPOSITES COMPRISED OF DIFFERENT FERRITE TYPES	61
FIGURE 4.10: ε'' VERSUS FREQUENCY FOR COMPOSITES COMPRISED OF DIFFERENT FERRITE TYPES	61
FIGURE 4.11: TANδ _ε VERSUS FREQUENCY FOR COMPOSITES COMPRISED OF DIFFERENT FERRITE TYPES	62

FIGURE 4.12: μ' VERSUS FREQUENCY FOR COMPOSITES COMPRISED OF DIFFERENT FERRITE TYPES	65
FIGURE 4.13: μ'' VERSUS FREQUENCY FOR COMPOSITES COMPRISED OF DIFFERENT FERRITE TYPES	65
FIGURE 4.14: $TAN\delta_{\mu}$ VERSUS FREQUENCY FOR COMPOSITES COMPRISED OF DIFFERENT FERRITE TYPES	66
FIGURE 4.15: ϵ' VERSUS FREQUENCY FOR MEASUREMENTS OF BaCo FERRITE 02L COMPOSITE FORMULATIONS	68
FIGURE 4.16: ϵ' VERSUS FREQUENCY FOR MEASUREMENTS OF BaCo FERRITE 04 COMPOSITE FORMULATIONS	68
FIGURE 4.17: μ' VERSUS FREQUENCY FOR MEASUREMENTS OF BaCo FERRITE 02L COMPOSITE FORMULATIONS	69
FIGURE 4.18: μ' VERSUS FREQUENCY FOR MEASUREMENTS OF BaCo FERRITE 04 COMPOSITE FORMULATIONS	69
FIGURE 4.19: $TAN\delta_{\epsilon}$ VERSUS FREQUENCY FOR MEASUREMENTS OF BaCo FERRITE 02L COMPOSITE FORMULATIONS	71
FIGURE 4.20: $TAN\delta_{\epsilon}$ VERSUS FREQUENCY FOR MEASUREMENTS OF BaCo FERRITE 04 COMPOSITE FORMULATIONS	71
FIGURE 4.21: $TAN\delta_{\mu}$ VERSUS FREQUENCY FOR MEASUREMENTS OF BaCo FERRITE 02L COMPOSITE FORMULATIONS	72
FIGURE 4.22: $TAN\delta_{\mu}$ VERSUS FREQUENCY FOR MEASUREMENTS OF BaCo FERRITE 04 COMPOSITE FORMULATIONS	72
FIGURE 4.23: ϵ' VERSUS FREQUENCY FOR DIFFERENT FORMULATIONS OF COMPOSITES MADE FROM BaCo FERRITE 02L AND BaCo FERRITE 04	74
FIGURE 4.24: μ' VERSUS FREQUENCY FOR DIFFERENT FORMULATIONS OF COMPOSITES MADE FROM BaCo FERRITE 02L AND BaCo FERRITE 04	74
FIGURE 4.25: $TAN\delta_{\epsilon}$ VERSUS FREQUENCY FOR DIFFERENT FORMULATIONS OF COMPOSITES MADE FROM BaCo FERRITE 02L AND BaCo FERRITE 04	75
FIGURE 4.26: $TAN\delta_{\mu}$ VERSUS FREQUENCY FOR DIFFERENT FORMULATIONS OF COMPOSITES MADE FROM BaCo FERRITE 02L AND BaCo FERRITE 04	75

FIGURE 4.27: CTE VALUES FOR SAMPLES INCLUDING COMPOSITES COMPRISED OF NiZn FERRITE 01 AS EXPERIMENTAL CONTROL, FABRICATED WITH DIFFERENT COUPLING AGENT TREATMENTS 0.5 WT% SILANE, 1.0 WT% SILANE, AND 1.5 WT% SILANE	76
FIGURE 4.28: E' VALUES FOR THE COMPOSITES NiZn FERRITE 01 AS THE EXPERIMENTAL CONTROL, 0.5 WT% SILANE, 1.0 WT% SILANE, AND 1.5 WT% SILANE	78
FIGURE 4.29: E'' VALUES FOR THE COMPOSITES NiZn FERRITE 01 AS THE EXPERIMENTAL CONTROL, 0.5 WT% SILANE, 1.0 WT% SILANE, AND 1.5 WT% SILANE	78
FIGURE 4.30: ϵ' VERSUS FREQUENCY FOR DIFFERENT COUPLING AGENT TREATMENTS	80
FIGURE 4.31: ϵ'' VERSUS FREQUENCY FOR DIFFERENT COUPLING AGENT TREATMENTS	80
FIGURE 4.32: $TAN\delta_{\epsilon}$ VERSUS FREQUENCY FOR DIFFERENT COUPLING AGENT TREATMENTS	81
FIGURE 4.33: ϵ' VERSUS FREQUENCY FOR DIFFERENT COUPLING AGENT TREATMENTS	83
FIGURE 4.34: ϵ'' VERSUS FREQUENCY FOR DIFFERENT COUPLING AGENT TREATMENTS	83
FIGURE 4.35: $TAN\delta_{\mu}$ VERSUS FREQUENCY FOR DIFFERENT COUPLING AGENT TREATMENTS	84
FIGURE 4.36: ϵ' VERSUS FREQUENCY FOR COMPOSITES MADE FROM BaCo FERRITE 02L AND BaCo FERRITE 02	90
FIGURE 4.37: μ' VERSUS FREQUENCY FOR COMPOSITES MADE FROM BaCo FERRITE 02L AND BaCo FERRITE 02	90
FIGURE 4.38: $TAN\delta_{\epsilon}$ VERSUS FREQUENCY FOR COMPOSITES MADE FROM BaCo FERRITE 02L AND BaCo FERRITE 02	91
FIGURE 4.39: $TAN\delta_{\mu}$ VERSUS FREQUENCY FOR COMPOSITES MADE FROM BaCo FERRITE 02L AND BaCo FERRITE 02	91
FIGURE 4.40: STATISTICAL ANALYSIS OF ϵ' AT 400 MHZ FOR COMPOSITES MADE FROM BaCo FERRITE 02L AND BaCo FERRITE 02	93
FIGURE 4.41: STATISTICAL ANALYSIS OF μ' AT 400 MHZ FOR COMPOSITES MADE FROM BaCo FERRITE 02L AND BaCo FERRITE 02	93
FIGURE 4.42: STATISTICAL ANALYSIS OF $TAN\delta_{\epsilon}$ AT 400 MHZ FOR COMPOSITES MADE FROM BaCo FERRITE 02L AND BaCo FERRITE 02	94
FIGURE 4.43: STATISTICAL ANALYSIS OF $TAN\delta_{\mu}$ AT 400 MHZ FOR COMPOSITES MADE FROM BaCo FERRITE 02L AND BaCo FERRITE 02	94
FIGURE 5.1: VALUES OF ϵ_r AND $TAN\delta_{\epsilon}$ OBTAINED IN A SINGLE MEASUREMENT	106

FIGURE 5.2: VALUES OF μ_r AND $\tan\delta_\mu$ OBTAINED IN A SINGLE MEASUREMENT	106
FIGURE 5.3: PICTURE OF THE MEASUREMENT SETUP FOR OBTAINING S_{11} VALUES	108
FIGURE 5.4: PICTURES OF MEASUREMENT SETUP FOR OBTAINING 2-D RADIATION PATTERN IN ANECHOIC CHAMBER	109
FIGURE 5.5: RADIATION PATTERN MEASUREMENT CONVENTION FOR ϕ AND θ	110
FIGURE 5.6: DIMENSIONS OF PATCH ANTENNA DESIGN ON PURE SILICONE SUBSTRATE (NOT DRAWN TO SCALE)	113
FIGURE 5.7: DIMENSIONS OF PATCH ANTENNA DESIGN ON MAGNETIC COMPOSITE SUBSTRATE (NOT DRAWN TO SCALE)	113
FIGURE 5.8: LAYOUT OF THE PROTOTYPE MAGNETIC COMPOSITE ANTENNA, UTILIZING THE MOLD DESIGN ON THE 305 X 457 X 1.6 MM FR-4 PANEL ILLUSTRATED IN FIGURE 4.5	114
FIGURE 5.9: PHOTOGRAPH OF PROTOTYPE PATCH ANTENNA ON MAGNETIC COMPOSITE SUBSTRATE	114
FIGURE 5.10: S_{11} VERSUS FREQUENCY FOR PATCH ANTENNAS ON MAGNETIC COMPOSITE AS MEASURED, MAGNETIC COMPOSITE AS SIMULATED, AND PURE SILICONE AS SIMULATED	115
FIGURE 5.11: RADIATION PATTERN AND ADJUSTED GAIN AT $\phi = 0^\circ$ AND 90° FOR PATCH ANTENNA ON SILICONE AS SIMULATED, TAKEN AT f_r	116
FIGURE 5.12: RADIATION PATTERN AND ADJUSTED GAIN AT $\phi = 0^\circ$ AND 90° FOR PATCH ANTENNA ON MAGNETIC COMPOSITE AS MEASURED AND SIMULATED, TAKEN AT f_r	116
FIGURE 5.13: DIMENSIONS OF PATCH ANTENNA DESIGN ON MAGNETIC COMPOSITE SUBSTRATE FOR THE VARIATION STUDY (NOT DRAWN TO SCALE)	120
FIGURE 5.14: METHODOLOGY FOR DEVELOPING STATISTICAL MODELS	122
FIGURE 5.15: PLOT OF ACTUAL VERSUS PREDICTED VALUES FOR THE f_r MODEL	127
FIGURE 5.16: HISTOGRAM OF RESIDUALS FOR THE f_r MODEL	129
FIGURE 5.17: PLOT OF RESIDUALS VERSUS PREDICTED VALUES FOR THE f_r MODEL	130
FIGURE 5.18: PLOT OF ACTUAL VERSUS PREDICTED VALUES FOR THE RL AT 386 MHz MODEL	131
FIGURE 5.19: HISTOGRAM OF RESIDUALS FOR THE RL AT 386 MHz MODEL	134
FIGURE 5.20: PLOT OF RESIDUALS VERSUS PREDICTED VALUES FOR THE RL AT 386 MHz MODEL	134

FIGURE 5.21: PLOT OF ACTUAL VERSUS PREDICTED VALUES FOR THE MAXIMUM GAIN AT 386 MHz MODEL	136
FIGURE 5.22: HISTOGRAM OF RESIDUALS FOR THE MAXIMUM GAIN AT 386 MHz MODEL	138
FIGURE 5.23: PLOT OF RESIDUALS VERSUS PREDICTED VALUES FOR THE MAXIMUM GAIN AT 386 MHz MODEL	139
FIGURE 5.24: CONTOUR PLOTS OF THE FINAL STATISTICAL MODELS FOR (A) f_r , (B) RL AT 386 MHz, AND (C) MAXIMUM GAIN AT 386 MHz	140
FIGURE 5.25: HISTOGRAMS OF 20,000 TRIALS FOR THE INPUTS (A) ϵ' AND (B) μ' THAT WERE GENERATED IN THE MONTE CARLO SIMULATION	144
FIGURE 5.26: HISTOGRAMS OF 20,000 TRIALS FOR THE OUTPUTS (A) f_r , (B) RL AT 386 MHz, AND (C) MAXIMUM GAIN AT 386 MHz	145
FIGURE 5.27: SENSITIVITY CHARTS SHOWING CONTRIBUTION TO VARIANCE OF ϵ' AND μ' FOR THE OUTPUTS (A) f_r , (B) RL AT 386 MHz, AND (C) MAXIMUM GAIN AT 386 MHz	147
FIGURE 5.28: S_{11} VERSUS FREQUENCY FOR PATCH ANTENNA ON MAGNETIC COMPOSITE ASSUMING THE ORIGINAL DESIGN WITH NO LOSS ($\text{TAN}\delta_\epsilon$ AND $\text{TAN}\delta_\mu$ EQUAL TO ZERO), THE ORIGINAL DESIGN WITH ACTUAL LOSS ($\text{TAN}\delta_\epsilon$ AND $\text{TAN}\delta_\mu$ EQUAL TO MEASURED VALUES), AND THE RETUNED DESIGN WITH NO LOSS ($\text{TAN}\delta_\epsilon$ AND $\text{TAN}\delta_\mu$ EQUAL TO ZERO)	148

NOMENCLATURE

2-D	two-dimensional
2θ	diffraction angle in x-ray diffraction
α	Type I risk assumed in statistical analysis
ϵ^*	complex permittivity
ϵ'	real part of complex permittivity; equivalent to ϵ_r ; dielectric constant
ϵ''	imaginary part of complex permittivity; dielectric loss
ϵ_{eff}	effective permittivity
ϵ_r	relative permittivity; equivalent to ϵ'
θ	angle rotated away from the x-axis in antenna radiation measurements
λ	wavelength
μ^*	complex permeability
μ'	real part of complex permeability; equivalent to μ_r ; magnetic property
μ''	imaginary part of complex permeability; magnetic loss
μ_{eff}	effective permeability
μm	micrometer
μ_r	relative permeability
σ	standard deviation
ϕ	angle rotated away from the z-axis in antenna radiation measurements
Ω	ohm
a	outer diameter of material shape required for μ^* measurement

AC	alternating current
Al	aluminum
atomic%	atomic percent
Auto-ID	automatic identification
b	inner diameter of material shape required for μ^* measurement
Ba	barium
BSE	backscattered electron
BW	bandwidth
c	speed of light
C	carbon
cm	centimeter
cm ³	cubic centimeter
Co	cobalt
Co ₂ Z	Z-phase BaCo ferrite of the ternary BaO·CoO·Fe ₂ O ₃ system; same as Z-phase Co hexaferrite
CST	full name CST Microwave Studio; EM simulation software
CTE	coefficient of thermal expansion
Cu	copper
d	inset dimension
DoD	Department of Defense
DOE	design of experiment
DTMA	dynamic mechanical thermal analysis or dynamic mechanical thermal analyzer

E*	complex Young's modulus
E'	real part of complex Young's modulus; storage modulus
E''	imaginary part of complex Young's modulus; loss modulus
EAS	electronic article surveillance
EDAX	manufacturer of EDS equipment
EDS	energy dispersive spectroscopy or energy dispersive spectroscope
EM	electromagnetic
ESCA	electron spectroscopy for chemical analysis
ESEM	environmental scanning electron microscope
Fe	iron
FEI	manufacturer of SEM equipment
FEM	finite element method
f_r	resonant frequency
FR-4	flame retardant laminate made from woven glass fiber impregnated with epoxy resin
g	gram
GHz	gigahertz
GSE	gaseous secondary electron
h	substrate thickness
HF	high frequency
HFSS	full name Ansoft HFSS; EM simulation software supplied by Ansoft
Hg	mercury
IEEE	Institute of Electrical and Electronics Engineers

ISO	International Standards Organization
k	number of factors in a factorial design of experiment
kHz	kilohertz
kPa	kilopascal
LCL	lower confidence limit
LF	low frequency
LSL	lower specification limit
max	maximum
Mg	magnesium
MHz	megahertz
mm	millimeter
MPD	multi-purpose diffractometer
Ni	nickel
O	oxygen
OFTA	Office of the Telecommunications Authority
OS	operating system
oz	ounce
PCB	printed circuit board
Q	circuit Q or component Q; quality factor
RF	radio frequency
RFID	radio frequency identification
RL	return loss
rpm	rotations per minute

RSM	response surface methodology
S_{11}	reflection coefficient
SAM	self assembled monolayer
SE	secondary electron
SEM	scanning electron microscopy or scanning electron microscope
$\tan\delta_\epsilon$	dielectric loss tangent; equivalent to ϵ''/ϵ'
$\tan\delta_\mu$	magnetic loss tangent; equivalent to μ''/μ'
TGA	thermogravimetric analysis or thermogravimetric analyzer
TMA	thermomechanical analysis or thermomechanical analyzer
TMP	Technical Machine Products; manufacturer of PCB press equipment
U.S.	United States
UCL	upper confidence limit
UHF	ultra high frequency
UPC	universal product code
USL	upper specification limit
vol%	volume percent
w	microstrip width
wt%	weight percent
XRD	X-ray diffraction or X-ray diffractometer
Z_0	characteristic impedance
Zn	zinc

SUMMARY

This work includes formulation of mechanically flexible magnetic composites and application to a quarter-wavelength microstrip patch antenna benchmarking structure operating in the lower UHF spectrum (~300-500 MHz) to investigate capability for miniaturization. A key challenge is to introduce sufficiently low magnetic loss for successful application. Particles of NiZn ferrite and BaCo ferrite, also known as Co_2Z , were characterized. Flexible magnetic composites comprised of 40 vol% NiZn ferrite or BaCo ferrite particles in a silicone matrix were formulated. Effects of treating the particles with silane in the formulation process were not detectable, but larger particle size showed to increase ϵ^* and μ^* . By comparing ϵ^* and μ^* of the composites, BaCo ferrite was selected for the antenna application. Antennas on the developed magnetic composite and pure silicone substrates were electromagnetically modeled in a full-wave FEM EM solver. A prototype of the antenna on the magnetic composite was fabricated. Good agreement between the simulated and measured results was found. Comparison of the antennas on the magnetic composite versus the pure silicone substrate showed miniaturization capability of 2.4X and performance differences of increased bandwidth, reduced Q, and reduced gain. A key finding of this study is that a small amount of permeability ($\mu_r \sim 2.5$) can provide relatively substantial capability for miniaturization, while sufficiently low magnetic loss can be introduced for successful application at the targeted operating frequency. The magnetic composite showed the capability to fulfill this balance and to be a feasible option for RFID applications in the lower UHF spectrum.

CHAPTER I: INTRODUCTION

Radio Frequency Identification (RFID) is one of several types of automatic identification (Auto-ID) procedures. Other types of Auto-ID procedures include barcode systems, biometrics such as voice identification and fingerprinting, and contact-based smart cards. The difference between RFID and other types of Auto-ID is that information between reader and the item to be identified is carried by radio waves. In RFID systems, a reader communicates to a transponder with an attached microchip that carries data and, in some systems, processes data [1].

RFID systems exist to provide information about people, animals, goods, and products in transit. Examples of RFID uses include automated toll paying applications (such as Florida Turnpike Sun Pass), credit card payments (such as Exxon Mobil Speedpass), metro passes, live stock keeping, cargo tracking, library book management, and industry supply chain, to name a few [2]. RFID is commonly compared to its predecessors, namely barcode systems and contact-based smart cards. Compared to barcode systems, RFID systems provide information transfer that does not depend on line-of-sight, higher volume read rates, higher information transfer accuracy, more storage capacity for information about the identified item (e.g., information beyond only a universal product code (UPC)), and, in some systems, the ability to process information on the identified item [3]. In the case of contact-based smart cards, RFID circumvents the disadvantages related to faulty contacting, such as dirt, unidirectional insertion, and processing time [1].

The use of RFID depends on the frequency bands licensed by governments. Operating frequencies licensed by governments include 135 kHz, 13.56 MHz, 868 MHz (Europe), 915

MHz (U.S.), 2.45 GHz, and 5.8 GHz among others [4, 5]. For these frequencies, the bands are low frequency (LF) that includes 135 kHz, high frequency (HF) that includes 13.56 MHz, ultra high frequency (UHF) that includes 868 and 915 MHz, and microwave that includes 2.45 and 5.8 GHz. The estimated volume usage for some licensed frequency bands is shown in Figure 1.1.

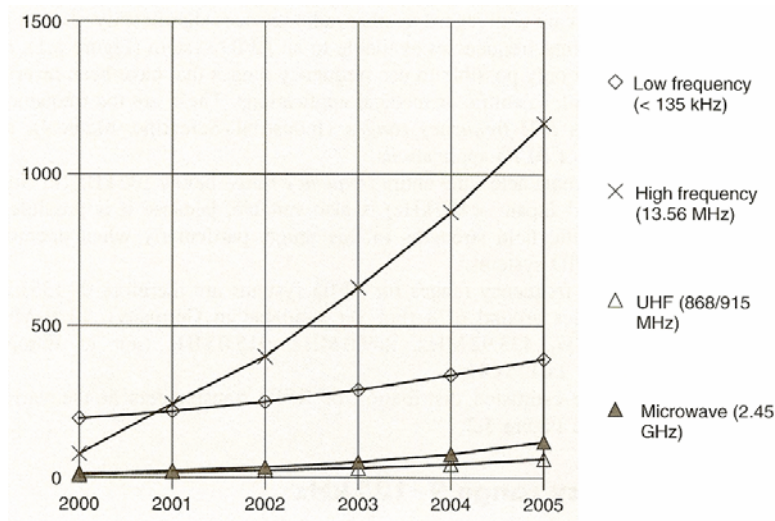


Figure 1.1: Estimated volume usage for some RFID licensed frequency bands [4]

The degree of functionality is a factor used to classify RFID into low-end, mid-range, and high-end systems. The low-end is typically used for applications in which little information is required, supporting read-only and read-write functionality, and can replace the functionality of barcode systems. An example of a low-end system is electronic article surveillance (EAS) systems. For mid-range, memory size ranges from a few bytes to over 100 Kbytes and typical functionality can include anticollision of multiple transponders in an interrogation zone and authentication procedures between transponder and reader. High-

range systems have capability of further functionality for more complex encryption and authentication algorithms, enabled by smart card operating system (OS) and, for most complex and highest security, the addition of a cryptographic coprocessor. Figure 1.2 shows the degree of functionality versus memory size for various systems that are described by their corresponding International Standards Organization (ISO) operating standards and operating frequencies.

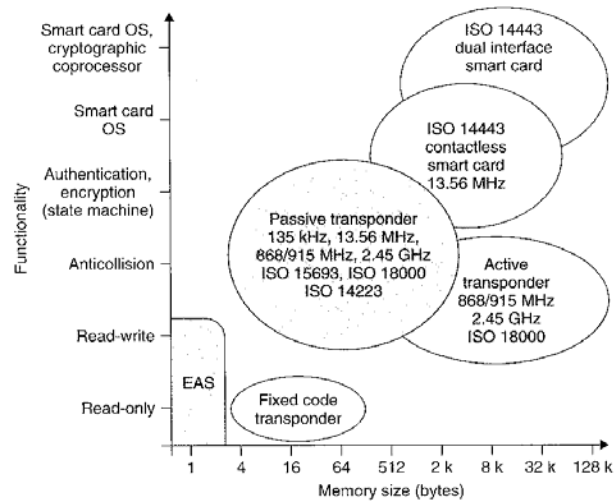


Figure 1.2: Degree of functionality versus memory size for various systems described by corresponding ISO operating standards and operating frequencies [6]

With the significant advantages provided by RFID, its inception has recently prompted mandates from large public enterprises and government agencies. Most notably, Wal-Mart and the United States Department of Defense (DoD) have issued commercial mandates, calling for their suppliers to adopt RFID in order to continue doing business with them [7]. These mandates require both rapid technological advancement and the adoption of strategic policies and standards. In March 2005, a technology exhibition and policy primer for members of U.S. Congress and their staffs was held in Washington D.C. Representation

from companies including Motorola, Oracle, and IBM demonstrated new RFID technologies [8]. Past commercial mandates have proven effective in uniting consumers and vendors toward a common goal and driving technological and policy development, and research firms predicted that the Wal-Mart mandate was going to be difficult for suppliers to achieve by the end-of-year 2006 timeline based on the state of the technology [9].

One critical area that can be addressed for significant development of RFID technology is application of magnetic materials in transponder antenna designs. Three-dimensional RFID transponder antennas that utilize wound coil inductors do make use of magnetic cores, but magnetic materials for two-dimensional embedded planar antennas, with embedded inductors or other planar shapes, have not yet been successfully realized for standard use. As their three-dimensional counterparts, two-dimensional embedded antennas can reap the benefits from magnetic materials, namely, miniaturization and improved system performance.

With miniaturization and improved performance of the transponder antennas, RFID system design can be more flexible. Two examples of increased system flexibility include a wider selection of transponder antenna form factors to attach to the tagged items and the ability to tune system performance to accommodate electromagnetic absorption and interference occurring from tagged item material compositions and surrounding media [10, 11]. In many embedded inductor and antenna studies, it can often be cited that objectives of miniaturization and improved performance are limited by availability of materials that possess the required properties [12, 13, 14]. Studies on magnetic materials that may provide cost effective solutions and are compatible with current standard processing techniques and design requirements are needed for such materials to find their way into standard RFID antenna designs.

CHAPTER II: BACKGROUND

RFID Systems

An RFID system is comprised of two components, a reader and transponder, which are designed to operate at a particular frequency. The reader, or interrogator, is the data capture device, and the transponder is located on the object to be identified and contains the data to be retrieved. Figure 2.1 describes the RFID system comprised of a reader and transponder and the coupling by radio waves to transfer data.

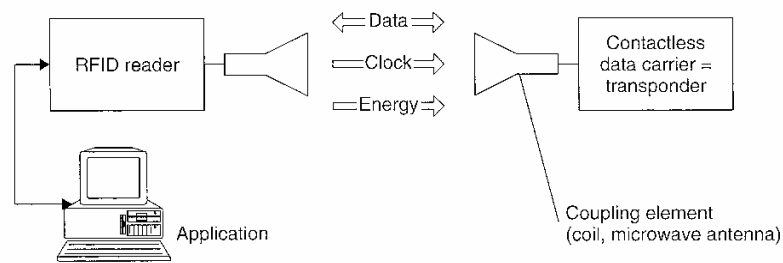


Figure 2.1: RFID system comprised of a reader and transponder and coupling by radio waves to transfer data [1]

For considerations of implementation, the most important differentiation criteria for RFID systems are operating frequency, physical coupling method, and read range of the system [6]. Operating frequency bands include LF (e.g. 135 kHz), HF (e.g. 13.56 MHz), UHF (e.g. 433, 868, and 915 MHz), and microwave (e.g. 2.45 and 5.8 GHz) [15]. Physical coupling methods include electric, magnetic, and electromagnetic. Achievable read range of systems can vary from a few millimeters to more than 15 meters. Classification of long-

range systems applies to read range greater than 1 meter and systems at operating frequencies of 868/915 MHz and higher [16].

RFID transponders, also known as tags, may be classified as either passive or active. Passive tags do not require a power source for operation but instead depend on energy from the reader for operation. Active tags include a battery for operation, enabling longer read ranges and more complex information exchange, and richer processing capabilities. Most popular today are passive tags [17].

RFID Communication Principles

Communication between the reader and transponder antennas for RFID systems in the HF (e.g. 13.56 MHz) and UHF (e.g. 433, 868, and 915 MHz) bands operates by two different principles, namely, near field and far field radiation, respectively [18, 19, 20]. The near field is the area at the antenna to the point in space for which the primary magnetic field exists and before which the electromagnetic field has fully formed. The far field is the area after which the electromagnetic field has formed and is separated from the antenna. The transition from the near field to the far field condition is defined by the operating frequency wavelength divided by 2π (that is, $\lambda/2\pi$). For example in the case of the HF bands, this condition gives RFID antennas at 13.56 MHz ($\lambda = 22.1$ m) operating by near field radiation, or mutual inductance, an insurmountable read range of 3.5 m. In the case of UHF RFID antennas at 433 MHz ($\lambda = 69$ cm) operating by far field radiation, or electromagnetic backscattering coupling, the maximum range is limited by field strength that decreases from the source antenna [21].

The RFID passive transponder antennas are usually different shapes that are driven by function. For the HF band, the antenna is typically an inductor, either as a wound coil or a

planar spiral form on a substrate. For the UHF band, the antenna is typically a planar form of various geometrical shapes [22, 23].

Near Field Communication and Magnetic Material Benefits

For the RFID operation in the HF band, a schematic of the near field communication principle and the corresponding equivalent circuit are given by Figure 2.2. The area labeled “antenna coil” shown in the left side of the schematic of Figure 2.2 (b) is the equivalent circuit for the inductor.

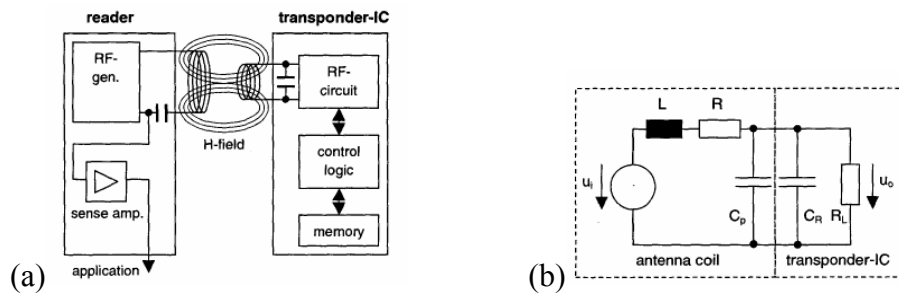


Figure 2.2: (a) Schematic of a typical reader-transponder operating by near field communication principle, or mutual inductance, and (b) equivalent circuit [22]

For HF RFID antennas, a widely used inductor design is a wound coil with magnetic core design that is commonly encased in a glass or plastic housing [23]. Smart cards and smart labels are planar spiral antennas, which do not include any magnetic materials [24]. A common, widely held motive for integration of magnetic material in wound coil inductors is for miniaturization and increasing component Q (also known as Q -factor and quality factor), the ratio of energy stored to energy lost, in order to achieve longer read ranges. Adding the higher relative permeability (μ_r) material into the design enables increased inductance, which requires smaller geometries (that is, miniaturization) to adjust the resonant frequency back up

to the targeted operating frequency and enables higher component Q and longer read ranges [25, 26]. Only limited work has been done to use magnetic materials in planar spiral antennas to achieve these benefits [12, 27, 28, 29, 30].

For embedded spiral inductor and antenna designs that operate in the HF band, the challenge is adding magnetic materials that incur low magnetic loss during operation. If lossy magnetic materials are added to the designs, effectively lower component Q can result [25]. Lower component Q results in lower circuit Q [31]. For this reason, a common figure of merit used to measure antenna performance is circuit Q, also known as selectivity, equal to resonant frequency (f_r) divided by bandwidth (BW), as shown by (2.1) [32].

$$Q = \frac{f_r}{BW} \quad (2.1)$$

For embedded spiral inductor and antenna designs, increasing circuit Q and miniaturization are interdependent results that can work together for improved performance.

Far Field Communication and Magnetic Material Benefits

For the RFID operation in the UHF band, transfer of data between reader and transponder is different compared to that shown in Figure 2.2 (a), as these higher frequencies operate by the far field communication principle. Additionally, instead of an inductive coil, the antenna operating in the UHF band is typically a planar antenna of various geometrical shapes [33]. For these high frequencies, a rectangular microstrip antenna, which is essentially a thin strip of rectangular metal on top of a dielectric substrate, is a simple and compact antenna design and demonstrates benefits that magnetic materials can provide. Although these antennas provide the advantage of compact, low profile designs, they possess the operational disadvantage of very narrow BW and, hence very high circuit Q, or selectivity, described by (2.1), making their use prohibitive [34]. A particular microstrip

antenna that has found practical use is the quarter wavelength microstrip [35]. The length of the quarter wavelength microstrip is $\lambda/4$ as shown by (2.2) [36].

$$\frac{\lambda}{4} = \frac{c}{4f_r \sqrt{\mu_{\text{eff}} \epsilon_{\text{eff}}}} \quad (2.2)$$

where λ is wavelength, c is speed of light, f_r is resonant frequency, μ_{eff} is effective permeability, and ϵ_{eff} is effective permittivity.

From (2.2), increasing permeability by the addition of a magnetic material to a quarter wavelength microstrip antenna decreases the required length for resonance, enabling miniaturization. Further, use of magnetic material has shown to decrease circuit Q by addition of some magnetic loss, but only limited amount of magnetic loss can be added to achieve successful microstrip designs [37, 38, 39]. Only limited work has been done to use magnetic materials in microstrip antennas to achieve these benefits [36, 37, 38, 39,40]. For microstrip antenna designs, decreasing circuit Q and miniaturization are interdependent results that can work together for improved performance.

Specific to the UHF band, antenna designs have included placement of the antenna structure directly on ferrite substrates. Beyond the obvious results of highly brittle substrates with no flexibility, the designs are limited by the dimensions and type of ferrite substrates that can be obtained [13].

Material Considerations

Magnetic Particles

When selecting a magnetic material, it is important to match its type with the targeted application. The magnetic materials introduce internal magnetic losses, with the two main sources being hysteresis loss and eddy current loss. These two types of internal loss are

inherent to some degree in every magnetic material and thus unavoidable. The permeability of magnetic materials is a function of frequency and usually decreases to a very small value at the upper end of the operating range. The permeability eventually approaches that of air and becomes “invisible” to the circuit [25]. The origin of the magnetism, including ferromagnetism, antiferromagnetism, ferrimagnetism, diamagnetism, and paramagnetism, of magnetic materials, can be referenced in literature [41, 42].

Ferrites are ferrimagnetic oxides and useful in radio frequency (RF) design. Ferrites widely used in alternating current (AC) applications are soft, as opposed to hard, magnetic materials with high resistivity, which resists occurrence of magnetic loss due to eddy currents [43]. For RF designs, the chosen magnetic material must provide sufficiently low loss at the targeted operating frequency. If designs implement materials for which magnetic loss is too high, a successful design can not be achieved.

The general classes of ferrite are based on their structure and termed the cubic ferrites, hexagonal ferrites, and rare earth ferrites, also known as garnets. In addition to their similarity in structure, the classes of ferrites are also similar in their applicability [43, 44]. For this work, a cubic ferrite, NiZn ferrite, and a hexagonal ferrite, BaCo ferrite, were targeted as the magnetic particles.

Matrix Processability and Properties

To be accepted and practical for standard use in antenna designs, the magnetic materials should be compatible with current standard processes, in particular, low temperature processability. For the limited work that has been done on low temperature processability, magnetic composite materials containing magnetic particles have been formulated, reducing processing temperatures to those required by the matrix. The processing temperatures

required are still as high as 300°C and more to achieve targeted magnetic properties, or the magnetic composites require high solvent volumes for thick film processing [12, 28, 29, 30, 45]. Magnetic composites comprised of ferrite particles in an organic matrix still show potential of providing the magnetic properties to miniaturize and improve embedded antenna performance while requiring low processing temperatures. For embedded capacitor and conductive adhesive applications, composites comprised of particles in an organic matrix have been shown to provide benefits of low processing temperatures [46, 47, 48]. In addition to processability, the composite for this work should be mechanically flexible and provide sufficient adhesion to copper. To achieve low temperature processability and these properties, silicone as the composite matrix was targeted for this work.

Particle Size

There has recently been work on composites comprised of nano-size particles in organic matrices for embedded capacitor and conductive adhesive applications. In these applications, both bulk properties of the particles and the particle-matrix interfaces contribute to the overall bulk properties of the composites. In fact, there has been focus on the particle-matrix interface, because the interface has shown to provide a dominate effect on the bulk composite properties [46, 47, 48].

For typical magnetic materials, nano-size particles and grains can be single domain, because single magnetic domains can be thermodynamically favored at this scale [49]. Typical domain wall widths are on the order of 100 nm, which implies that, in this case, a particle or grain smaller than 100 nm can not accommodate the domain and contains only a single domain [49]. Additionally, it is well known that decreasing particle and grain size increases coercivity of magnetic materials [49, 50]. The effect of decreasing grain size with

increasing hysteresis loss has been shown on a rare earth ferrite with average grain size range of 0.7-5.3 μm [51]. Formulation of nano-size ferrite particles has been established with sizes of about 5-50 nm [12, 29, 30, 52, 53, 54, 55, 56, 57]. Additionally, formulations of magnetic composites comprised of ferrite nano-size particles in an organic matrix have been demonstrated [53, 57]. However, these works do not include data on permeability loss [12, 29, 30, 52, 53, 54, 55, 56, 57].

Average grain size of a ferrite can also affect its value of μ_r . The effect of increasing average grain size with increasing value for μ_r has been shown for Ni ferrite, NiZn ferrite, and a rare earth ferrite with approximate average grain sizes range of about 1-10 μm [51, 58].

The targeted embedded antenna application for this work requires sufficiently low magnetic loss for performance, while having μ_r values that are large enough for miniaturization capability. For this work, the approach was to use particle sizes that were sufficiently large in order to not disrupt the magnetic domains, therefore avoiding undesirable hysteresis loss and preserving μ_r values. Thereafter, the effect of particle size distribution on the electromagnetic properties could be investigated.

Experimental Objective

For the limited work that has been done to use magnetic materials in both embedded spiral and other planar antenna designs, fundamental material science research is rarely coupled with system-level performance results. Further understanding on the impact that magnetic materials have on system level designs can drive more areas of research on structure-property relationships and translation of fundamental material mechanisms to material performance that occurs at the system level. Further, demonstrating system-level

performance can benefit electrical engineers who would have interest in using these materials in their system designs.

The objective of this work is to fundamentally understand magnetic composites with respect to mechanisms of magnetic properties and loss and determine system-level effects in antenna designs that operate in the lower UHF band (~300-500 MHz). Specific system-level effects to be considered include capabilities to miniaturize and effect on circuit Q. The main challenge for observing the capabilities to miniaturize and the effect on circuit Q is achieving sufficiently low magnetic loss in the magnetic composites in order for the antenna structure to successfully operate. Additionally, the studied magnetic material should be compatible with current standard processing techniques and design rules as well as provide sufficient adhesion and mechanical flexibility.

CHAPTER III: CHARACTERIZATION OF MAGNETIC PARTICLES

Introduction

The magnetic materials used in this work were ferrites supplied in a powder form by different manufacturers. The manufacturers provided some information on structure and properties of their ferrite powder material. The purpose of this chapter is to characterize the ferrite powders in terms of structure and permittivity, which is a critical material property for antenna applications. For the structure investigation, the morphology, topography, and particle size were characterized by SEM, and EDS was used to determine elemental composition. XRD was used to investigate microstructure. Impedance analysis was applied to measure complex permittivity ϵ^* , from which ϵ' , ϵ'' , and $\tan\delta_\epsilon$ were obtained, as a function of frequency. Finally, the results of these characterizations were compared to the specifications provided by the manufacturers and applicability to antenna design is discussed.

Materials

Magnetic Particles

The magnetic materials targeted for this work were a cubic ferrite and a hexagonal ferrite. Both of these materials were supplied as powders by separate manufacturers. The cubic ferrite was a NiZn ferrite, specifically with a spinel lattice structure. It can be cited that NiZn ferrites can have applicability up to 200 MHz [59]. The hexagonal ferrite was a BaCo ferrite, specifically Z-phase composition and referred to as Z-phase Co hexaferrite, which showed applicability to the lower UHF spectrum (~300-500 MHz) [60]. The densities as provided by the manufacturers for the NiZn ferrite and BaCo ferrite are 5.20 and 5.33 g/cm³,

respectively. The latter was confirmed to agree with literature as the X-ray density [61].

This information for the two ferrites is summarized in Table 3.1.

Table 3.1: Material Structure Information of Ferrite Used in this Work

Type	Lattice Structure	Density
NiZn Ferrite	Spinel	5.20 g/cm ³
BaCo Ferrite (Z-phase)	Hexagonal	5.33 g/cm ³

There were four batches of the ferrites used in this work, one batch of the NiZn ferrite and three batches of the BaCo ferrite. The NiZn ferrite was supplied by Steward and the BaCo ferrite by Trans-Tech. This information on the batches and additional information on the manufacturer part number, batch code, and identification of the batches for the purpose of this work are summarized in Table 3.2. Hereafter in this work, the batches will be identified as NiZn Ferrite 01, BaCo Ferrite 01, BaCo Ferrite 02, and BaCo Ferrite 04, corresponding to that shown in Table 3.2.

Table 3.2: Batch Information of Ferrite Particles Used in this Work

Type	Manufacturer	Part Number	Batch Code	Identification
NiZn Ferrite	Steward	72599	070707	NiZn Ferrite 01
BaCo Ferrite	Trans-Tech	C ₀₂ Z	962452	BaCo Ferrite 01
BaCo Ferrite	Trans-Tech	C ₀₂ Z	A016265	BaCo Ferrite 02
BaCo Ferrite	Trans-Tech	C ₀₂ Z	A017699	BaCo Ferrite 04

NiZn Ferrite

The NiZn ferrite used in this work is a cubic ferrite with spinel lattice structure. Cubic ferrites have the general formula $MO \cdot Fe_2O_3$, where M is a divalent ion, such as Mn^{2+} , Ni^{2+} , Fe^{2+} , Co^{2+} , Mg^{2+} , or Zn^{2+} . The cubic ferrites crystallize as spinel structure but can also crystalline in the inverse spinel structure [62, 63]. The cubic ferrites can be tailored to specific applications. As an example, because $NiFe_2O_4$ and $ZnFe_2O_4$ are soluble in each other, solid solutions of NiZn ferrite can produce properties that are intermediate of the parent compounds. The spinel structure is shown in Figure 3.1, including descriptions of the normal and inverse spinel structures.

NiZn ferrite is generally formulated by solid state reaction at $1250^\circ C$ of pellets of 0.5 NiO and 0.5 ZnO with Fe_2O_3 [64]. The composition of the NiZn ferrite used in this work was specified by the manufacturer by the components NiO, ZnO, CuO, and Fe_2O_3 . Table 3.3 shows the specified composition as a range in wt%, the nominal wt%, and the converted atomic%. Table 3.4 shows the composition as atomic% for the elements.

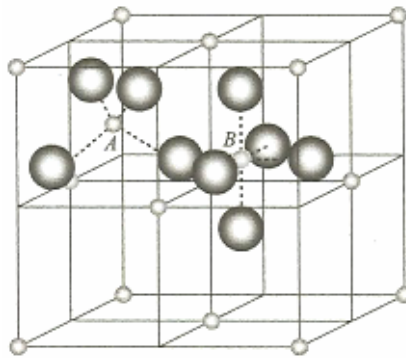


Figure 3.1: Schematic of the spinel structure, showing the oxygen anions forming tetrahedral and octahedral sites occupied by A and B cations, respectively. Not all sites are occupied by cations. In normal spinel structure, the divalent M^{2+} ions are all on A sites, and Fe^{3+} ions occupy B sites. In inverse spinel structure, the divalent ions occupy some of the B sites, and the Fe^{3+} ions are divided equally between A and B sites [65].

Table 3.3: Composition of NiZn Ferrite Used in this Work by Component

Component	Specified Wt%	Nominal Wt%	Nominal Atomic%
NiO	17-23	20	31.6
ZnO	8-14	11	15.9
CuO	1-4	2.5	3.7
Fe ₂ O ₃	63-69	66	48.8
Total	89-110	99.5	100.0

Table 3.4: Composition of NiZn Ferrite Used in this Work by Element

Element	Nominal Atomic%
O	57.0
Fe	28.2
Ni	9.1
Cu	1.1
Zn	4.6
Total	100.0

BaCo Ferrite

The Z-phase BaCo ferrite used in this work has the chemical formula Ba₃Co₂Fe₂₄O₄₁. In 1956-57, Philips introduced this material as one of several new compounds in the ternary BaO·MeO·Fe₂O₃ system [66]. For this ternary system, Me represents one of the small divalent ions Mn, Fe, Co, Ni, Zn, or Mg, or a mixture of them. A more complete list of the new compounds cited for the system around this time includes ferrocube MeFe₂O₄ (S),

ferroxdure $\text{BaFe}_{12}\text{O}_{19}$ (M), BaFe_2O_4 (B), $\text{BaMe}_2\text{Fe}_{16}\text{O}_{27}$ (W), $\text{Ba}_2\text{Me}_2\text{Fe}_{12}\text{O}_{22}$ (Y), and $\text{Ba}_3\text{Me}_2\text{Fe}_{24}\text{O}_{41}$ (Z). The $\text{BaO}\cdot\text{MeO}\cdot\text{Fe}_2\text{O}_3$ system and these compounds are shown in the ternary diagram in Figure 3.2. With substitution of Me with one of the small divalent ions, the specific compound may be represented by its letter symbol (S, W, Y, or Z) and the substituted divalent ion with its stoichiometry; therefore, the Z-phase BaCo ferrite used in this work may be properly referred to as Co_2Z [66].

The compounds, or phases, of the $\text{BaO}\cdot\text{MeO}\cdot\text{Fe}_2\text{O}_3$ ternary system are formulated by heating specific mixtures of these oxides for a given time at 1200-1400°C to obtain a sintered ceramic product [66]. For this work, the Z-phase BaCo ferrite particles were formulated by blending oxides and carbonates of the stoichiometric composition and heat treating to bring about solid state reaction between 1150-1300°C to form single phase Co_2Z material. The formulation process included the early materials hematite Fe_2O_3 and magnetite Fe_3O_4 , with magnetite Fe_3O_4 having spinel lattice structure. Thereafter, intermediate products M- and Y-phases, both having hexagonal lattice structure, were formed. Then, the M- and Y-phases were converted to the final Z-phase BaCo ferrite. Following the solid state reaction of the powder, the material was pressed into granules, sintered above 1200°C, and crushed to achieve the desired particle size. Similar to the conversion process from M- and Y-phases for obtaining Z-phase, it is cited that W-phase can be obtained from the conversion of M-phase [66]. Additionally, it is cited that care must be taken to ensure the conversion process is taken to completion in order to obtain the pure targeted final phase. If the conversion process is not taken to completion, small quantities of the earlier reactant phase can remain as an impurity in the targeted final phase [66, 67].

The hexagonal lattice structures for the M-, W-, Y-, and Z-phases of the BaO·MeO·Fe₂O₃ ternary system are relatively complex and can be referenced in literature. The hexagonal lattice structures for these phases are described in Figure 3.3. Table 3.5 summarizes the chemical formulae and some crystallographical properties, including the lattice structure described in Figure 3.3, for the M-, W-, Y-, and Z-phases.

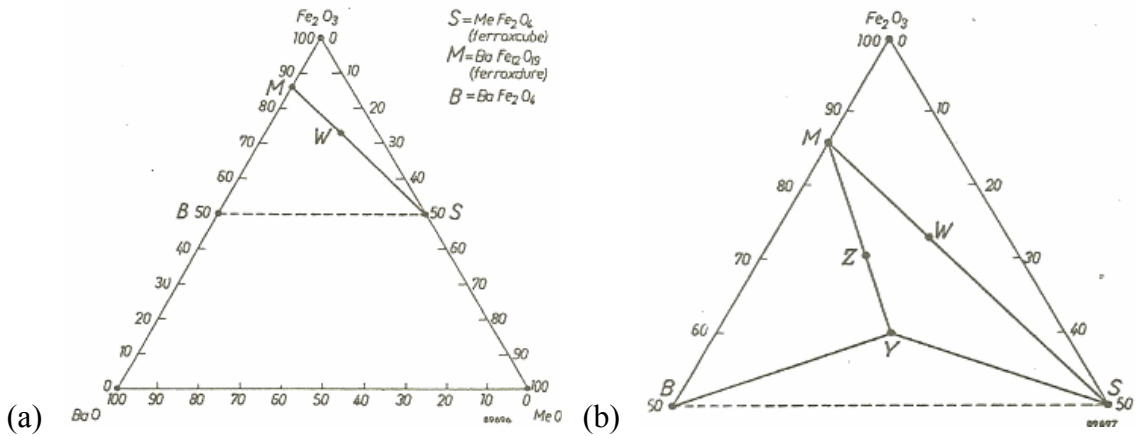


Figure 3.2: Ternary diagram of BaO·MeO·Fe₂O₃ system in molar % (a) showing the complete system, including 0-100 molar % for all three constituents and (b) showing only top section, including 0-50 molar % for BaO and MeO and 50-100 molar % for Fe₂O₃. The symbol Me represents one of the divalent ions Mn, Fe, Co, Ni, Zn, or Mg or a mixture of them. The materials ferroxcube MeFe₂O₄ (S), ferroxdure BaFe₁₂O₁₉ (M), BaFe₂O₄ (B), BaMe₂Fe₁₆O₂₇ (W), Ba₂Me₂Fe₁₂O₂₂ (Y), and Ba₃Me₂Fe₂₄O₄₁ (Z) are shown as points on the triangle [66].

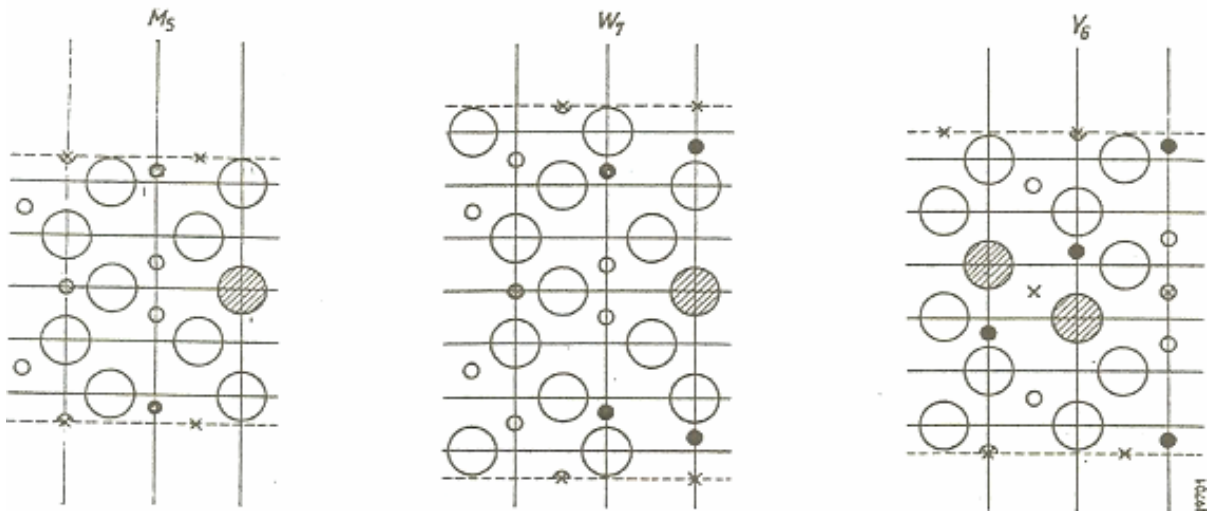


Figure 3.3: Cross-section through a plane of symmetry of the “blocks” M_5 , W_7 , and Y_6 , which comprise the crystal structure of the M-, W-, Y-, and Z-phases of the ternary $BaO \cdot MeO \cdot Fe_2O_3$ system. The hexagonal crystal structure of the phases may be described as the close-packing of spheres of the large oxygen and barium ions. Layers of these ions are perpendicular to the hexagonal axis. In the unit cell, each layer contains four large ions. The layers are most often four oxygen ions but, occurring at regular intervals, can be three oxygen ions and one barium ion. These layers are indicated by the horizontal lines. In the M-phase, the barium-containing layers occur once in five layers, and, in the W-phase, once in seven layers. In Y-phase, two adjacent barium-containing layers occur followed by four oxygen-containing layers. Hence, the cross-sections shown here containing five, seven, and six layers are termed M_5 , W_7 , and Y_6 , respectively. The large ions shown are oxygen ions (\bigcirc) and barium ions ($\textcircled{\text{hatched}}$). The small metal ions are found in the interstices of the oxygen lattice. The small black circles represent metal ions (Me) at the tetrahedral sites, and the small white circles represent metal ions at the octahedral sites. In the M- and W-phases, an additional metal ion occurs in the barium-containing layer, at a site surrounded by five oxygen ions. The small hatched circles represent metal ions surrounded by five oxygen ions. The crosses represent centers of symmetry, and the vertical lines are the threefold axes of symmetry. The unit cells of M-, W-, and Y-phases can be built by stacking together two M_5 , two W_7 , and three Y_6 cross sections, respectively. In doing so, the cross sections must be turned such that the crosses shown become centers of symmetry. The unit cell of Z-phase is built by first placing Y_6 in the orientation as it is shown here upon M_5 , which is a new cross section termed Z_{11} . Then, two Z_{11} cross sections are stacked together. It is observed that W_7 can be considered as a stacking of M_5 with two layers of an oxygen-containing layer with S composition. Finally, to realize the complete spatial structure of the unit cells for the M-, W-, Y-, and Z-phases, the described cross-sections are rotated about the central axis of symmetry 120° forward and 120° backward out of the plane [66].

Table 3.5: Chemical Formulae and Some Crystallographical Properties, including Lattice Structure Described in Figure 3.3, for the M-, W-, Y-, and Z-Phases [66]

Group	Formula	Unit cell		
		a -axis in Å	c -axis in Å	Structure
M	BaFe ₁₂ O ₁₉	5.9	23.3	2 M ₆
W	BaMe ₂ Fe ₁₆ O ₂₇	5.9	32.8	2 W ₇ = 2(M ₆ +2S)
Y	Ba ₂ Me ₂ Fe ₁₂ O ₂₂	5.9	43.5	3 Y ₆
Z	Ba ₃ Me ₂ Fe ₂₄ O ₄₁	5.9	56.0	2 (M ₆ + Y ₆)

Given the stoichiometry by the chemical formula Ba₃Co₂Fe₂₄O₄₁ for the Z-phase, the expected composition of the BaCo ferrite used in this work by element was calculated and given in Table 3.6.

Table 3.6: Composition of BaCo Ferrite Used in this Work by Element

Element	Nominal Atomic%
O	58.6
Ba	4.3
Fe	34.3
Co	2.9
Total	100.1

As previously noted, there were three batches of BaCo ferrite particles obtained from the supplier. Batches identified as BaCo Ferrite 01 and BaCo Ferrite 04 were obtained from the supplier with specified nominal particle size distribution of 45-150 μm . The size distribution was achieved by the supplier processing the material through #325 mesh and #100 mesh to retain particles greater than 45 μm and reject particles greater than 150 μm , respectively. The batch previously identified as BaCo Ferrite 02 was achieved from a batch originally obtained from the supplier and introduced now as BaCo Ferrite 02L, with “L” added to differentiate the larger particle size distribution of 45-250 μm . The size distribution was achieved by the supplier processing the material through #325 mesh and #60 mesh to retain particles greater than 45 μm and reject particles greater than 250 μm , respectively. After receipt of the BaCo Ferrite 02L batch, the BaCo Ferrite 02 batch was achieved by processing the material through #100 mesh to reject particles greater than 150 μm , giving the equivalent nominal particle size distributions to that of batches BaCo Ferrite 01 and BaCo Ferrite 04. The unique batches described here are differentiated throughout this work and are summarized in Table 3.7.

Table 3.7: Nominal Particle Size Distributions for Batches of BaCo Ferrite Particles

Identification	Applied Sieves	Nominal Particle Size Distribution
BaCo Ferrite 01	-100 +325	45 – 150 μm
BaCo Ferrite 02	-100 +325	45 – 150 μm
BaCo Ferrite 02L	-60 +325	45 – 250 μm
BaCo Ferrite 04	-100 +325	45 – 150 μm

Analytical Equipment and Methods

Scanning Electron Microscopy

Scanning electron microscopy (SEM) was utilized mainly to assess morphology and topography of the ferrite particles. It was also applied to confirm agreement with the specified nominal particle size distribution for the BaCo ferrite. The equipment used was an FEI model number XL30 environmental scanning electron microscope (ESEM) equipped with an EDAX energy dispersive spectroscope (EDS). SEM images were captured in secondary electron (SE), gaseous secondary electron (GSE), and backscattered electron (BSE) modes. For the purpose as stated for this work, SE and GSE modes were considered equivalent, and the SE and GSE modes were used interchangeable based on convenience of the current setting when the analysis was performed. In SE and BSE modes, the following parameters were applied: accelerating voltage of 20.0 kV, spot size of 4.0, and working distance of 10.0. In GSE mode, the same parameters were applied as for SE and BSE modes with exception of spot size of 5.0. SE/GSE images were captured at 500X, 1500X, and 5000X magnifications for each of the four batches, NiZn Ferrite 01, BaCo Ferrite 01, BaCo Ferrite 02, and BaCo Ferrite 04. BSE images were captured at 1500X magnification for the same batches and corresponded to the same views as those captured in SE/GSE mode at 1500X.

Energy Dispersive Spectroscopy

Energy dispersive spectroscopy (EDS) was applied to determine elemental composition. The equipment used was an FEI model number XL30 environmental scanning electron microscope (ESEM) equipped with an EDAX energy dispersive spectroscope (EDS). The EDS profiles were obtained at 1500X magnification. The elemental composition was

determined in terms of atomic% for each of the four batches, NiZn Ferrite 01, BaCo Ferrite 01, BaCo Ferrite 02, and BaCo Ferrite 04.

X-ray Diffraction

X-ray diffraction (XRD) used to determine the microstructure. Specifically, it was used to determine lattice structure of both the NiZn ferrite and BaCo ferrite and assess purity of Z-phase for the BaCo ferrite. For the NiZn ferrite, XRD was performed with a Philips X-ray diffractometer (XRD) model number PW 1800. For the BaCo ferrite, XRD was performed with a Philips XRD with a PW1830 Generator and a PW3710 multi-purpose diffractometer (MPD) control. $\text{CuK}\alpha$ source (wavelength = 0.1540562 nm) was applied as the radiation source for the XRD analyses. The four batches NiZn Ferrite 01, BaCo Ferrite 01, BaCo Ferrite 02, and BaCo Ferrite 04 were analyzed with XRD. For these batches, samples were prepared as powder with no attempt made to preferentially align the sample to obtain enhanced (00l) reflections.

Impedance Analysis

Impedance analysis was performed to determine complex permittivity (ϵ^*) of the pressed ferrite powders. The powders were pressed between two flat aluminum plates using a Carver hand-crank press. The approximate thicknesses for each sample were measured. Then, the pressed powders were measured using an HP4291A impedance analyzer to obtain ϵ^* (real and imaginary parts) with material fixture 16453A over the frequency range of 1 MHz to 1.8 GHz. From the ϵ^* measurements, ϵ' and $\tan\delta_\epsilon$ were obtained. Impedance analysis was applied to the pressed powders from all five batches, NiZn Ferrite 01, BaCo Ferrite 01, BaCo Ferrite 02, BaCo Ferrite 02L, and BaCo Ferrite 04.

Results

Morphology and Topography

Typical SEM images at 500X magnification of the magnetic particles, batches NiZn Ferrite 01, BaCo Ferrite 01, BaCo Ferrite 02, and BaCo Ferrite 04, in SE mode are shown in Figure 3.4. With respect to the 100 μm scale bar, the particles of the NiZn Ferrite 01 batch appear to range from about 10 μm for most particles to as large as about 100 μm for only a few particles. For this SEM image, one of these few large NiZn ferrite particles is seen in the center. The other three SEM images for the BaCo ferrite show comparable particle sizes for the three batches and reasonable agreement with the nominal particle size distribution of 45-150 μm .

Typical SEM images at 1500X magnification of the magnetic particles for the NiZn ferrite and BaCo ferrite batches in SE mode are shown in Figure 3.5. These same images in BSE mode are shown in Figure 3.6. The images for the NiZn Ferrite 01 batch show some whole particles and appearance of some much smaller particles on the larger particles' surfaces, lending to the appearance of a collection of non-smooth particles making up the batch. Compared to the NiZn ferrite batch, the images for the BaCo ferrite batches show relatively smoother particles overall. Comparing the different BaCo ferrite batches to each other, BaCo Ferrite 01 and BaCo Ferrite 04 batches appear to be comprised of relatively smoother particles than the BaCo Ferrite 02. This difference can be seen slightly in the SEM image in SE mode but is seen better in the SEM image in BSE mode.

Typical SEM images at 5000X magnification of the magnetic particles for the NiZn ferrite and BaCo ferrite batches in SE mode are shown in Figure 3.7. At this magnification, the relative smoothness of the particles making up the batches can be best compared. The

image of the NiZn ferrite shows the smaller size material on the surface of the particle.

Additionally, the similarity of surface smoothness between BaCo Ferrite 01 and BaCo Ferrite 04 and their difference compared to BaCo Ferrite 02 can be seen. Further, there appears to be some resemblance in surface smoothness when the particle of the BaCo Ferrite 02 batch is compared to the particle of the NiZn Ferrite 01 batch at this magnification.

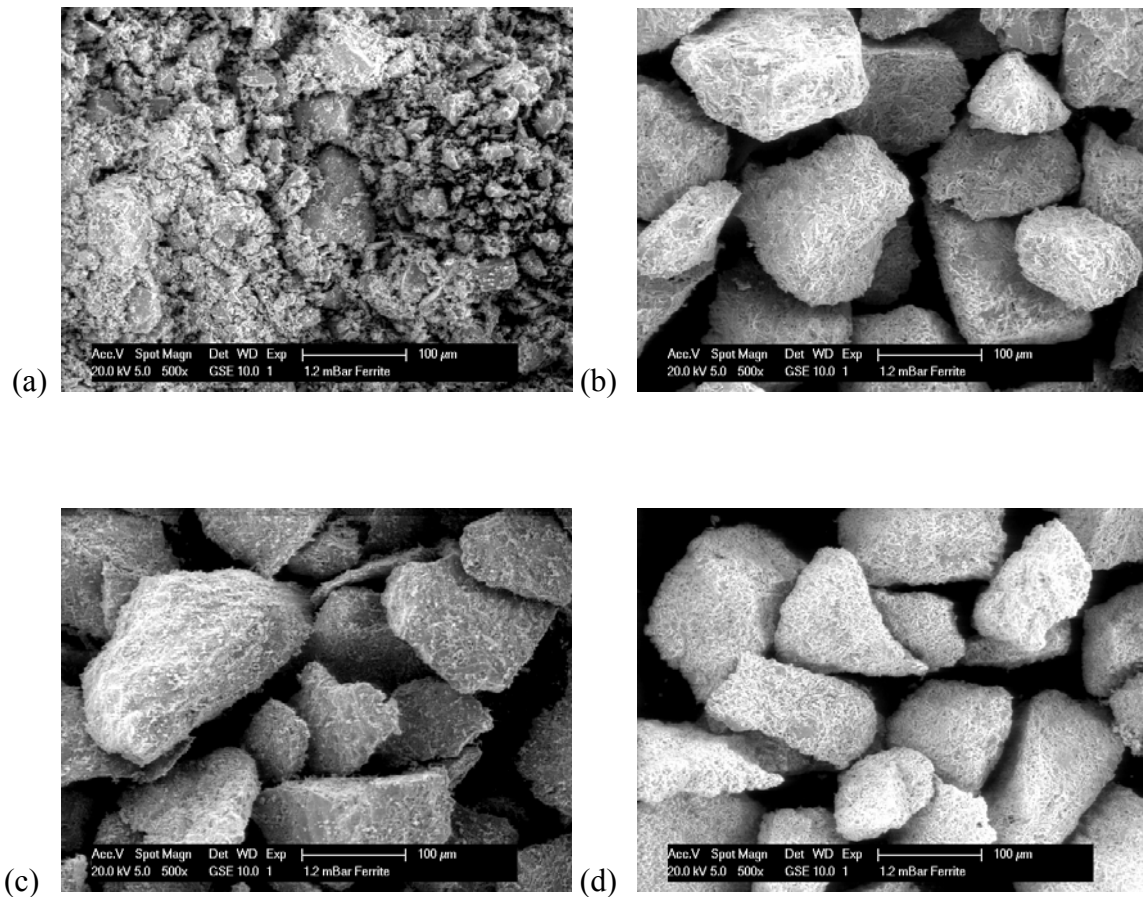


Figure 3.4: SEM images at 500X magnification of magnetic particles in SE mode. (a) NiZn Ferrite 01, (b) BaCo Ferrite 01, (c) BaCo Ferrite 02, and (d) BaCo Ferrite 04

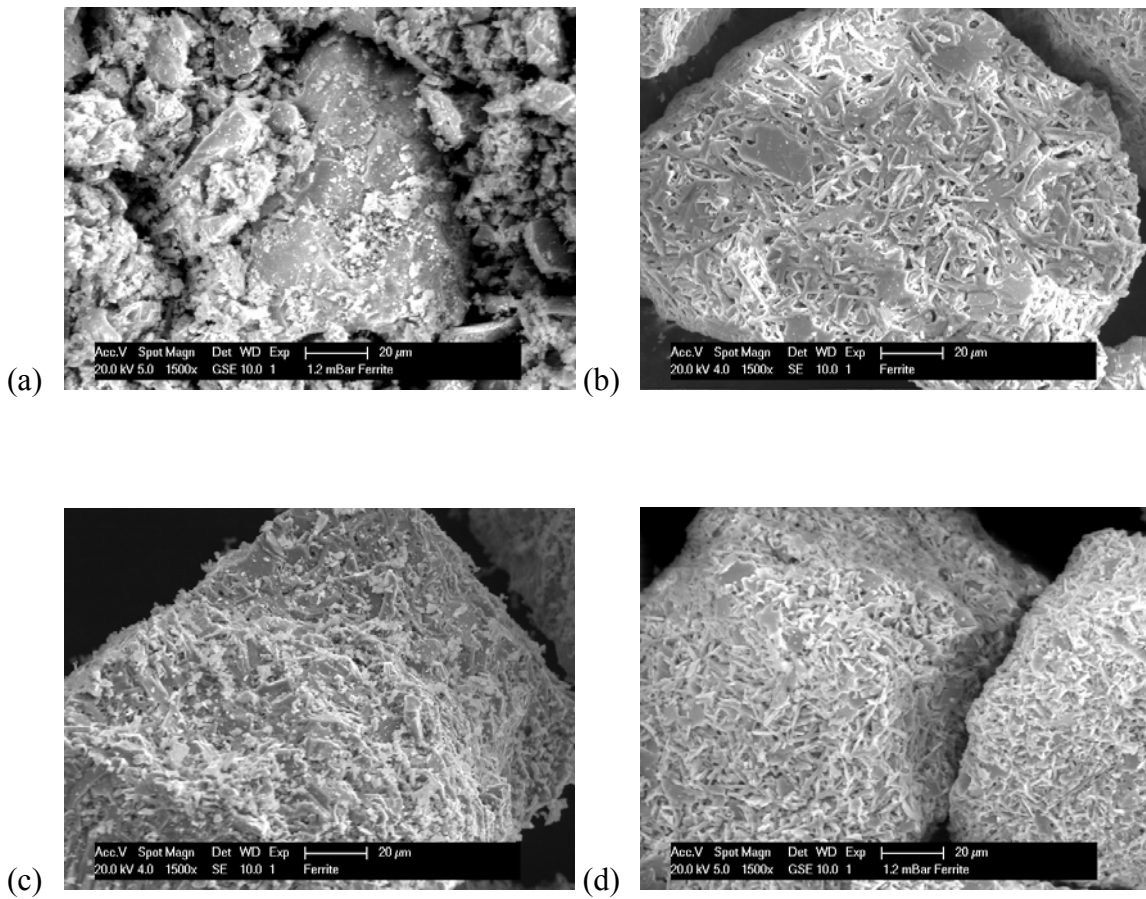


Figure 3.5: SEM images at 1500X magnification of magnetic particles in SE mode. (a) NiZn Ferrite 01, (b) BaCo Ferrite 01, (c) BaCo Ferrite 02, and (d) BaCo Ferrite 04

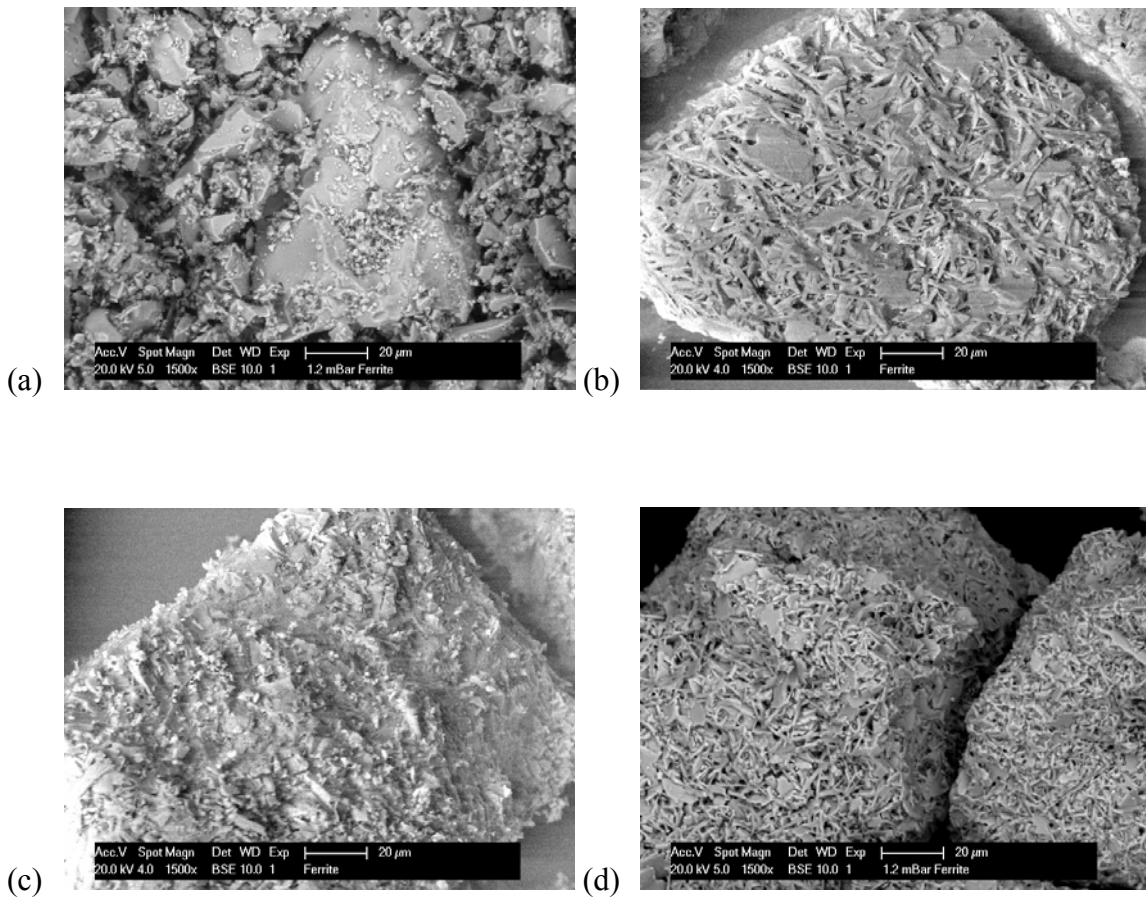


Figure 3.6: SEM images at 1500X magnification of magnetic particles in BSE mode.
 (a) NiZn Ferrite 01, (b) BaCo Ferrite 01, (c) BaCo Ferrite 02, and
 (d) BaCo Ferrite 04

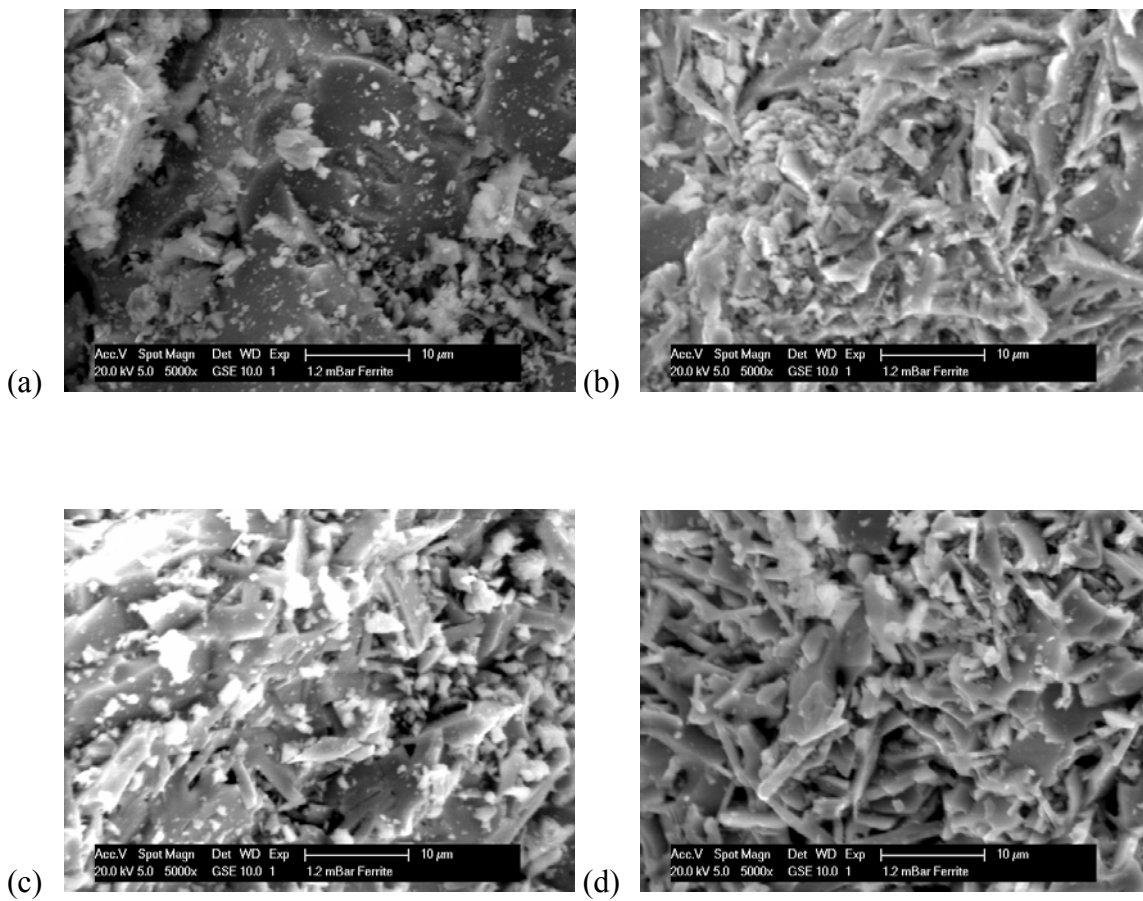
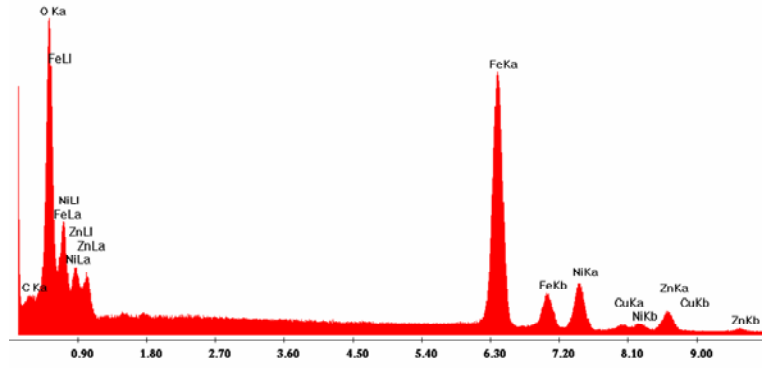


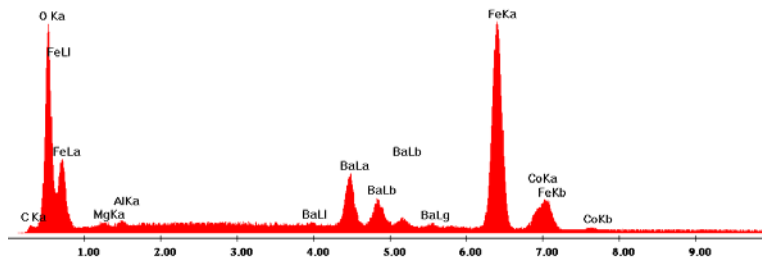
Figure 3.7: SEM images at 5000X magnification of magnetic particles in SE mode.
(a) NiZn Ferrite 01, (b) BaCo Ferrite 01, (c) BaCo Ferrite 02, and (d) BaCo Ferrite 04

Elemental Composition

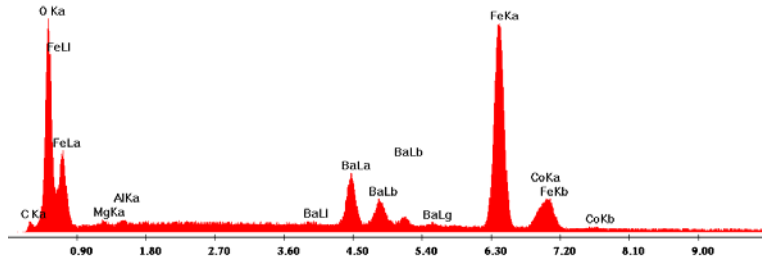
The EDS profiles taken for the magnetic particles, batches NiZn Ferrite 01, BaCo Ferrite 01, BaCo Ferrite 02, and BaCo Ferrite 04, are shown in Figure 3.8. Based on these profiles, the elemental composition was determined in terms of atomic% for each of the four batches. The atomic% results for the elements that were detected and the deviation from nominal are summarized in Table 3.8. The nominal atomic% values for the NiZn ferrite and BaCo ferrite are shown in Table 3.4 and Table 3.6, respectively. The deviations from nominal are negative for O for all samples analyzed, ranging from -17.1 to -9.5%. Deviations from nominal for Fe ranged from -12.9 to 3.9%. For the elements other than Fe or O, which differentiate the iron oxides, the greatest negative deviation was seen for Cu of the NiZn Ferrite 01 batch at -25.5% and the greatest positive deviation was seen for Co of the BaCo Ferrite 01 batch at 14.5%.



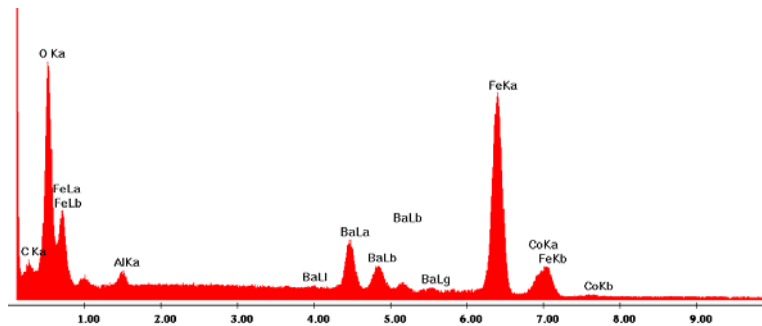
(a)



(b)



(c)



(d)

Figure 3.8: EDS of magnetic particles. (a) NiZn Ferrite 01, (b) BaCo Ferrite 01, (c) BaCo Ferrite 02, and (d) BaCo Ferrite 04

Table 3.8: Atomic% Detected by EDS for NiZn Ferrite and Deviation from Nominal
(Nominal shown in Table 3.4)

Element	Atomic% NiZn Ferrite 01	Deviation
C K	6.32	N/A
O K	51.59	-9.5%
Fe K	29.29	3.9%
Ni K	7.52	-17.4%
Cu K	0.82	-25.5%
Zn K	4.46	-3.0%
Total	100.00	N/A

Table 3.9: Atomic% Detected by EDS for BaCo Ferrite and Deviation from Nominal
(Nominal shown in Table 3.6)

Element	Atomic% BaCo Ferrite 01	Deviation	Atomic% BaCo Ferrite 02	Deviation	Atomic% BaCo Ferrite 04	Deviation
C K	4.45	N/A	7.45	N/A	12.54	N/A
O K	51.95	-11.3%	51.28	-12.5%	48.56	-17.1%
Mg K	1.00	N/A	0.88	N/A	none	N/A
Al K	0.74	N/A	0.50	N/A	1.87	N/A
Ba L	4.54	5.6%	4.19	-2.6%	4.02	-6.5%
Fe K	33.94	-1.0%	32.50	-5.2%	29.87	-12.9%
Co K	3.39	14.5%	3.19	10.0%	3.15	8.6%
Total	100.00	N/A	100.00	N/A	100.00	N/A

Microstructure

The XRD pattern obtained for NiZn Ferrite 01 batch is shown in Figure 3.9. The pattern was compared to the PCPDFWIN library and the closest match was found to be the NiZn ferrite with card number 08-0234. This compound is noted as having spinel structure. The PCPDFWIN Card 08-2034 (NiZn)Fe₂O₄ showing 2 θ peak positions is given in Figure 3.10.

The XRD patterns obtained for the BaCo Ferrite 01, BaCo Ferrite 02, and BaCo Ferrite 04 batches are shown in Figures 3.11, 3.12, and 3.13, respectively. The BaCo Ferrite 01 batch was compared to the possible compounds in the sample, which included Ba₃Co₂Fe₂₄O₄₁ (Z-phase), Ba₂Co₂Fe₁₂O₂₂ (Y-phase), BaFe₁₂O₁₉ (M-phase), and BaFe_{11.9}O₁₉. Similarly, the BaCo Ferrite 02 batch was also compared to the possible compounds in the sample, which included Ba₃Co₂Fe₂₄O₄₁ (Z-phase), Ba₂Co₂Fe₁₂O₂₂ (Y-phase), BaFe₁₂O₁₉ (M-phase), CoFe₂O₄, Fe₂O₃, and Fe_{2.936}O₄. Likewise, the BaCo Ferrite 04 batch was compared to the compounds Ba₃Co₂Fe₂₄O₄₁ (Z-phase), BaFe₁₂O₁₉ (M-phase), BaCo_{1.883}Fe_{16.12}O₂₇, Fe₂O₃, and Fe₃O₄. The PCPDFWIN Card 19-0097 Ba₃Co₂Fe₂₄O₄₁ showing 2 θ peak positions is given in Figure 3.14.

By comparison of the XRD patterns for the BaCo Ferrite 01, BaCo Ferrite 02, and BaCo Ferrite 04 batches, the BaCo Ferrite 02 batch appears to be relatively less pure than the BaCo Ferrite 01 and BaCo Ferrite 04 batches. The BaCo Ferrite 02 batch contains the targeted Z-phase as well as some M- and Y-phases. In Figure 3.12 for the BaCo Ferrite 02 batch, the peaks characteristic of the M- and Y-phases are marked by * and +, respectively. Difference is seen by the relatively higher peaks that occur at 2 θ around 24° and at less than 20° for the BaCo Ferrite 02 batch. Additionally, the peaks are relatively broader in the BaCo Ferrite 02 batch.

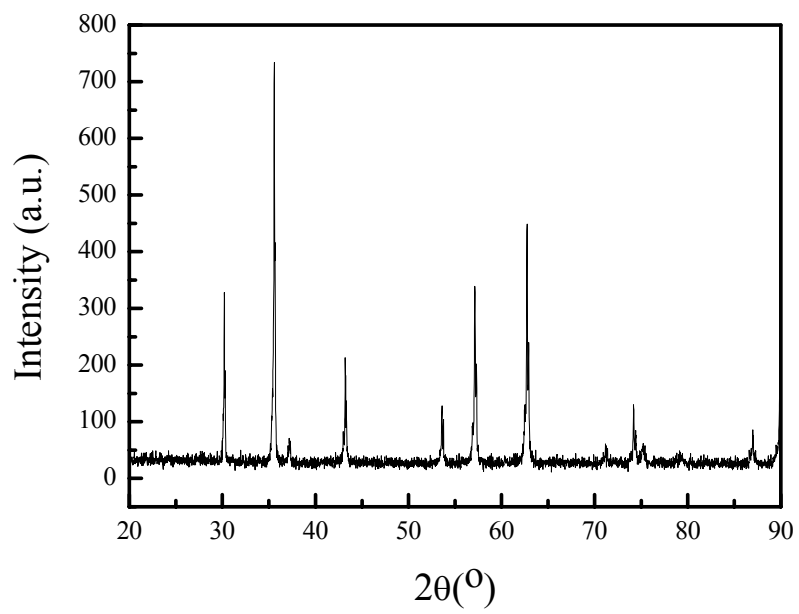


Figure 3.9: XRD pattern for NiZn Ferrite 01

08-0234		Wavelength= 1.54184				
(Ni,Zn)Fe ₂ O ₄		2θ	Int	h	k	l
Nickel Zinc Iron Oxide		18.292	14	1	1	1
		30.131	45	2	2	0
		33.193	4			
		35.438	100	3	1	1
Rad.: FeKα λ: 1.9373 Filter: d-sp: 170.0		37.104	6	2	2	2
Cut off: Int.: 1/lor.:		43.074	25	4	0	0
Ref: Kedesky, Katz, Ceramic Age, 62, 29 (1953)		53.425	10	4	2	2
		56.948	25	5	1	1
		62.549	35	4	4	0
		65.920	2b	5	3	1
		71.035	2	6	2	0
Sys.: Cubic S.G.: Fd3m (227)		74.067	8	5	3	3
a: 8.399	b:	c:	A:	C:		
			Z: 8	mp:		
α:	β:	γ:				
Ref: Ibid.		86.801	4	6	4	2
		89.712	12	7	3	1
		94.599	6	8	0	0
Dx: 5.300 Dm: SS/FOM: F ₁₆ = 11(0.080 . 19)						
Color: Brownish black						
Sample formed by solid state reaction at 1250 C of pellets of 0.5 NiO and 0.5 ZnO + Fe ₂ O ₃ . Spinel, Al ₂ Mg O ₄ type. PSC: cF56.						
Volume[CD]: 592.49.						

 © 1997 JCPDS-International Centre for Diffraction Data. All rights reserved
 .PCPDFWIN v. 1.30

Figure 3.10: PCPDFWIN Card 08-2034 (NiZn)Fe₂O₄ showing 2θ peak positions

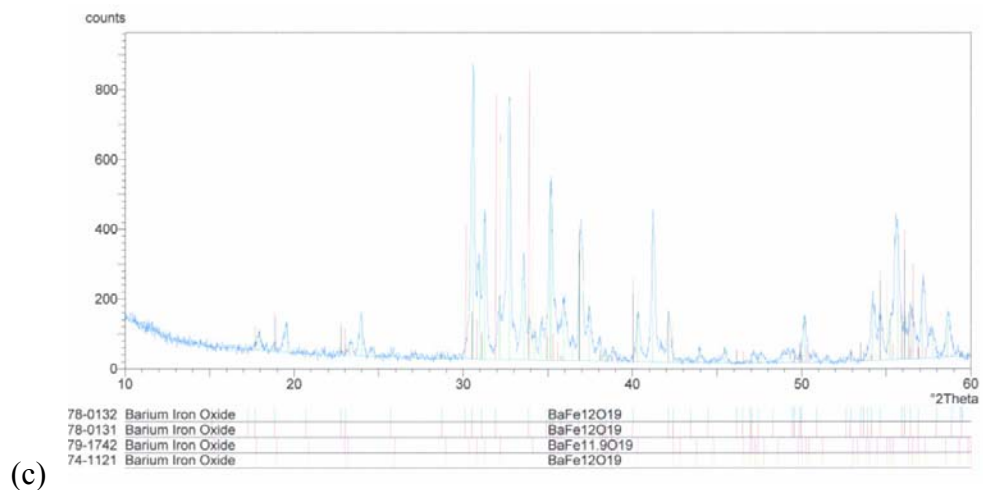
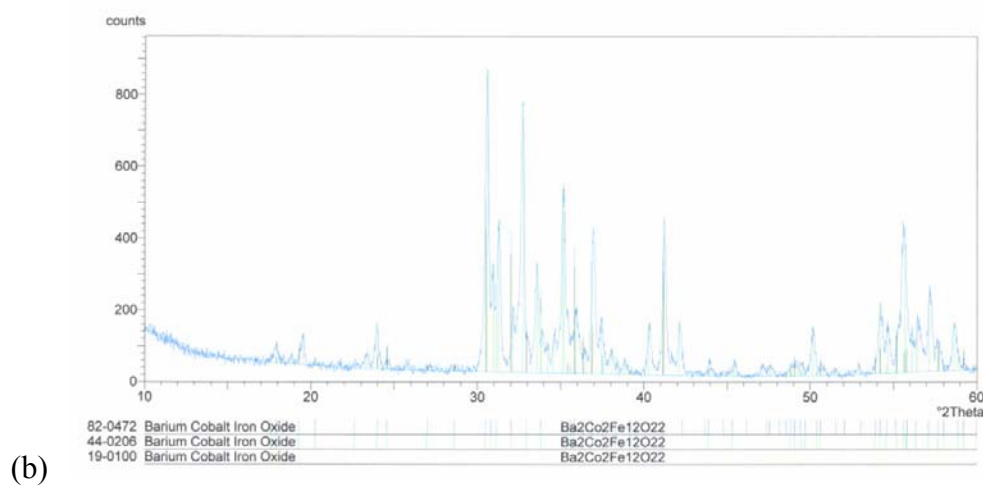
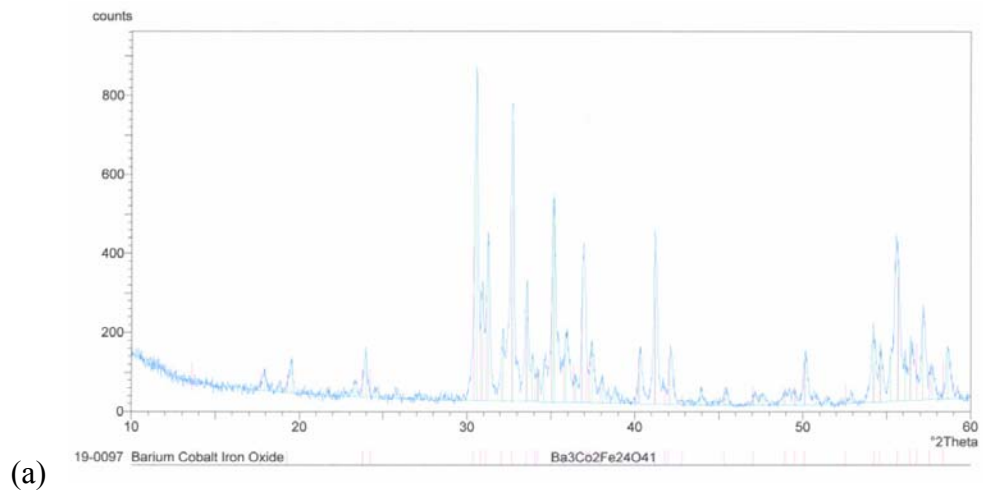


Figure 3.11: XRD pattern for BaCo Ferrite 01. Analysis comparisons to (a) Ba₃Co₂Fe₂₄O₄₁, (b) Ba₂Co₂Fe₁₂O₂₂, and (c) BaFe₁₂O₁₉ and BaFe_{11.9}O₁₉.

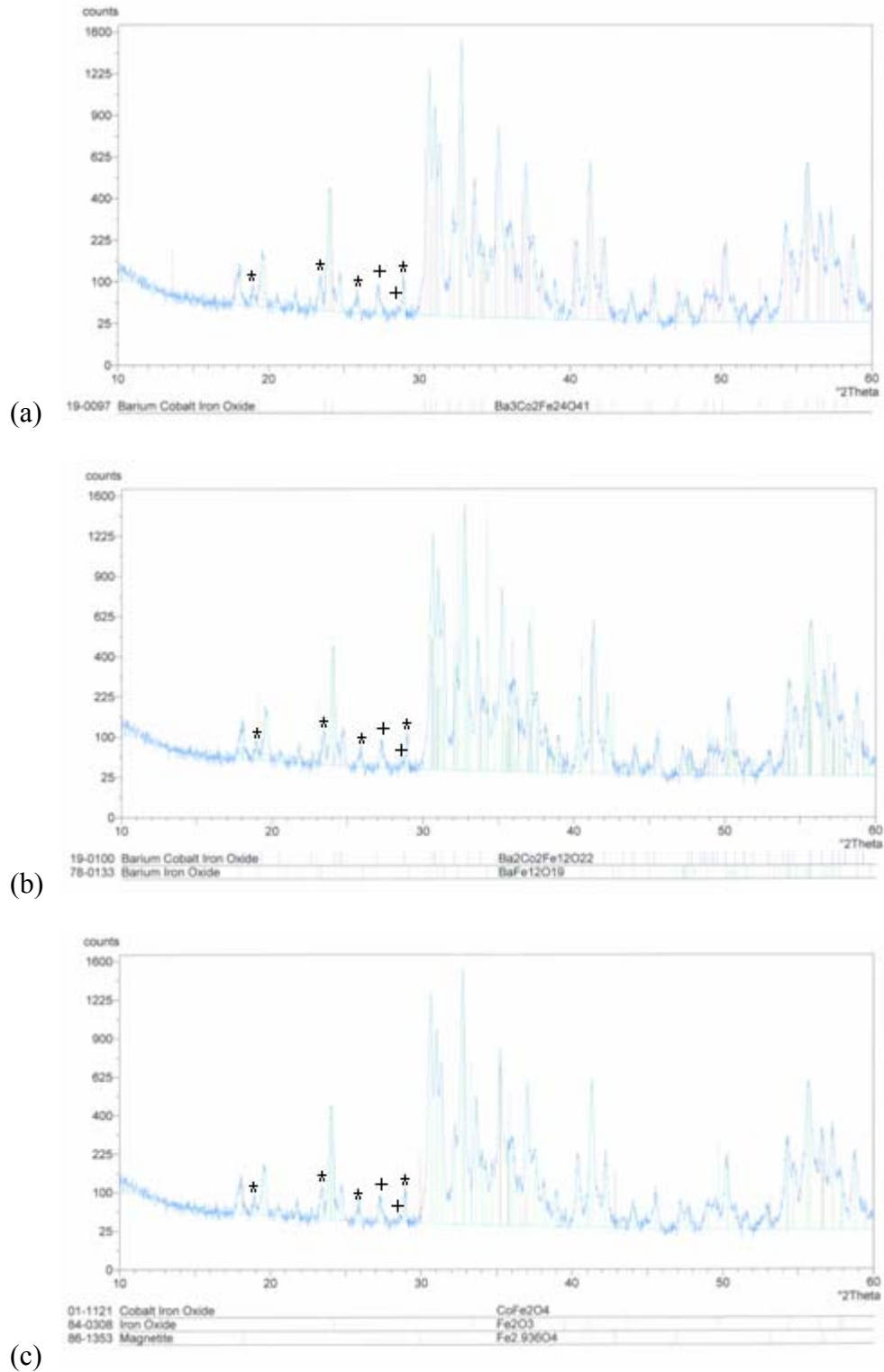


Figure 3.12: XRD pattern for BaCo Ferrite 02. Analysis comparisons to (a) Ba₃Co₂Fe₂₄O₄₁, (b) Ba₂Co₂Fe₁₂O₂₂, and BaFe₁₂O₁₉, and (c) CoFe₂O₄, Fe₂O₃, and Fe_{2.936}O₄. The peaks characteristic of the M- and Y-phases are marked by * and +, respectively.

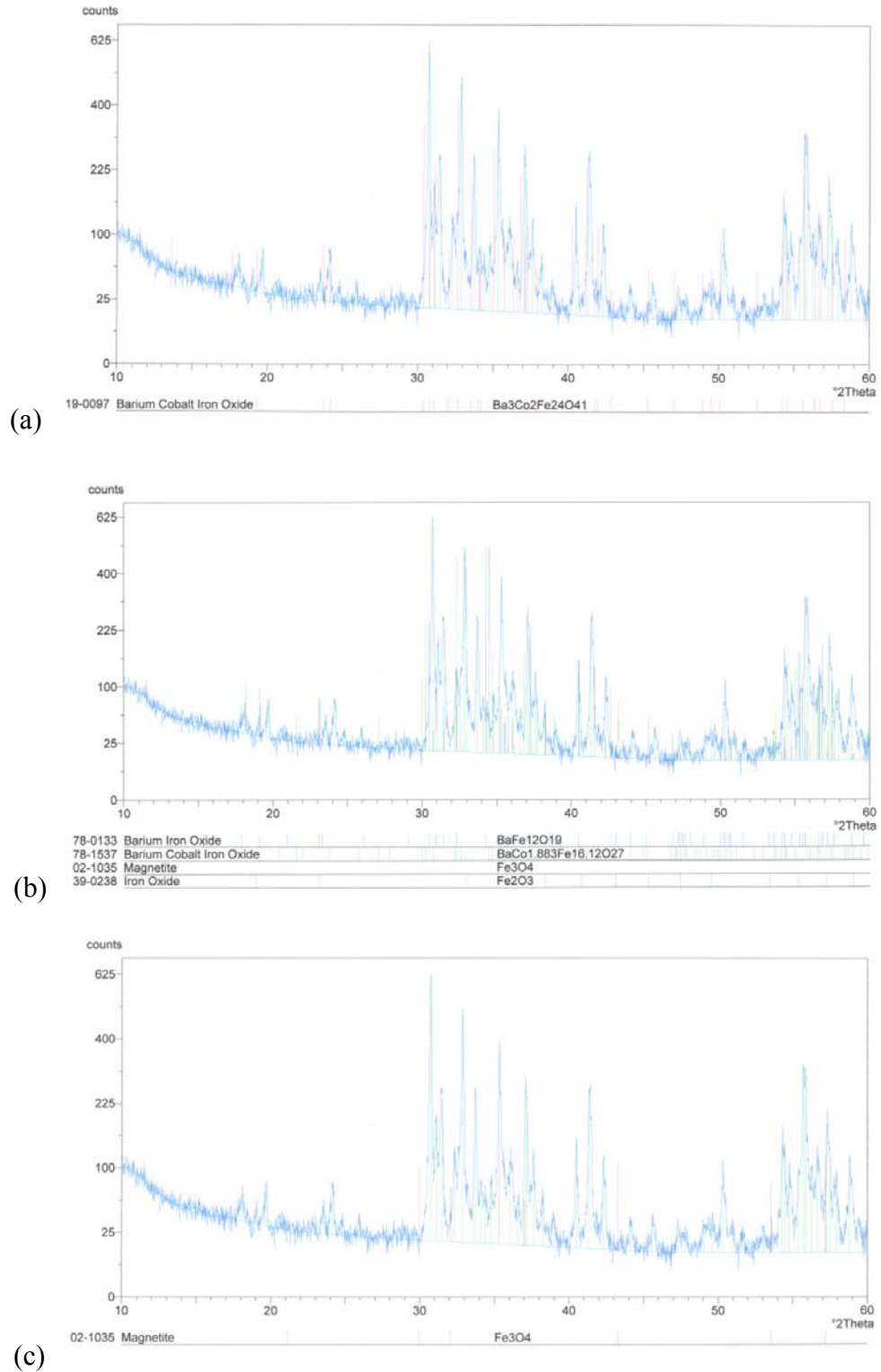


Figure 3.13: XRD pattern for BaCo Ferrite 04. Analysis comparisons to (a) Ba₃Co₂Fe₂₄O₄₁, (b) BaFe₁₂O₁₉, BaCo_{1.883}Fe_{16.12}O₂₇, Fe₃O₄, and Fe₂O₃, and (b) Fe₃O₄.

19-0097		Wavelength= 1.54184									
Ba3Co2Fe24O41		2θ	Int	h	k	l	2θ	Int	h	k	l
Barium Cobalt Iron Oxide											
		13.602	15	0	0	8	41.821	5	1	0	22
		17.703	10	1	0	2	42.025	25	2	0	13
		19.296	10	1	0	5	42.860	5	2	0	14
		23.791	15	0	0	14	45.345	10	1	0	24
		24.252	15	1	0	10	47.086	10	2	1	0
Rad.: FeKα λ: 1.9373 Filter: Mn Beta d-sp:		30.403	80	1	1	0	48.972	10	2	1	7
Cut off: Int.: Diffract. 1/1cor.:		30.833	40	0	0	18	49.540	10	2	1	8
Ref: Vinnik, Russ. J. Inorg. Chem. (Engl. Transl.), 10, 1164 (1965)		31.164	55	1	1	4	50.122	20	2	0	20
		32.081	15	1	1	6	52.598	10	2	0	22
		32.683	100	1	0	16	54.280	20	3	0	3
Sys.: Hexagonal S.G.: P6 ₃ /mmc (194)		33.564	45	1	1	8	54.630	20	3	0	4
a: 5.88 b: c: 52.31 A: C: 8.8963		34.090	10	1	0	17	55.709	65	1	0	30
α: β: γ: Z: [2] mp:		34.224	15	0	0	20	56.453	25	3	0	9
Ref: Ibid.		35.052	65	1	1	10	56.833	30	2	0	25
		35.774	20	2	0	3	57.609	15	3	0	11
		36.373	20	2	0	5	58.408	20	2	0	26
		36.836	50	1	1	12	61.854	10	1	1	30
		37.152	20	1	0	19	63.261	55	2	2	0
Dx: 5.356 Dm: SS/FOM: F ₃₀ = 4(0.099 , 84)		37.312	25	2	0	7					
		37.965	10	2	0	8					
		40.261	25	1	0	21					
		41.222	55	1	1	16					
PSC: hP140. Mwt: 2526.16. Volume[CD]: 1566.28.											


 © 1997 JCPDS-International Centre for Diffraction Data. All rights reserved
 PCPDFWIN v. 1.30

Figure 3.14: PCPDFWIN Card 19-0097 Ba₃Co₂Fe₂₄O₄₁ showing 2θ peak positions

Permittivity

Measurements of ϵ^* as a function of frequency were obtained for the five batches NiZn Ferrite 01, BaCo Ferrite 01, BaCo Ferrite 02, BaCo Ferrite 02L, and BaCo Ferrite 04. For the different samples measured, the approximate thicknesses are given in Table 3.10. Because the samples contain only pure pressed powder and no binder, the samples are extremely fragile and only approximate thicknesses can be obtained. From the measurements of ϵ^* , the results for ϵ' (equivalent to ϵ_r), ϵ'' , and $\tan\delta_\epsilon$ were extracted and plotted as shown in Figures 3.15, 3.16, and 3.17, respectively.

The value of the ϵ^* measurements depend on the thickness that is input into the impedance analyzer, although the general behavior of the ϵ^* measurement is unaffected by the inputted thickness. Therefore, when comparing the different batches, only the general behavior of the ϵ^* measurements should be compared and not the absolute values. It is expected that the absolute values of the ϵ^* measurements can be in error by several percent, however large differences in the absolute values of the ϵ^* measurements may be notable.

By inspection of the ϵ' as a function of frequency in Figure 3.15, it is immediately apparent that ϵ' for the BaCo Ferrite 02L batch has a very strong frequency dependence, starting high and dropping almost linearly from 1 MHz to 1 GHz. By closer inspection, the BaCo Ferrite 02 batch shows this same behavior. For the remaining batches, NiZn Ferrite 01, BaCo Ferrite 01, and BaCo Ferrite 04, ϵ' is independent of frequency, showing constant ϵ' values over the frequency sweep. Additionally, the relatively higher ϵ' values for the BaCo Ferrite 02L and BaCo Ferrite 02 batches are recognized as possibly significant, as the values are much greater than the other ϵ' values.

By inspection of the ϵ'' as a function of frequency in Figure 3.16, the behavior of ϵ'' for the BaCo Ferrite 02L batch is once again immediately recognized as different. Over the 1 MHz to 1.8 GHz frequency sweep, the BaCo Ferrite 02L batch shows permittivity relaxation, that is, where a maximum ϵ'' occurs, at 1.401 GHz. Additionally, the relatively higher ϵ'' values for the BaCo Ferrite 02L and BaCo Ferrite 02 batches are recognized as possibly significant, as the values are much greater than the other ϵ'' values.

Although $\tan\delta_\epsilon$ is obtained from dividing ϵ'' by ϵ' , it is shown in Figure 3.17 to be complete and also because it is a convenient property to compare loss that is normalized to permittivity property ϵ' . The relatively higher $\tan\delta_\epsilon$ values for the BaCo Ferrite 02L and BaCo Ferrite 02 batches are recognized to occur and as possibly significant, as the values are greater than the other $\tan\delta_\epsilon$ values, even with the normalization.

Table 3.10: Sample Thicknesses of Pressed Ferrite Powder Disks for Permittivity Measurements

Identification	Sample Thickness (mm)
NiZn Ferrite 01	1.680
BaCo Ferrite 01	2.360
BaCo Ferrite 02	1.310
BaCo Ferrite 02L	1.772
BaCo Ferrite 04	2.068

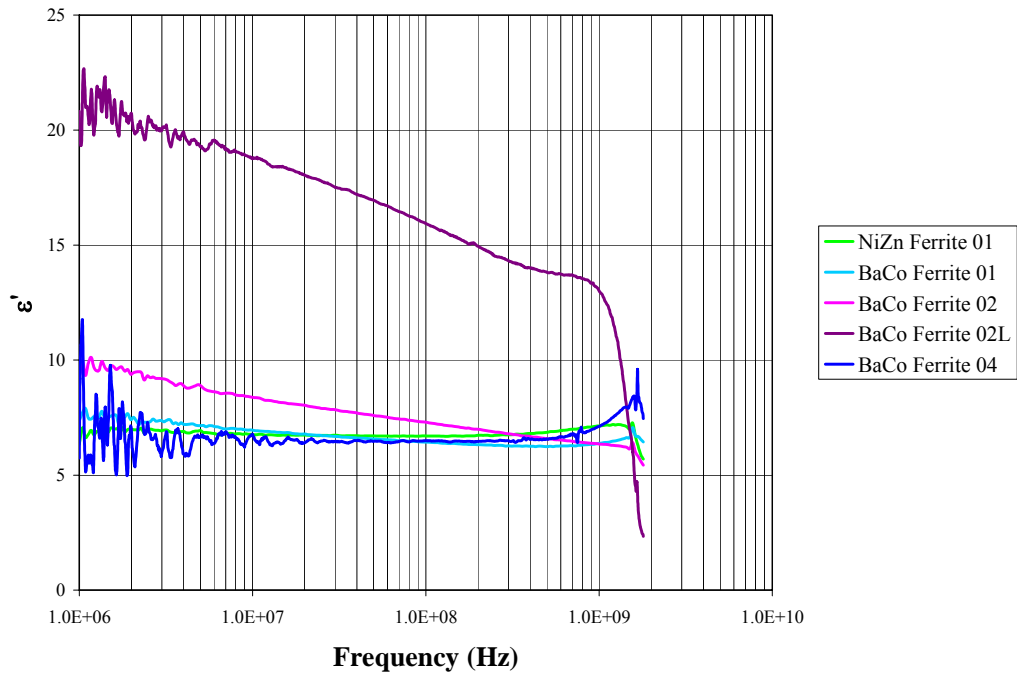


Figure 3.15: ϵ' versus frequency for ferrite powders pressed into disk shapes

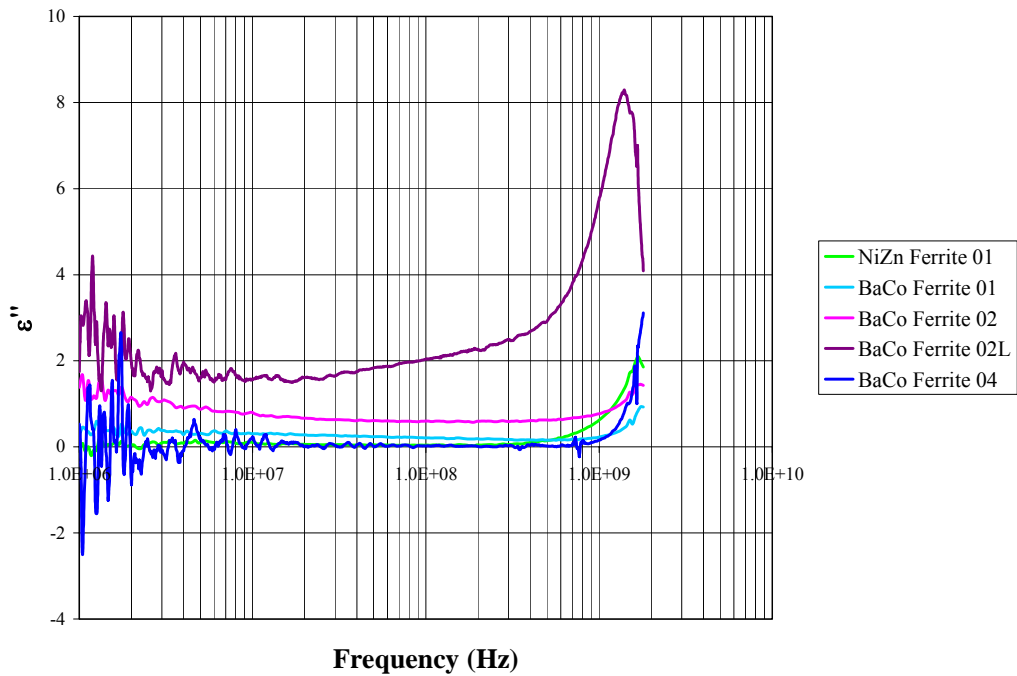


Figure 3.16: ϵ'' versus frequency for ferrite powders pressed into disk shapes

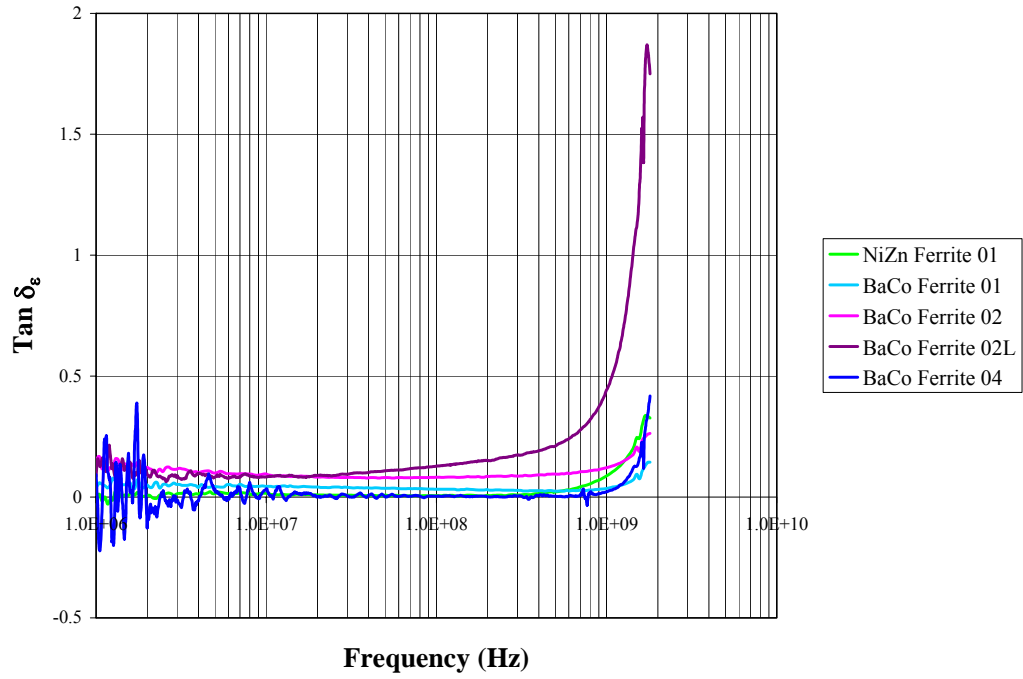


Figure 3.17: $\tan \delta_e$ versus frequency for ferrite powders pressed into disk shapes

Discussion

There were marked differences observed between expected microstructure and properties and the actual microstructure and properties when comparing the BaCo Ferrite 02 batch and all other batches. Specifically, when compared to the other BaCo ferrite batches only, the BaCo Ferrite 02 batch was observed to be less pure, that is, not pure Z-phase, based on inspection of the XRD patterns. Due to the complexity of the microstructure, other phases, such as the Y- and M-phases from which the Z-phase is converted, appeared to possibly be present. Other phases, such as magnetite Fe_3O_4 with spinel lattice structure, which is a compound included earlier in the conversion process, were also investigated, but their presence could not be confirmed in the XRD pattern. For the permittivity property, the expected general behavior was constant ϵ' with frequency, from the beginning of the frequency sweep to at least the lower UHF spectrum ($\sim 300\text{-}500$ MHz). In Figure 3.15, the BaCo Ferrite 02 batch showed a relatively higher ϵ' value at the beginning of the frequency sweep that then constantly decreased with increasing frequency. This behavior was more pronounced in the BaCo Ferrite 02L batch, which was obtained from the same batch as BaCo Ferrite 02 but contained a particle size distribution with larger particles. The BaCo Ferrite 02L batch showed a value of ϵ' an order of magnitude higher than the others at the beginning of the frequency sweep that then constantly decreased with increasing frequency at a rate similar, and possibly slightly faster, than that for the BaCo Ferrite 02 batch. Additionally, in Figure 3.16, the BaCo Ferrite 02L batch showed a dielectric relaxation, that is, a peak in ϵ'' within the frequency sweep.

Based on observed microstructure and properties ϵ' and ϵ'' , the mechanism for the behavior of the ϵ' and ϵ'' properties for BaCo Ferrite 02 batch is proposed to begin with

available reduced ions, such as Fe^{2+} , Co^{2+} , and Ba^{2+} , in the ferrite material. These ions are available when compounds such as CoFe_2O_4 and Fe_3O_4 are present. Because these compounds have spinel structure, detecting spinel in the XRD pattern would have confirmed presence of the Fe^{2+} ions. Referencing the ternary diagram for the $\text{BaO}\cdot\text{MeO}\cdot\text{Fe}_2\text{O}_3$ system shown in Figure 3.2, the S compound has spinel structure, confirming the coexistence of both spinel and hexagonal structures within the $\text{BaO}\cdot\text{MeO}\cdot\text{Fe}_2\text{O}_3$ system. It should be noted that CoFe_2O_4 is an S-compound, and Fe_3O_4 is one of the early compounds in the conversion process. Although spinel could not be definitely confirmed, the observed decreased purity does provide evidence that the process did not completely or correctly convert all materials to the targeted Z-phase. The incomplete or incorrect conversion supports that other compounds existing in the ternary system can be present and, therefore, that Fe^{2+} ions may be available in the batch.

The availability of these reduced ions allows transitions shown by (3.1), (3.2), (3.3), and (3.4) to occur [67].



The existence of the electrons freed by these transitions causes polarization in the surrounding lattice. Two types of polarization that occur are due to electron displacements and lattice displacements. The displacements create energy levels just below the conduction band. When the electron moves, it takes its state of polarization with it. New regions

polarize while others return to normal. The movement of these charges in a polarized medium are termed polarons [68, 69]. With freed electrons in the BaCo Ferrite 02 batch, polarons are responsible for the observed ϵ' and ϵ'' behavior. The dependency of ϵ' over a frequency sweep and higher ϵ' value for the BaCo Ferrite 02 and BaCo Ferrite 02L batches shown in Figure 3.15 has been observed and explained by the same mechanism for other compounds in the BaO·MeO·Fe₂O₃ system [67, 70]. Additionally, the shift of the dielectric relaxation to relatively lower frequencies and the higher ϵ'' value for the BaCo Ferrite 02L batch shown in Figure 3.16 has also been observed and explained by the same mechanism for another compound in the BaO·MeO·Fe₂O₃ system [67].

The behavior of ϵ' and ϵ'' for the BaCo Ferrite 02 and BaCo Ferrite 02L is not favorable for the targeted antenna application of this work. For this work, the favored properties for the antenna application in the lower UHF spectrum (~300-500 MHz) include constant ϵ' values up to and over the targeted operating frequency range, low and constant ϵ'' values up to and over the targeted operating frequency range, and the dielectric relaxation to occur at frequencies well above the targeted operating frequency range. It has been show that the favorable behavior of ϵ' and ϵ'' (and therefore $\tan\delta_e$) can be achieved and is reproducible by the BaCo Ferrite 01 and BaCo Ferrite 04 batches. To ensure that the favorable properties are achieved, the formulation process must enable complete and correct conversion to obtain the pure Z-phase. According to Philips, the conversion process must enable Fe²⁺ ions to be properly replaced by other ions [66]. Another consideration for ensuring that the conversion process proceeds correctly is application of an oxygen atmosphere during the process. The oxygen atmosphere provides protection so that the desired iron deficient composition is achieved and presence of Fe²⁺ ions is prevented [67].

Conclusions

The SEM and EDS analyses provided reasonable agreement with manufacturer specifications on particle size and elemental composition, respectively. Taken together, the XRD and impedance analyses showed BaCo Ferrite 02 batch different than the other batches. It was observed that the microstructure of BaCo Ferrite 02 batch was different than the other BaCo ferrite batches, because the BaCo Ferrite 02 batch appeared to be less pure Z-phase. Compared to the other BaCo ferrite batches, the permittivity behavior for the BaCo Ferrite 02 batch included ϵ' having strong dependence on frequency and higher ϵ' values across the frequency sweep. Additionally, the permittivity behavior for the BaCo Ferrite 02 batch also showed higher values for ϵ'' , and the BaCo Ferrite 02L batch (that had a particle size distribution that included larger particles) showed dielectric relaxation within the frequency sweep.

The observed structure difference detected by XRD was linked to the permittivity results. The mechanism for the permittivity behavior of the BaCo Ferrite 02 batch was proposed to be polarons produced from availability of reduced species, such as Fe^{2+} , Co^{2+} , and Ba^{2+} , due to the relatively lower O-content in the compound. For this work, the favored properties for the antenna application in the lower UHF spectrum (~300-500 MHz) include constant ϵ' values up to and over the targeted operating frequency range, low and constant ϵ'' values up to and over the targeted operating frequency range, and the dielectric relaxation to occur at frequencies well above the targeted operating frequency range. The NiZn Ferrite 01, BaCo Ferrite 01, and the BaCo Ferrite 04 demonstrated these favorable permittivity properties. Additionally, for the BaCo ferrite, the formulation and characterization the BaCo Ferrite 01 and BaCo Ferrite 04 batches showed that these permittivity properties are reproducible.

CHAPTER IV: FORMULATION AND CHARACTERIZATION OF MAGNETIC COMPOSITES

Introduction

For this work, formulation of magnetic composites with optimum electromagnetic properties and low loss is investigated by a combination of three approaches. The approaches include formulating magnetic composites and characterizing both complex permittivity (ϵ^*) and complex permeability (μ^*) as a function of frequency to determine (1) the optimum ferrite for the targeted operating frequency, (2) the effect of functionalizing the ferrite particles as part of the composite formulation process, and (3) the effect of ferrite particle size distribution. The optimum electromagnetic properties and low loss are explored in these approaches by investigating the both the behavior and relative values of ϵ^* and μ^* as a function of frequency.

First, to introduce minimal magnetic loss and optimize magnetic property for the composite, the ferrite particles was investigated for the targeted lower UHF spectrum (~300-500 MHz) based on ϵ^* and μ^* properties over the 1 MHz to 1 GHz frequency range. For their application to antenna design, the favored behavior of the magnetic composites is constant ϵ^* and μ^* properties with frequency, extending to the targeted operating frequency, and low loss quantified by imaginary part of permittivity (ϵ''), dielectric loss tangent ($\tan\delta_\epsilon$), imaginary part of permeability (μ''), and magnetic loss tangent ($\tan\delta_\mu$).

Second, to further reduce magnetic loss, the ferrite particle surface was functionalized to form a self assembled monolayer (SAM) coating around the particles and increase the electrical resistivity at the particle-matrix interface. The functional group provided by silane

has potential for achieving the increased interfacial resistivity. Silane has shown to be compatible with processing ferrite powders and has improved final properties of injection bonded magnets produced from the powders [71]. In two independent studies on polyethylene for power cable applications, silane have shown to increase the electrical breakdown strength at the insulating polyethylene and inorganic interface [72, 73]. In another study on electrically insulating materials for power applications, a polyester modified silicone coating on ZnO varistor ceramic was shown to be effective in reducing interfacial space charge and enable the ability to withstand higher impulse currents [74]. In a study on rare earth magnets for high frequency applications, micron-size magnetic particles coated with a polymer mixture that included epoxy resin and silane demonstrated reduced eddy current loss by measuring irreversible losses in varying magnetizing field at 500 kHz [75]. Additionally, silane was shown to have affinity for ceramic surface of a multichip module (MCM) and thereby promoted adhesion between silicone and the ceramic interface [76].

In this work, the proposed mechanism to occur in the case of ferrite in silicone with the added silane functional group is the same as that between the ceramic and silicone in the MCM adhesion study and is shown in Figure 4.1.

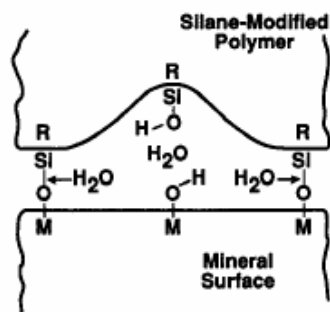


Figure 4.1: Proposed mechanism to increase resistivity at particle-matrix interface by silane functional group [76]

The resulting SAM coating to form around the ferrite particles is given in the generalized illustration shown in Figure 4.2. The silane functional group will orient to selectively tie to the ferrite and the R group will preferentially react with the matrix, which is expected to reduce availability of the more polar –OH groups thereby reducing electron mobility.

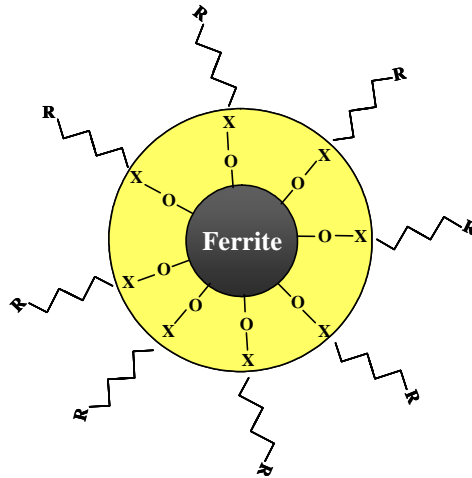


Figure 4.2: Generalized illustration of ferrite particle functionalized by SAM molecules, where X = Si from the silane function group

In addition to impedance analysis of the composites to obtain ϵ^* and μ^* over the 1 MHz to 1 GHz frequency range, effects due to the SAM coating on the mechanical properties coefficient of thermal expansion (CTE) and complex Young's modulus (E^*) of the composites were investigated. Thermomechanical analysis (TMA) was performed to obtain the CTE of the composites. Dynamic mechanical thermal analysis (DMTA) was performed to obtain E^* (real and imaginary parts), including both storage modulus (E') and loss modulus (E''), of the composites.

Third, for optimum ϵ^* and μ^* properties, the effects of ferrite particle size distribution in the composites were investigated. For this work, the approach was to use particle sizes that

are sufficiently large in order to not disrupt the magnetic domains, therefore avoiding undesirable hysteresis loss and preserving real part of permittivity (μ') values. The ϵ^* and μ^* properties for two different size particle size distributions of ferrite were compared.

This chapter includes these three approaches for investigating formulation of magnetic composites with optimum electromagnetic properties and low loss. To begin, magnetic composites were formulated from the ferrite described in the previous chapter, in Table 3.2 and in more detail in Table 3.7. The magnetic composites were comprised of 40 vol% ferrite particles in a silicone matrix. The main analytical technique was impedance analysis of the composites to obtain ϵ^* and μ^* over the 1 MHz to 1 GHz frequency range. For characterization of ϵ^* and μ^* of the composites, the variation of the measurements as well as variation of the composite formulation process were investigated. Then, the effects of silane functionalized ferrite particles in the composites on the mechanical properties CTE and E^* and the electromagnetic properties ϵ^* and μ^* were investigated. Finally, the effects of particle size distribution on ϵ^* and μ^* were also investigated.

Materials and Methods

Composite Formulation

This study includes composites made from ferrite, namely, NiZn ferrite and BaCo ferrite, in a silicone matrix. The ferrite batches used in formulation of the composites are described in Table 3.2 and in further detail in Table 3.7. The silicone used was Dow Corning Sylgard 184 silicone. For formulations in which the ferrite was treated with silane, vinyltriethoxy silane was used and supplied by GE Advanced Materials with trade name Silquest A-151 Silane. The chemical structure of vinyltriethoxy silane is shown in Figure 4.3.

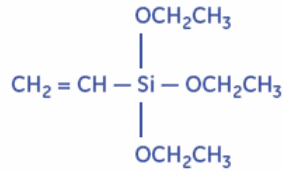


Figure 4.3: Vinyltriethoxy silane chemical structure

The formulated magnetic composites were comprised of 40 vol% ferrite in silicone. The densities of the ferrites used to calculate the amount of ferrite required in the formulation process are given in Table 3.1. The density assumed for silicone was 1 g/cm³. The composite formulation process was begun by drying the ferrite overnight under vacuum at 711 mm Hg and 70°C. Then, the ferrite was stirred into the uncured silicone with an electric mixer at 240 rpm and 110°C for 30 minutes. The equipment and setup used in the composite formulation process is described in Figure 4.4. Finally, the silicone curing agent in the proportion prescribed by supplier was stirred by hand into the resulting paste of ferrite and uncured silicone.

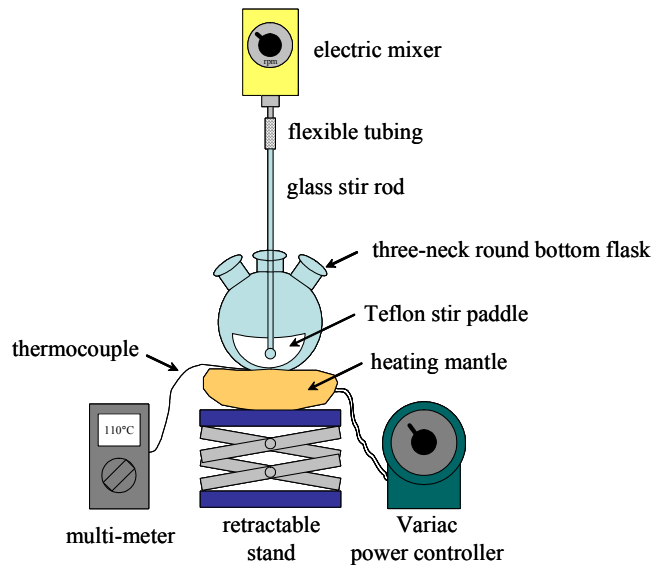


Figure 4.4: Equipment and setup used in the composite formulation process

There were three formulations in which the ferrite was treated with silane. The process for treating the ferrite with silane was begun by adding the ferrite powder to a beaker. The ferrite treated with silane was the NiZn Ferrite 01 batch described in Table 3.2. Then, an aqueous solution of 95 vol% methanol/5 vol% distilled water was added to cover the ferrite powder. The silane was then charged into the beaker in the amount equal to 0.5, 1.0, and 1.5 wt% of total ferrite to be treated for the three different formulations. The mixtures were stirred with a spatula until no air bubbles were seen. Next, the ferrite powder was dried at 125°C for 2 hours. Finally, the dry powder was transferred out of oven and immediately stored in a desiccator. The resulting ferrite powders treated with the 0.5, 1.0, and 1.5 wt% silane were then used in the composite formulation process just previously described.

Substrate Fabrication

Substrates were made from both the magnetic composites and pure silicone. The fabrication process began by transferring either the uncured composite paste or the pure uncured silicone into a flat mold. The critical dimensions of the flat mold designed for the substrate formulation process is described in Figure 4.5. The mold was made by routing a 305 x 457 x 1.6 mm FR-4 panel to obtain one 180 x 180 mm and four 77 x 77 mm cavities with surrounding reservoirs. Then, the initial flat mold was completed by adhering a piece of 1 oz copper foil to the back with silicone as the adhesive. To produce composite substrates with nominal thicknesses of 1.6-3.2 mm, approximately 34 g of uncured composite was placed in the 77 x 77 mm cavities and approximately 186 g was placed in the 180 x 180 mm cavity. The silicone substrate is fabricated using the identical steps with the exception of placing pure uncured silicone in the flat mold. Uncured silicone was placed into the cavities in an amount until the surface tension of the silicone was seen just above the cavity top.

After filling the uncured material into the mold, FR-4 pieces obtained from routing the original panel were replaced into any unused cavities. Next, uncured pure silicone was placed around the panel edges to act as glue, and a new piece of 1 oz copper foil was placed on top of the mold, thereby completing the mold stack up.

The mold stack-up was then placed into a TMP printed circuit board (PCB) oil press. Prior to curing, the mold stack up was held under vacuum at 711 mm Hg for 30 minutes. The curing process was immediately initiated and took place under vacuum at 711 mm Hg. The temperature profile for the curing process included a maximum temperature set point of 121°C for 80 minutes. The entire temperature profile included the following steps: go to 38°F and hold for 3 minutes; go to 71°F with 6 minute ramp time and hold for 10 minutes; go to 121°F with 9 minute ramp time and hold for 80 minutes; and go to 38°F with 15 minute ramp time and hold for 20 minutes. The curing temperature profile, including set point and actual temperatures for a typical curing process, is shown in Figure 4.6. The accompanying mechanical press profile includes the following steps: go to 345 kPa and hold for 10 minutes; go to 1,034 kPa and hold for 80 minutes; and go to 345 kPa and hold for 1 minute.

After the curing process, the stack up was removed from the press. The substrate was obtained by carefully pulling the copper foil away from both sides of the bare FR-4 panel and then separating the substrate edges away from the cavity sides with a razor.

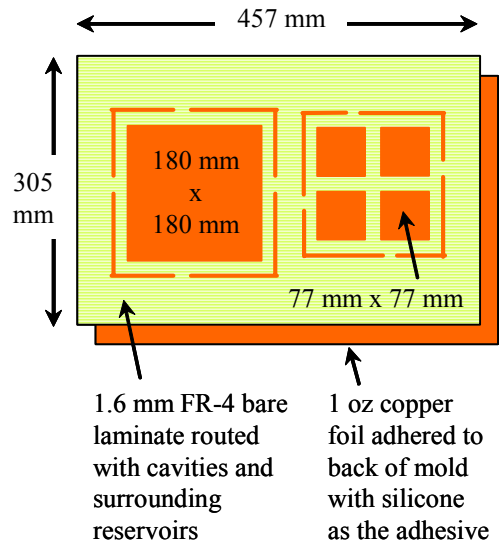


Figure 4.5: Critical dimensions of mold design on 305 x 457 x 1.6 mm FR-4 panel including one 180 x 180 mm and four 77 x 77 mm cavities with surrounding reservoirs

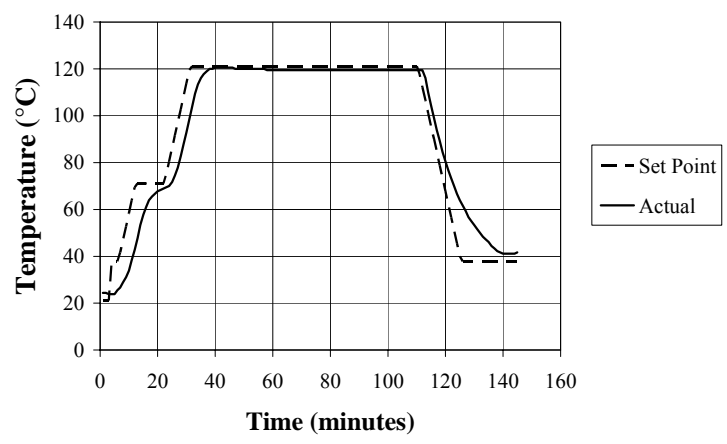


Figure 4.6: Curing temperature profile, including set point and actual temperatures for a typical curing process

Analytical Equipment and Methods

Impedance Analysis

Impedance analysis was performed to determine ϵ^* and μ^* (real and imaginary parts) of the composites and pure silicone. The materials were measured using an HP4291A impedance analyzer to obtain ϵ^* and μ^* with material fixtures 16453A for ϵ^* and 16454A for μ^* over the frequency range of 1 MHz to 1.8 GHz. The data for ϵ^* and μ^* was obtained in equal logarithmic increments over the frequency range of 1 MHz to 1.8 GHz, giving a total of 201 data points for each real part of permittivity (ϵ'), real part of permeability (μ'), dielectric loss tangent ($\tan\delta_\epsilon$), and magnetic loss tangent ($\tan\delta_\mu$) measurements. The materials were prepared by cutting samples with a die from the prepared substrates in shapes accepted by the material fixtures. For ϵ^* , the shape used was a disk with 20 mm diameter and nominal thickness of 1.6-3.2 mm. For μ^* , the shape was a disk with a concentric circular center cut as shown in Figure 4.7. For the specific fixture used to measure μ^* in this work, dimensions were outer diameter (a) of 20 mm, inner diameter (b) of 6 mm, and nominal thickness (h) of 1.6-3.2 mm. A picture of actual samples for impedance analysis is shown in Figure 4.8. Due to the variation in the nominal thickness in the substrate fabrication and sensitivity to sample thickness for the ϵ^* and μ^* measurements, all sample thicknesses were measured twice with an Exact Automatic Micrometer, an analog (dial) micrometer with 0.0005 inch increments and range of 0-0.200 inch available from E. J. Cady & Company. The average of the two thickness measurements was applied for the impedance analysis. For the impedance analysis, there were 5 measurements taken for each ϵ' , μ' , $\tan\delta_\epsilon$, and $\tan\delta_\mu$ for every sample. Unless otherwise stated, the average of the 5 measurements were taken as the final values for ϵ' , μ' , $\tan\delta_\epsilon$, and $\tan\delta_\mu$.

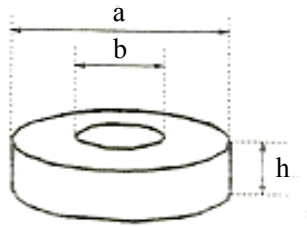


Figure 4.7: Shape of disk with a concentric circular center cut for μ^* measurements with outer diameter (a), inner diameter (b), and thickness (h)

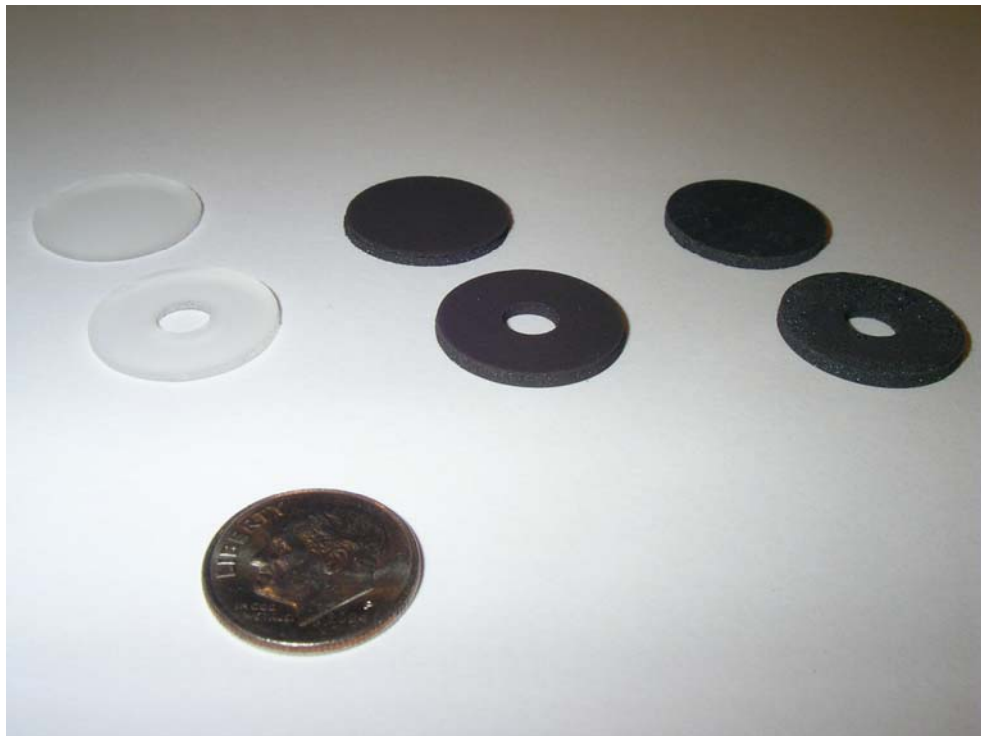


Figure 4.8: Picture of actual samples for impedance analysis. A dime is shown in the foreground for size reference. From left to right, pure silicone, NiZn ferrite composite, and BaCo ferrite composite are shown. Back row are samples for ϵ^* measurements, and front row are samples for μ^* measurements.

Thermomechanical Analysis

Thermomechanical analysis (TMA) was performed to obtain the coefficient of thermal expansion (CTE) of the composites and pure silicone. The equipment used was a TA Instruments thermomechanical analyzer (TMA) model number 2940. The materials were tested over the temperature range of 30-235°C with an initial isothermal hold at 30°C for 1 minute and a subsequent ramp rate of 10°C per minute. The sample dimensions were approximately 5 mm square with nominal thickness of 1.6 mm. All samples were measured twice to obtain two CTE values per sample.

Dynamic Mechanical Thermal Analysis

Dynamic mechanical thermal analysis (DMTA) was performed to obtain complex Young's modulus (E^*) (real and imaginary parts) of the composites and pure silicone. The equipment used was a Rheometric Scientific dynamic mechanical thermal analyzer (DMTA) model number V. From E^* , both storage modulus (E') and loss modulus (E'') were obtained. The samples were tested using a single cantilever bending geometry with a medium fixture that provided a fixed specimen length of 8 mm for the test. The other dimensions for the specimens included approximate width of 10 mm and the approximate thickness of 1.65 mm. The DMTA test type was dynamic temperature ramp, which was performed over temperature range of 30-200°C, with a ramp rate of 5°C per minute, frequency of 1 Hz, and force of 0.01 N. All samples were tested twice, the first test to remove thermal history and the second test to obtain comparable values of E' and E'' for the samples.

Results

Effect of Ferrite Type

Permittivity

The results of ϵ' , ϵ'' , and $\tan\delta_\epsilon$ as a function of frequency for composites comprised of the five ferrite types NiZn Ferrite 01, BaCo Ferrite 01, BaCo Ferrite 02, BaCo Ferrite 02L, and BaCo Ferrite 04 and pure silicone are shown in Figures 4.9, 4.10, and 4.11, respectively. By visual inspection of the permittivity behavior for the composites seen these figures, most notable is the similarity in behavior seen for the pressed ferrite powders in Figures 3.15, 3.16, and 3.17. The ϵ^* behavior of the composites mimics the ferrite powders from which they are made.

By inspection of the ϵ' as a function of frequency in Figure 4.9, it is immediately apparent that ϵ' for the BaCo Ferrite 02L composite has a very strong frequency dependence, starting high and dropping almost linearly from 1 MHz to 1 GHz. The BaCo Ferrite 02 composite shows this same behavior but appears to have overall smaller ϵ' values. For the remaining composites, NiZn Ferrite 01, BaCo Ferrite 01, and BaCo Ferrite 04, and the pure silicone, ϵ' is independent of frequency, showing constant ϵ' values over the frequency sweep. Additionally, the ϵ' values for the BaCo Ferrite 02L and BaCo Ferrite 02 composites are higher than the ϵ' values for the other composites.

By inspection of the ϵ'' as a function of frequency in Figure 4.10, the behavior of ϵ'' for the BaCo Ferrite 02L composite is once again immediately recognized as different. Over the 1 MHz to 1.8 GHz frequency sweep, the BaCo Ferrite 02L composite shows permittivity relaxation, that is, where a maximum ϵ'' occurs, at 1.503 GHz. Comparing to Figure 3.16, the permittivity relaxation for the pressed BaCo Ferrite 02L powder occurs at 1.401 GHz.

Also, the ϵ'' values for the BaCo Ferrite 02L and BaCo Ferrite 02 composites are much greater than the ϵ'' values for the other composites. For the remaining composites, NiZn Ferrite 01, BaCo Ferrite 01, and BaCo Ferrite 04, and the pure silicone, ϵ'' is independent of frequency, showing constant ϵ'' values over the frequency sweep.

Although $\tan\delta_\epsilon$ is obtained from dividing ϵ'' by ϵ' , it is shown in Figure 4.11 to be complete and also because it is a convenient property to compare loss that is normalized to permittivity property ϵ' . The $\tan\delta_\epsilon$ values for the BaCo Ferrite 02L and BaCo Ferrite 02 batches are greater than the $\tan\delta_\epsilon$ values for the other composites, even with the normalization.

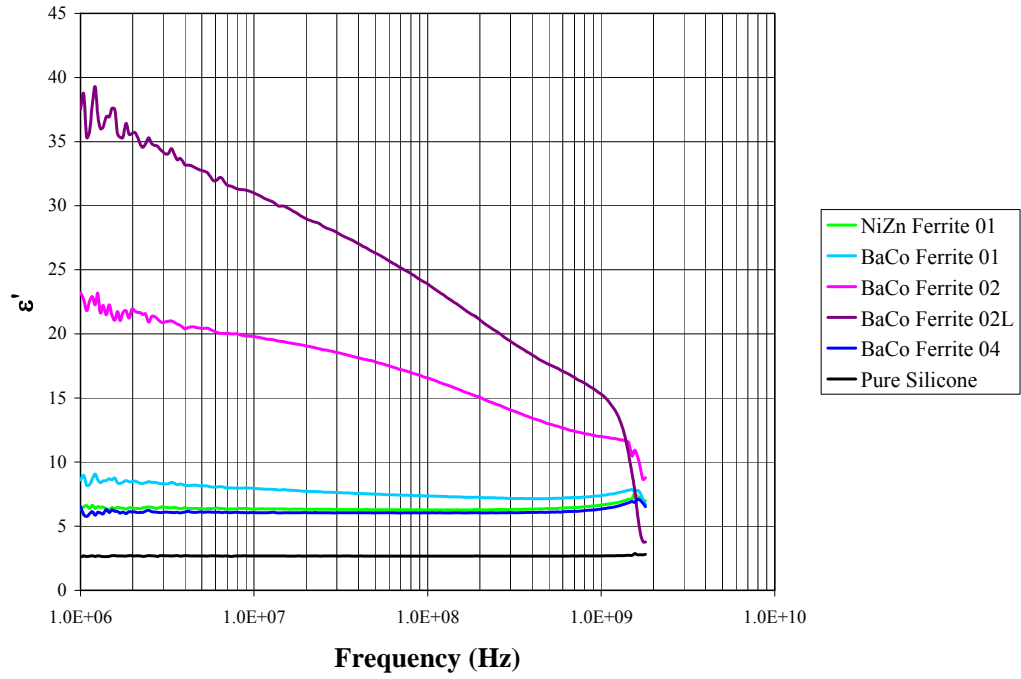


Figure 4.9: ϵ' versus frequency for composites comprised of different ferrite types

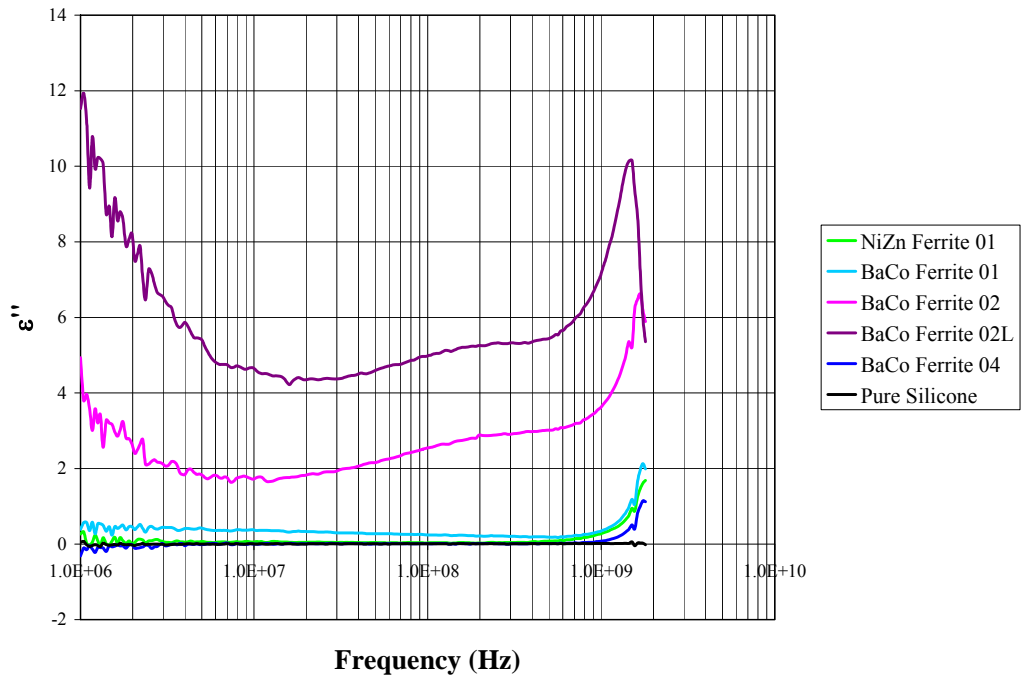


Figure 4.10: ϵ'' versus frequency for composites comprised of different ferrite types

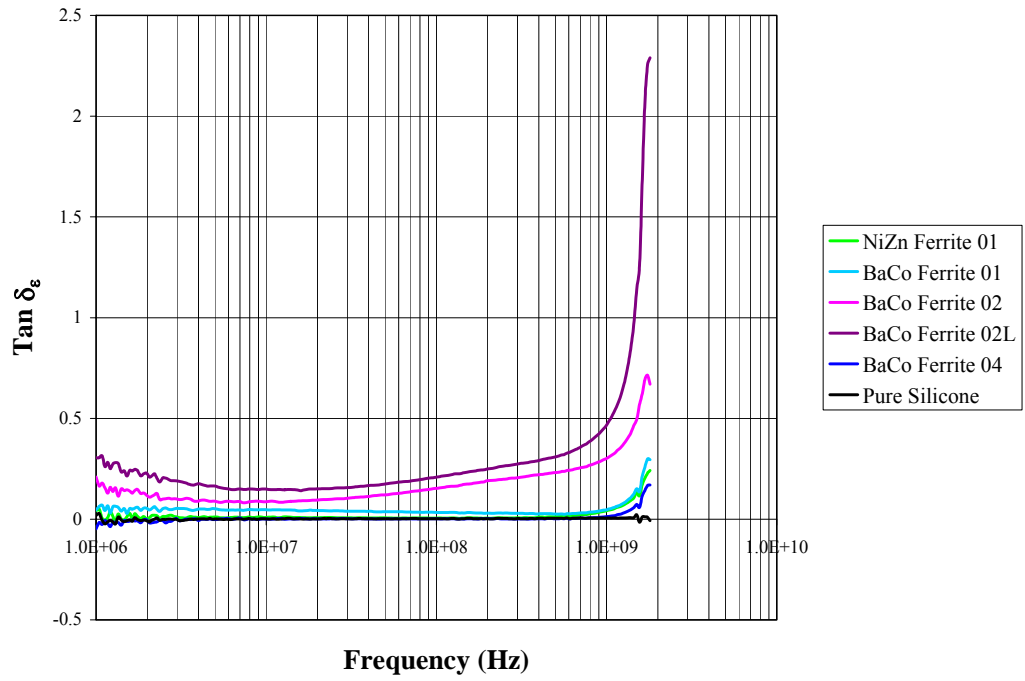


Figure 4.11: $\tan \delta_e$ versus frequency for composites comprised of different ferrite types

Permeability

The results of μ' , μ'' , and $\tan\delta_\mu$ as a function of frequency for composites comprised of the five ferrite types NiZn Ferrite 01, BaCo Ferrite 01, BaCo Ferrite 02, BaCo Ferrite 02L, and BaCo Ferrite 04 and pure silicone are shown in Figures 4.12, 4.13, and 4.14, respectively. By visual inspection of the permittivity behavior for the composites seen these figures, most notable is the difference in behavior seen for the NiZn Ferrite 01 composite compared to the other composites made from BaCo ferrite. In the figures, the μ^* behavior of the NiZn Ferrite 01 composite begins to show dependency on frequency beginning at about 20 MHz, whereas the other composites made from BaCo ferrite begin to show dependency on frequency beginning at about 200 MHz. As expected, the pure silicone shows magnetic property μ' equal to one and loss quantified as μ'' and $\tan\delta_\mu$ equal to zero.

In Figure 4.12, the value of μ' for the NiZn Ferrite 01 composite begins to decrease at about 20 MHz, whereas the values of μ' for the other composites BaCo Ferrite 01, BaCo Ferrite 02, BaCo Ferrite 02L, and BaCo Ferrite 04 begins to increase at about 200 MHz. Additionally, for the composites comprised on BaCo ferrite, the values of μ' for the composites BaCo Ferrite 02 and BaCo Ferrite 02L show similar behavior, and the values of μ' for the composites BaCo Ferrite 01 and BaCo Ferrite 04 show similar behavior. Specifically, beginning at about 200 MHz, the values of μ' for the BaCo Ferrite 02 and BaCo Ferrite 02L composites show a slower initial increase with frequency and then a similar increase toward the end of the frequency sweep compared to the BaCo Ferrite 01 and BaCo Ferrite 04 composites. Due to this behavior and the relative values of μ' for the composites, the values of μ' for the BaCo Ferrite 01 and BaCo Ferrite 02 composites cross at about 600 MHz. With respect to the relative values of μ' , the NiZn Ferrite has the largest constant

value of μ' . For the composites comprised on BaCo ferrite, the largest constant value of μ' is observed for the BaCo Ferrite 02L composite, which has the particle size distribution containing the largest particle sizes. The effect of the particle size distribution is explored in a later section. The next largest constant values of μ' are observed for the BaCo Ferrite 02 composite, then the BaCo Ferrite 01 composite, and finally the BaCo Ferrite 04 composite.

In Figure 4.13, the values of μ'' begin to depend on frequency at about the same frequencies as for the values of μ' . Specifically, the values of μ'' for NiZn Ferrite 01 begin to increase at about 20 MHz, and, for the other composites BaCo Ferrite 01, BaCo Ferrite 02, BaCo Ferrite 02L, and BaCo Ferrite 04 begin to increase at about 200 MHz. Additionally, the highest values of μ'' are observed for NiZn Ferrite 01 followed by the BaCo Ferrite 02L, then BaCo Ferrite 02, BaCo Ferrite 01, and finally BaCo Ferrite 04.

Although $\tan\delta_\mu$ is obtained from dividing μ'' by μ' , it is shown in Figure 4.14 to be complete and also because it is a convenient property to compare loss that is normalized to permeability property μ' . As expected, the behaviors of the $\tan\delta_\mu$ values are similar to that of the μ'' values, in that the values of $\tan\delta_\mu$ begin to depend on frequency at about the same frequencies of 20 and 200 MHz for the composites made from the NiZn ferrite and BaCo ferrite, respectively. Additionally, even with the normalization that the values of $\tan\delta_\mu$ provide, the highest values of $\tan\delta_\mu$ are observed for NiZn Ferrite 01 followed by the BaCo Ferrite 02L, then BaCo Ferrite 02, BaCo Ferrite 01, and finally BaCo Ferrite 04. A notable observation is that the BaCo Ferrite 02 composite showed a higher value of $\tan\delta_\mu$ compared to the BaCo Ferrite 01 composite, even though these composites had similar values of μ' .

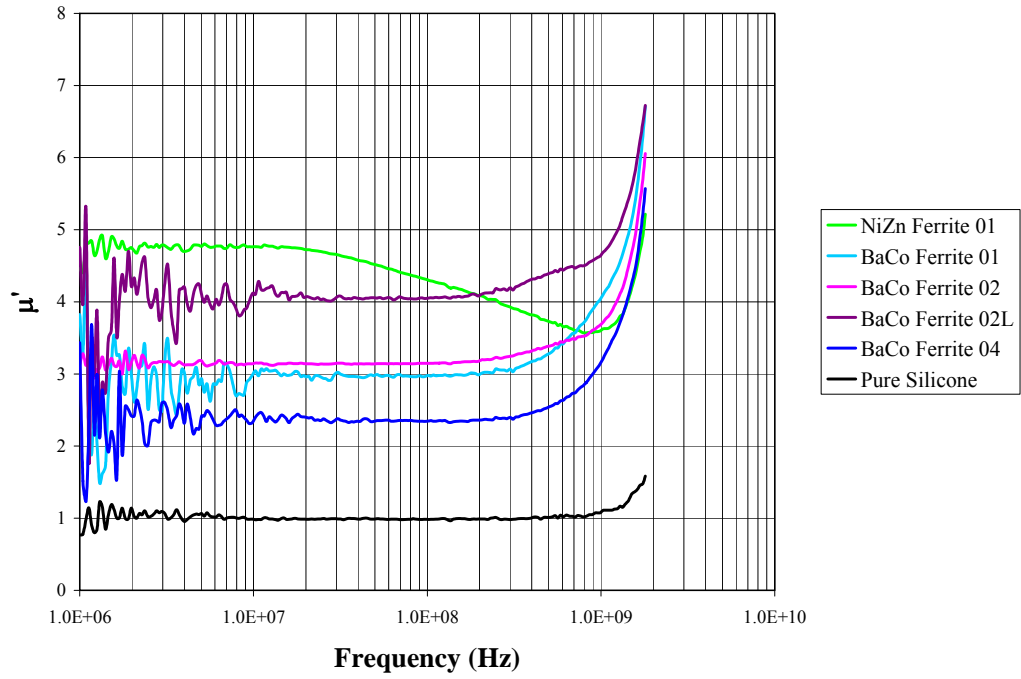


Figure 4.12: μ' versus frequency for composites comprised of different ferrite types

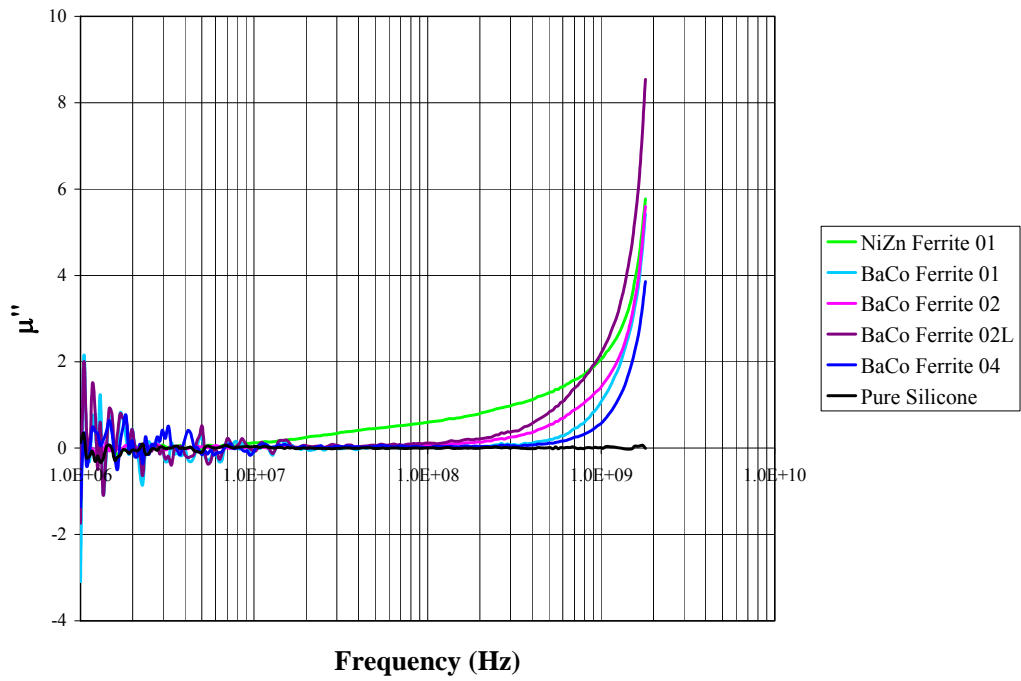


Figure 4.13: μ'' versus frequency for composites comprised of different ferrite types

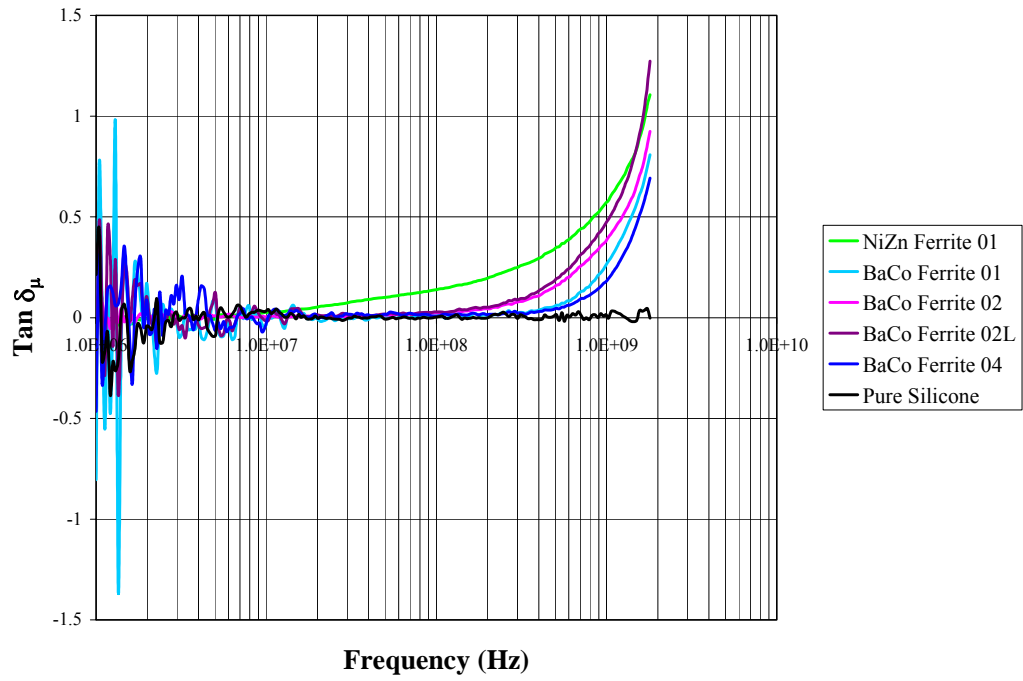


Figure 4.14: $\text{Tan } \delta_\mu$ versus frequency for composites comprised of different ferrite types

Sources of Variation

Variation of Measurements

Measurement variation for ϵ' and μ' was observed in the five measurements taken for each of the three formulations of composites made from BaCo Ferrite 02L and BaCo Ferrite 04. The measurement variation of ϵ' for the BaCo Ferrite 02L and BaCo Ferrite 04 composites is shown in Figures 4.15 and 4.16, respectively. The measurement variation of μ' for the BaCo Ferrite 02L and BaCo Ferrite 04 composites is shown in Figures 4.17 and 4.18, respectively. The identification convention in the figures includes denoting the ferrite batch from which the composite is made and the ending numbers denoting the formulation and measurement. For the example of BaCo Ferrite 02L – 1.3, the composite is made from the BaCo Ferrite 02L batch and the numbers 1.3 denote the first formulation and the third measurement, respectively.

By visual inspection of the Figures 4.15, 4.16, 4.17 and 4.18, it is immediately apparent that there is more variation in the measurements of ϵ' compared to that of μ' . In Figures 4.15 and 4.16, the variation in the measured values of ϵ' around 100 MHz is observed to be as great as 10% and more. In Figures 4.17 and 4.18, the variation in the measured values of μ' around 100 MHz is observed to be less than 5%. Further, there are some measurements that appear to be different than others, in particular, there is one measurement appearing different for a frequency sweep of ϵ' for the second formulation of BaCo Ferrite 02L composite in Figure 4.15 and another sweep of μ' of the third formulation of the BaCo Ferrite 02L composite in Figure 4.17. This observed variation in measurements of ϵ' and μ' substantiates the need to report an average value of measurements for any sample. As described previously, this work reports an average of five measurements for all samples.

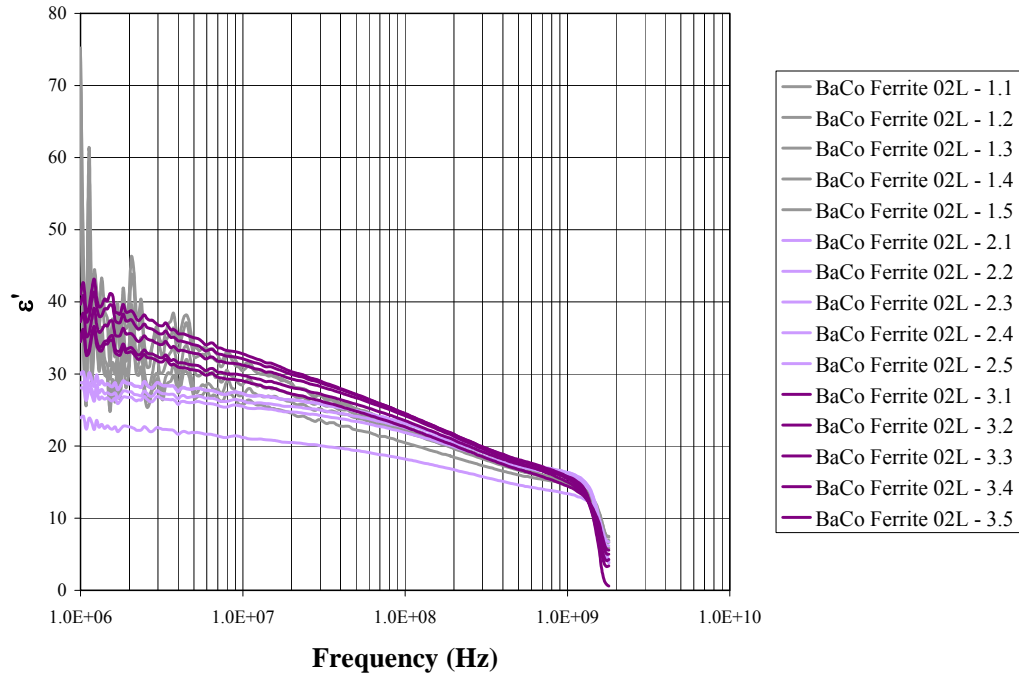


Figure 4.15: ϵ' versus frequency for measurements of BaCo Ferrite 02L composite formulations

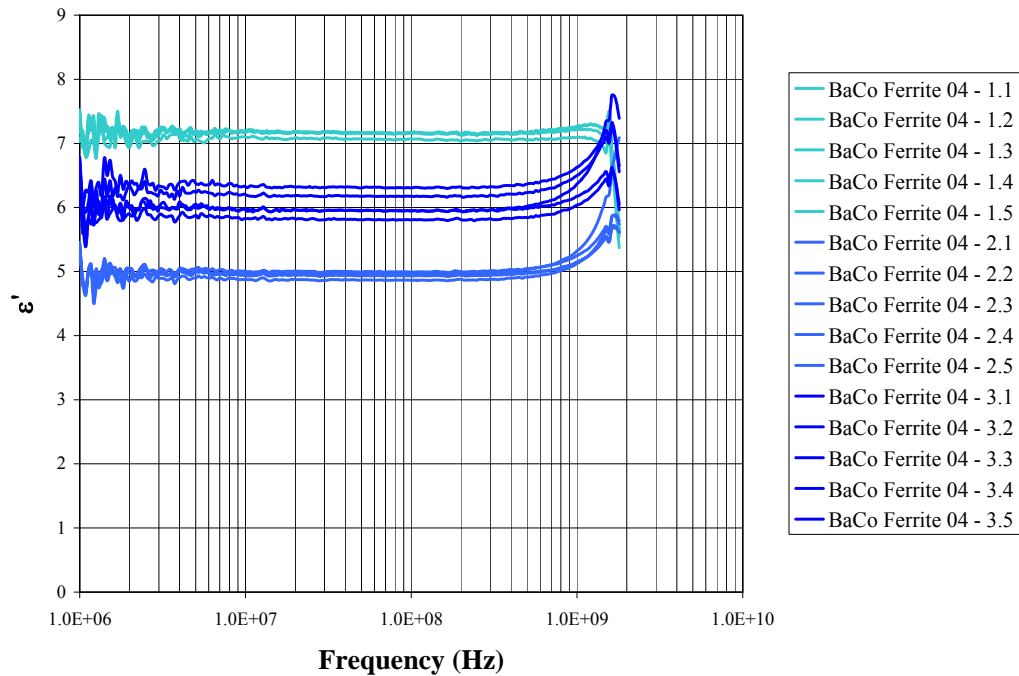


Figure 4.16: ϵ' versus frequency for measurements of BaCo Ferrite 04 composite formulations

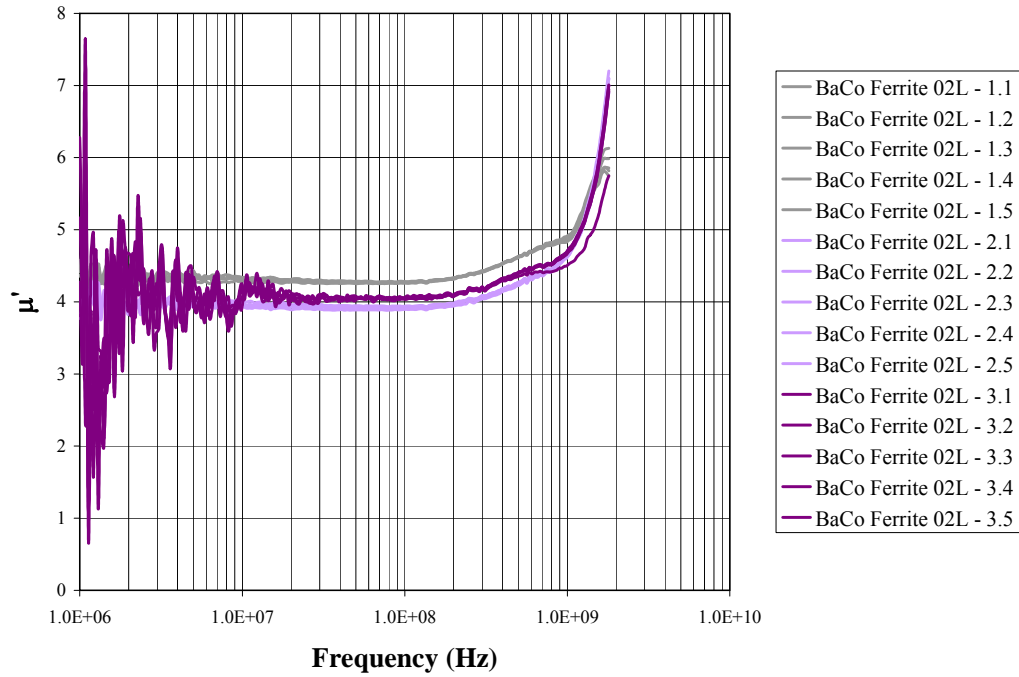


Figure 4.17: μ' versus frequency for measurements of BaCo Ferrite 02L composite formulations

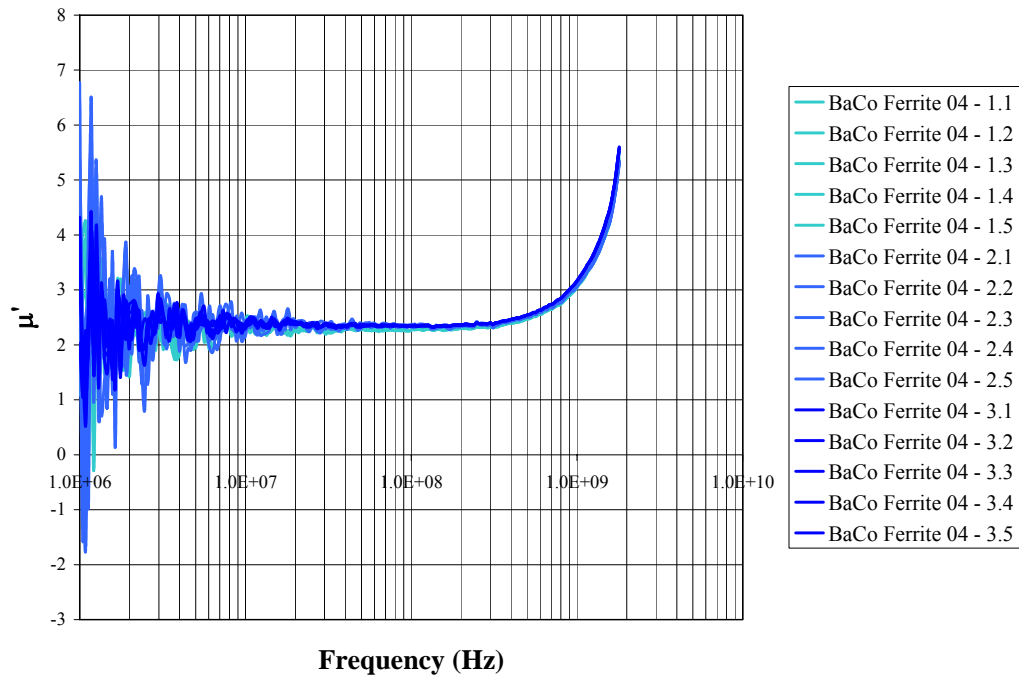


Figure 4.18: μ' versus frequency for measurements of BaCo Ferrite 04 composite formulations

Measurement variation for $\tan\delta_\epsilon$ and $\tan\delta_\mu$ was observed in the five measurements taken for each of the three formulations of composites made from BaCo Ferrite 02L and BaCo Ferrite 04. The measurement variation of $\tan\delta_\epsilon$ for the BaCo Ferrite 02L and BaCo Ferrite 04 composites is shown in Figures 4.19 and 4.20, respectively. The measurement variation of $\tan\delta_\mu$ for the BaCo Ferrite 02L and BaCo Ferrite 04 composites is shown in Figures 4.21 and 4.22, respectively. The identification convention in the figures is the same as that described for the previous figures, Figures 4.15, 4.16, 4.17 and 4.18.

By visual inspection of the Figures 4.19, 4.20, 4.21 and 4.22, there appears to be minimal variation for the scale shown. Overall, calculated variation at 100 MHz was smaller for $\tan\delta_\epsilon$ compared to $\tan\delta_\mu$. The lower loss BaCo Ferrite 04 composite has values of $\tan\delta_\epsilon$ and $\tan\delta_\mu$ that approach the limits of the instrument's capability to measure, making the variation higher for the measured $\tan\delta_\epsilon$ and $\tan\delta_\mu$ values compared to the BaCo Ferrite 02L composite. For measurement of $\tan\delta_\epsilon$, the variation calculated at 100 MHz was as high as 25% and 55% for the BaCo Ferrite 02L and BaCo Ferrite 04 composites, respectively. For measurement of $\tan\delta_\mu$, the variation calculated at 100 MHz was as high as about 20% and 100% for the BaCo Ferrite 02L and BaCo Ferrite 04 composites, respectively. Given the small values measured by the instrument, these variations are reasonable. Moreover, the observed variation in measurements of $\tan\delta_\epsilon$ and $\tan\delta_\mu$ substantiates the need to report an average value of measurements for any sample. As described previously, this work reports an average of five measurements for all samples.

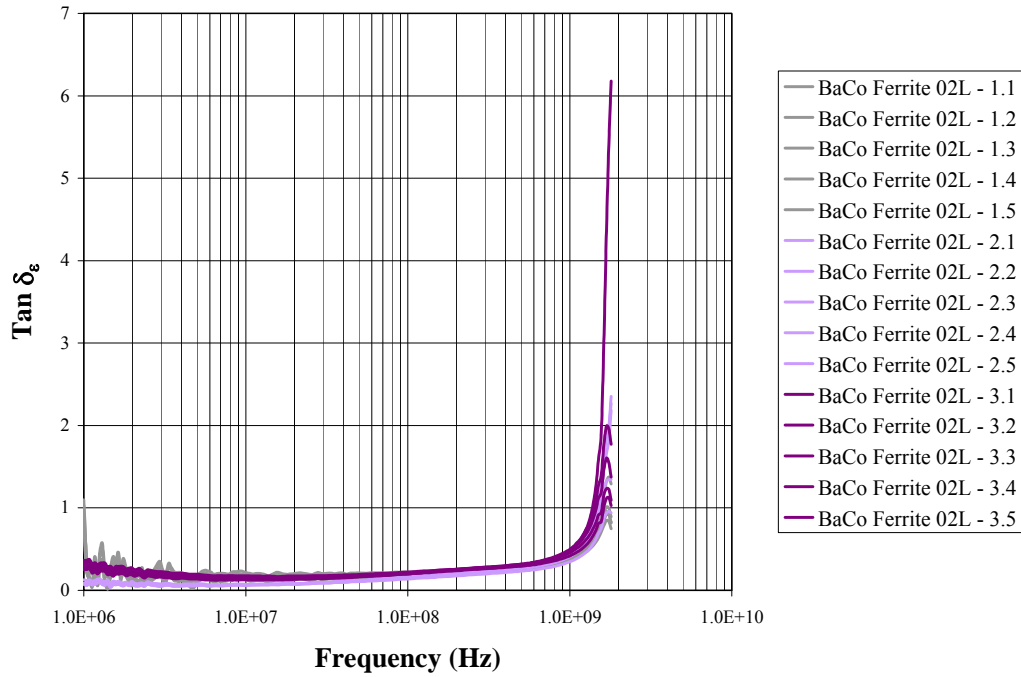


Figure 4.19: $\text{Tan}\delta_\epsilon$ versus frequency for measurements of BaCo Ferrite 02L composite formulations

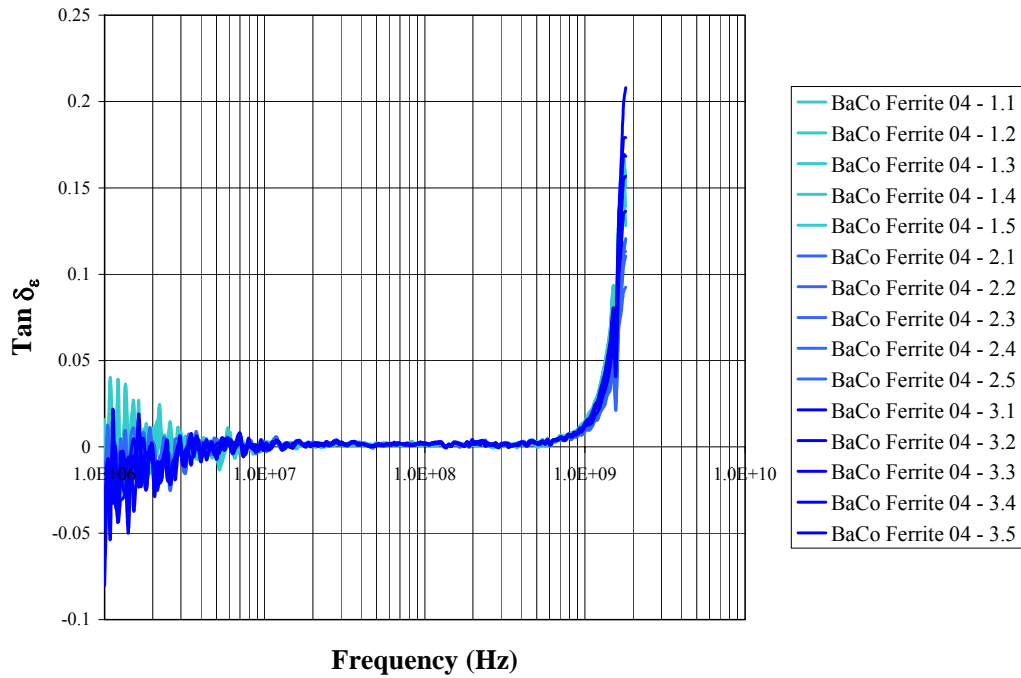


Figure 4.20: $\text{Tan}\delta_\epsilon$ versus frequency for measurements of BaCo Ferrite 04 composite formulations

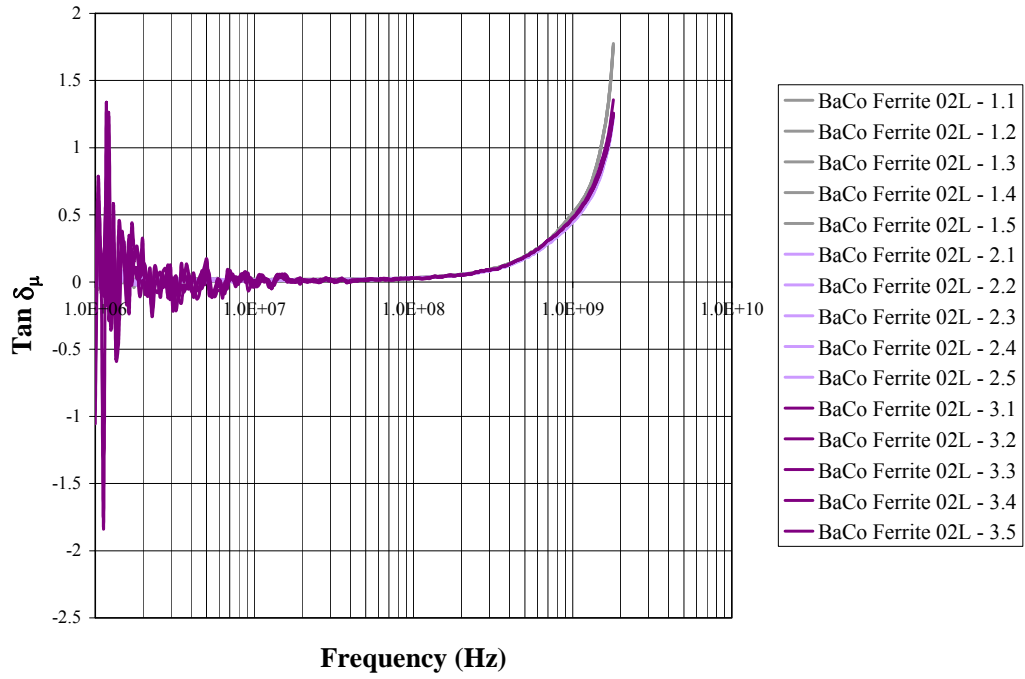


Figure 4.21: $\text{Tan } \delta_\mu$ versus frequency for measurements of BaCo Ferrite 02L composite formulations

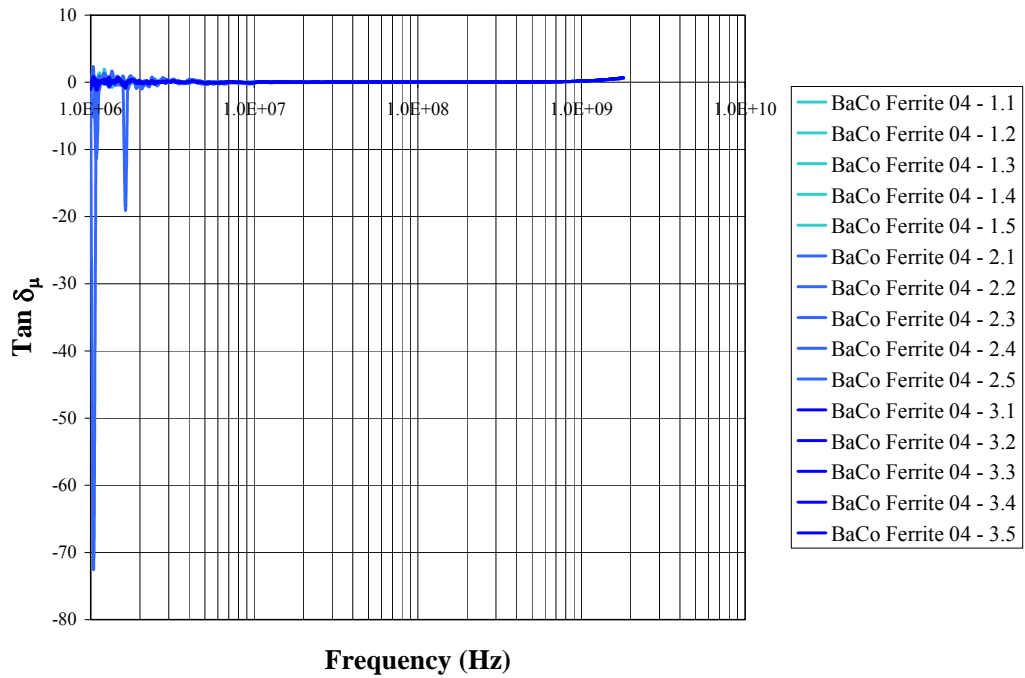


Figure 4.22: $\text{Tan } \delta_\mu$ versus frequency for measurements of BaCo Ferrite 04 composite formulations

Variation of Composite Formulations

To compare variation of composite formulations, the averages were determined for the BaCo Ferrite 02L and BaCo Ferrite 04 composites measurements shown in Figures 4.15, 4.16, 4.17, and 4.18 and combined into individual plots for ϵ' and μ' in Figures 4.23 and 4.24, respectively. Likewise, the averages were determined for the BaCo Ferrite 02L and BaCo Ferrite 04 composites measurements shown in Figures 4.19, 4.20, 4.21, and 4.22 and combined into individual plots for $\tan\delta_\epsilon$ and $\tan\delta_\mu$ in Figures 4.25 and 4.26, respectively. By visual inspection of the average ϵ' and μ' values for the composites at 100 MHz, the values of ϵ' are observed to vary as much as 10% and more, and the values of μ' are observed to vary as much as about 10%. Due to the small values measured for $\tan\delta_\epsilon$ and $\tan\delta_\mu$, the variation at 100 MHz was calculated and found to be about 30% for $\tan\delta_\epsilon$ and about 75% for $\tan\delta_\mu$. As previously observed, the high variation in $\tan\delta_\mu$ was determined for the lower loss BaCo Ferrite 04 composite, which has values of $\tan\delta_\mu$ that approach the instrument's capability to measure.

The variation due to repeatability of measurements is decreased by using the average and, therefore, provides reasonable basis to compare reproducibility of the formulations. The variation of formulations seen here to be as much as 10% and more for ϵ' and as much as about 10% for μ' is additional variation considered in further comparisons. Also, with this variation present, the behavior, or shape, of the values extracted from the ϵ^* and μ^* properties as a function of frequency, is also considered in further comparisons. So far, the behaviors of the ϵ^* and μ^* properties are observed to be highly repeatable and reproducible in both the measurements and formulations, respectively, for the different composites investigated.

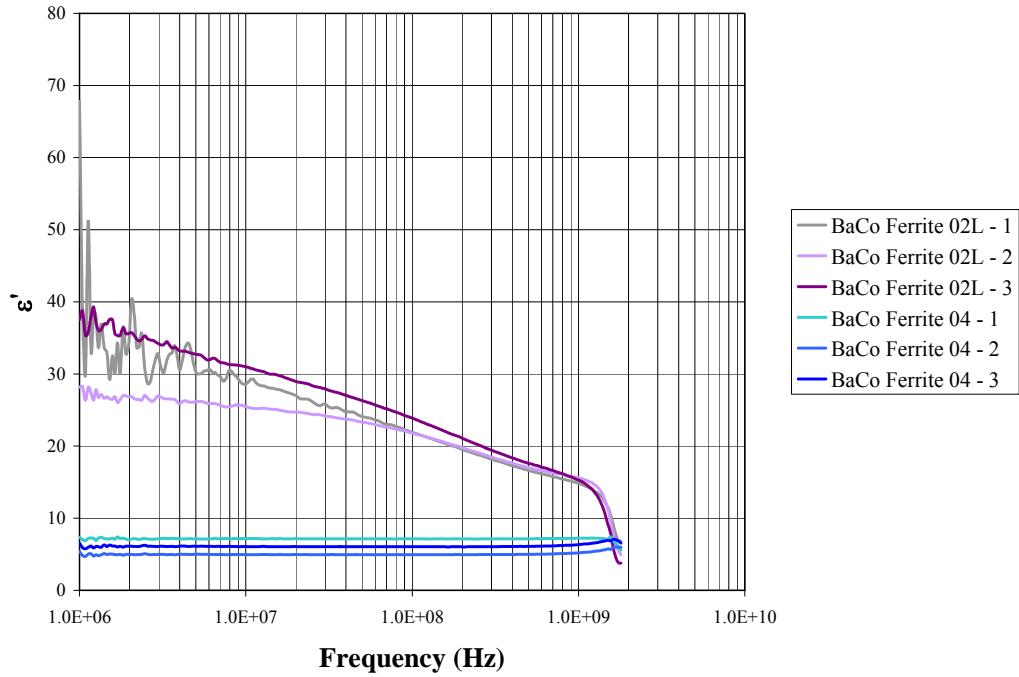


Figure 4.23: ϵ' versus frequency for different formulations of composites made from BaCo Ferrite 02L and BaCo Ferrite 04

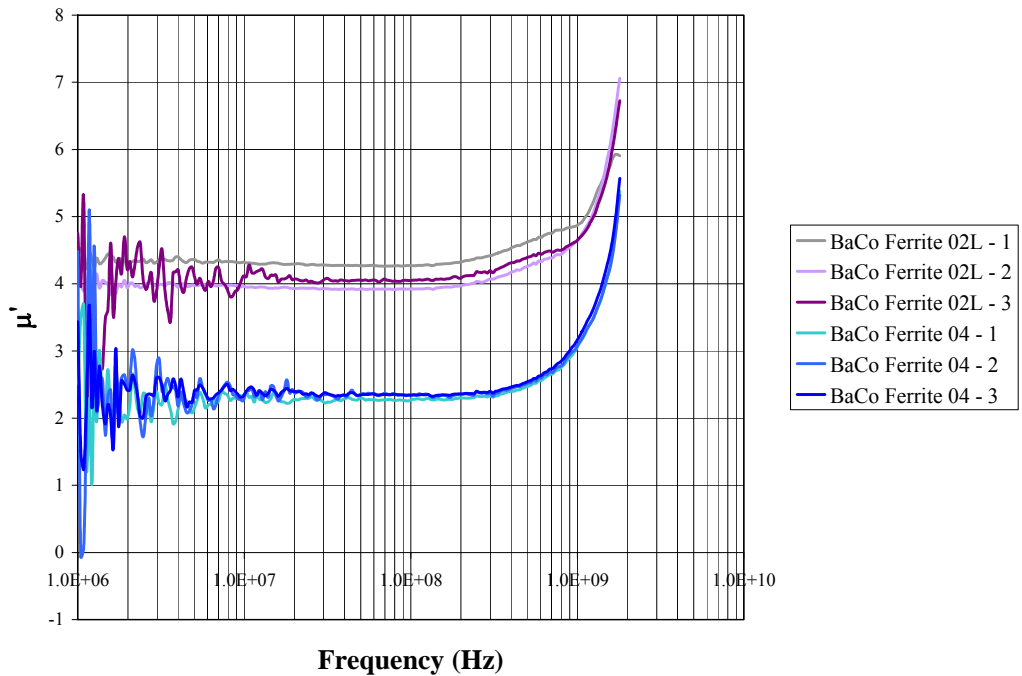


Figure 4.24: μ' versus frequency for different formulations of composites made from BaCo Ferrite 02L and BaCo Ferrite 04

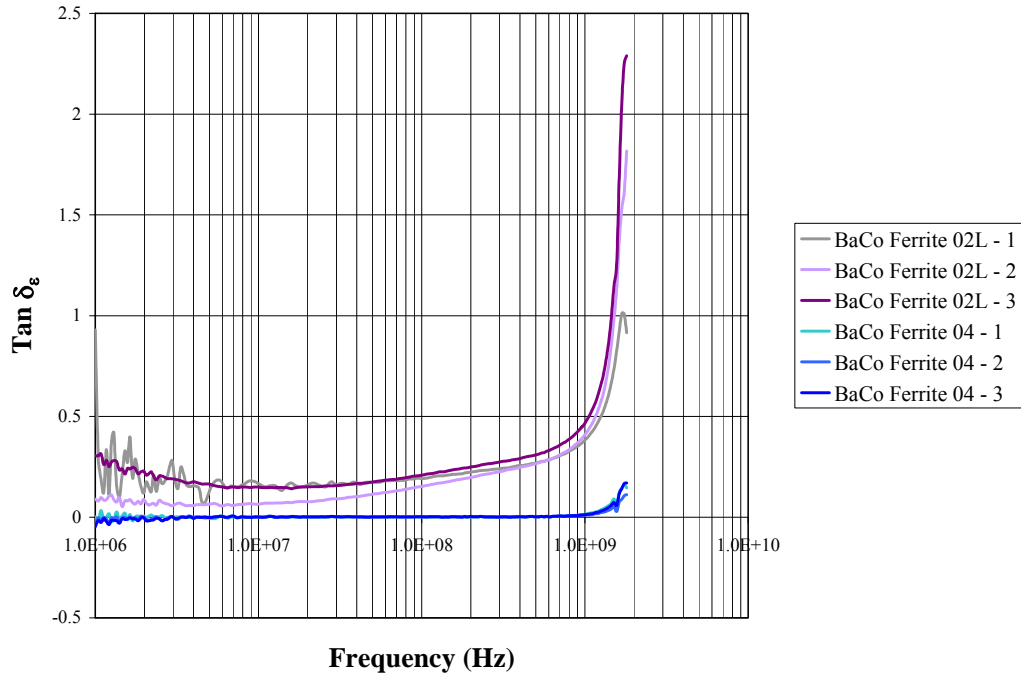


Figure 4.25: $\text{Tan}\delta_\epsilon$ versus frequency for different formulations of composites made from BaCo Ferrite 02L and BaCo Ferrite 04

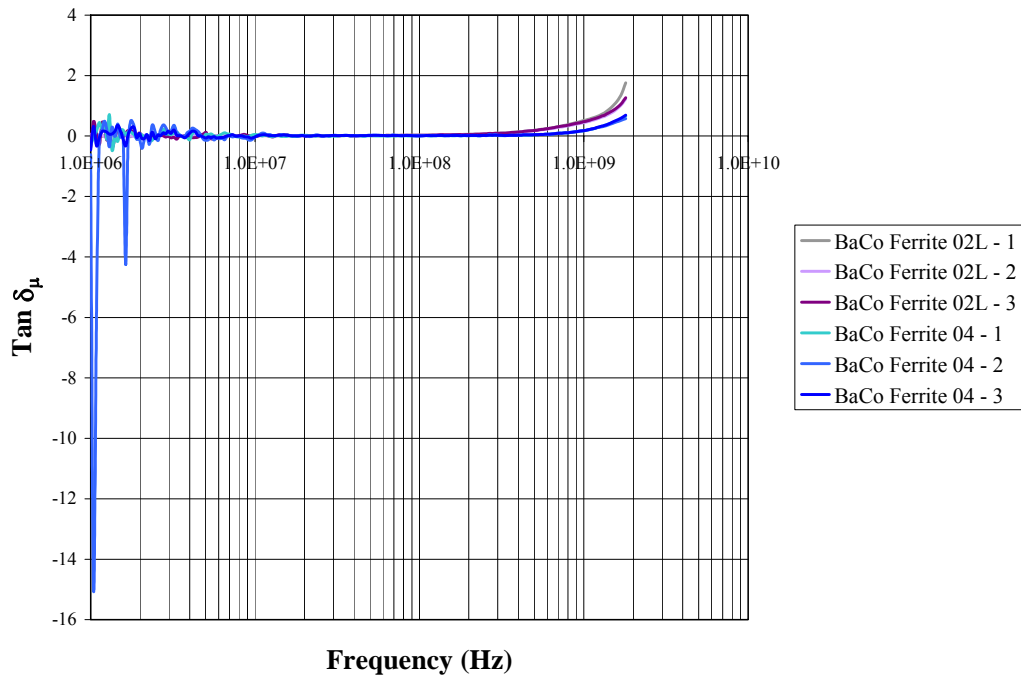


Figure 4.26: $\text{Tan}\delta_\mu$ versus frequency for different formulations of composites made from BaCo Ferrite 02L and BaCo Ferrite 04

Effect of Coupling Agent

Coefficient of Thermal Expansion

To investigate effect of the silane coupling agent used in formulation of the composites, the coefficient of thermal expansion (CTE) values were obtained and compared. The CTE values for the composites NiZn Ferrite 01 as the experimental control, 0.5 wt% silane, 1.0 wt% silane, and 1.5 wt% silane are given in Figure 4.27. In Figure 4.27, both the first and second CTE values measured are shown, denoted by CTE – 1 and CTE – 2, respectively. By inspection of the relative CTE values, the composites formulated with silane are similar to the NiZn Ferrite 01 composite, indicating no detectable effect of the silane on CTE.

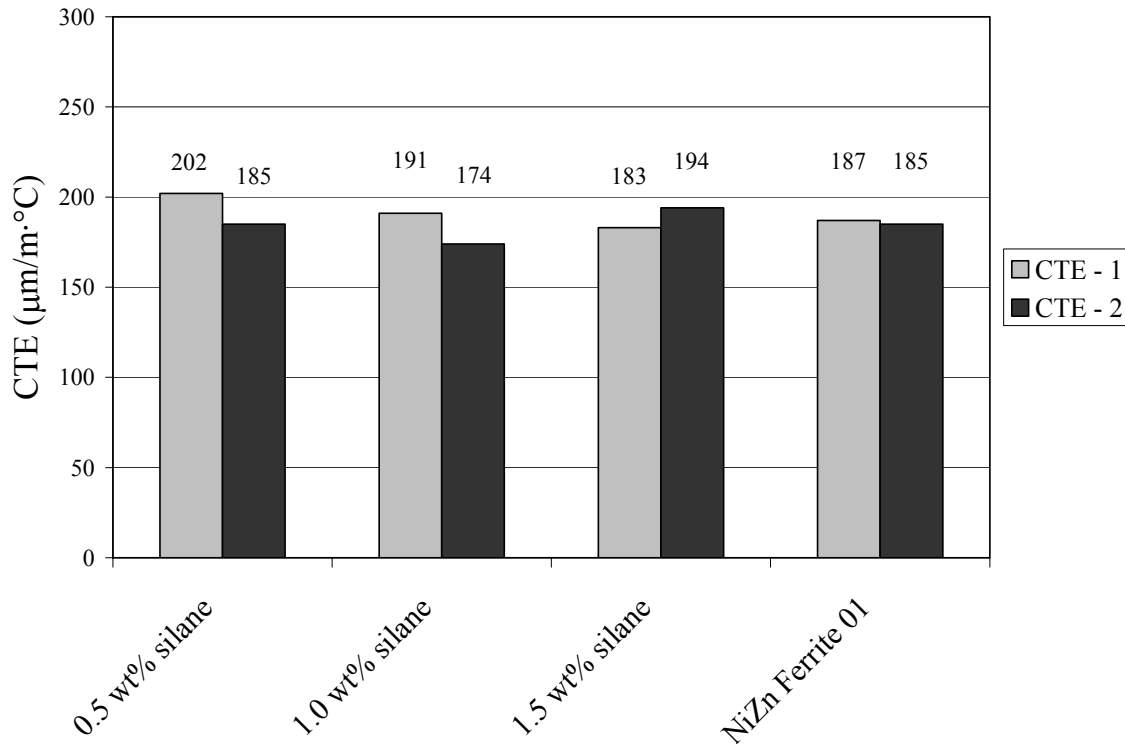


Figure 4.27: CTE values for samples including composites comprised of NiZn Ferrite 01 as experimental control, fabricated with different coupling agent treatments 0.5 wt% silane, 1.0 wt% silane, and 1.5 wt% silane. Both the first and second CTE values measured are shown, denoted by CTE – 1 and CTE – 2, respectively.

Complex Young's Modulus

To investigate effect of the silane coupling agent used in formulation of the composites, complex Young's modulus (E^*) values, including both storage modulus (E') and loss modulus (E''), were obtained and compared. The E' and E'' values for the composites NiZn Ferrite 01 as the experimental control, 0.5 wt% silane, 1.0 wt% silane, and 1.5 wt% silane are given in Figure 4.28 and 4.29, respectively. In the figures, the measured values for both the first and second tests are shown, denoted by dotted lines and regular lines, respectively. By inspection of the relative E' and E'' values, the composites formulated with silane are similar to the NiZn Ferrite 01 composite, indicating no detectable effect of the silane on E' or E'' .

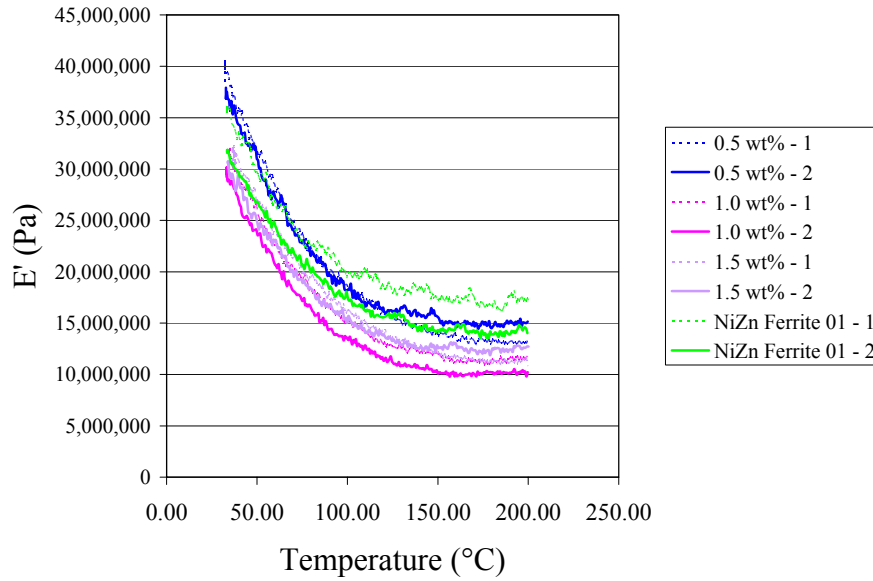


Figure 4.28: E' values for the composites NiZn Ferrite 01 as the experimental control, 0.5 wt% silane, 1.0 wt% silane, and 1.5 wt% silane. Measured values for both the first and second tests are shown, denoted by dotted lines and regular lines, respectively. The first test is to remove thermal history and the second test to obtain comparable values of E' and E'' for the samples.

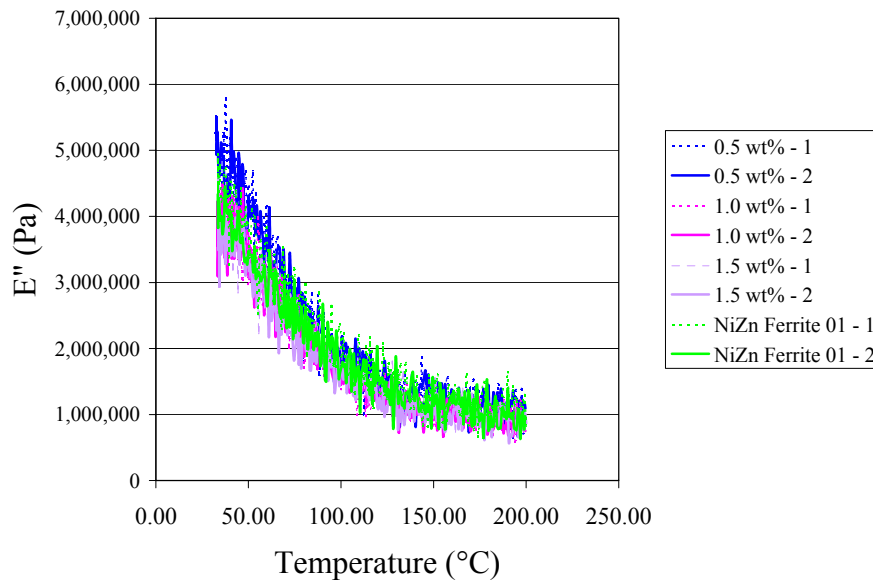


Figure 4.29: E'' values for the composites NiZn Ferrite 01 as the experimental control, 0.5 wt% silane, 1.0 wt% silane, and 1.5 wt% silane. Measured values for both the first and second tests are shown, denoted by dotted lines and regular lines, respectively. The first test is to remove thermal history and the second test to obtain comparable values of E' and E'' for the samples.

Permittivity

To further investigate the effect of the silane coupling agent used in formulation of the composite, the ϵ' , ϵ'' , and $\tan\delta_\epsilon$ values as a function of frequency were obtained and compared. The values of ϵ' , ϵ'' , and $\tan\delta_\epsilon$ as a function of frequency for the composites NiZn Ferrite 01, 0.5 wt% silane, 1.0 wt% silane, and 1.5 wt% silane are given in Figure 4.30, 4.31, and 4.32, respectively. In the figures, the values for the NiZn Ferrite 01 composite are the same as those shown previously in Figures 4.9, 4.10, and 4.11, because the NiZn Ferrite 01 composite serves as the experimental control. The values of ϵ' , ϵ'' , and $\tan\delta_\epsilon$ as a function of frequency for the composites formulated with silane are similar to the NiZn Ferrite 01 composite, indicating no detectable effect of the silane on permittivity.

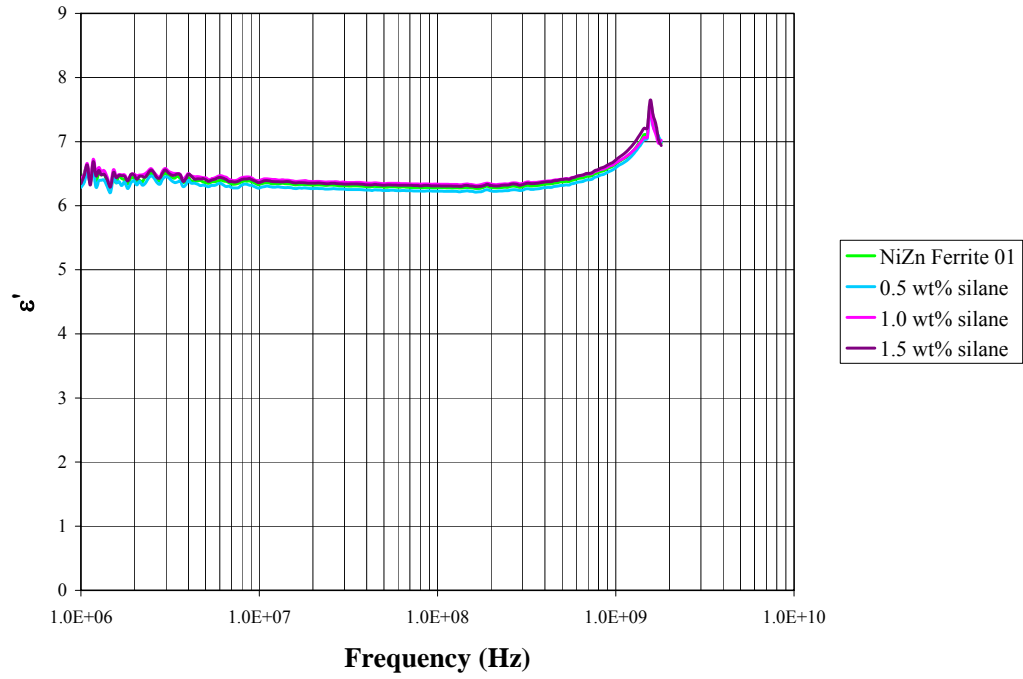


Figure 4.30: ϵ' versus frequency for different coupling agent treatments

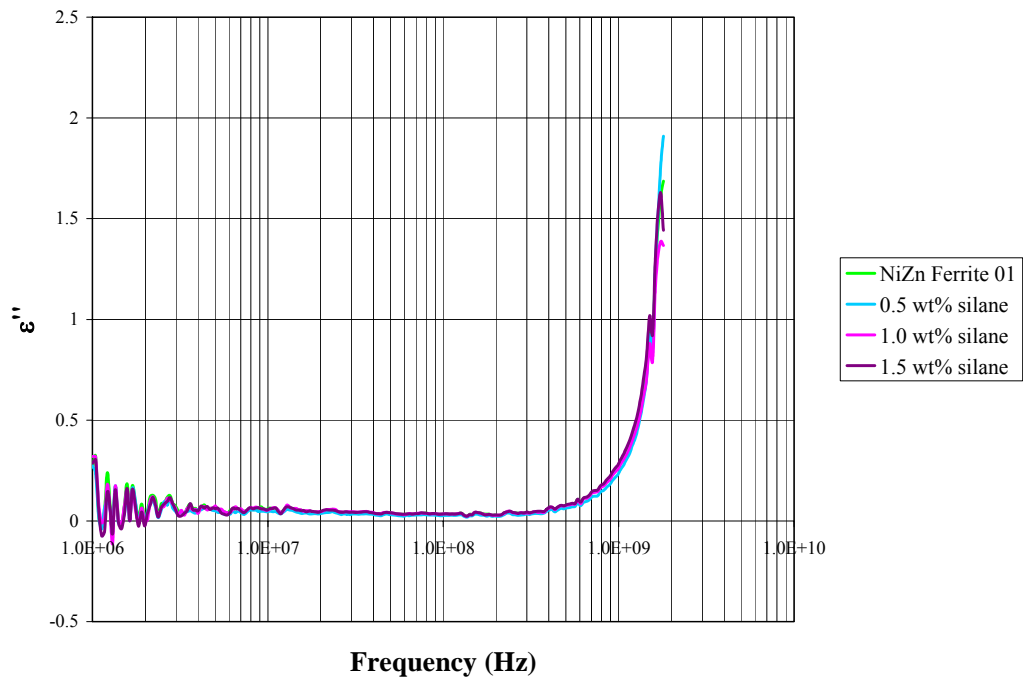


Figure 4.31: ϵ'' versus frequency for different coupling agent treatments

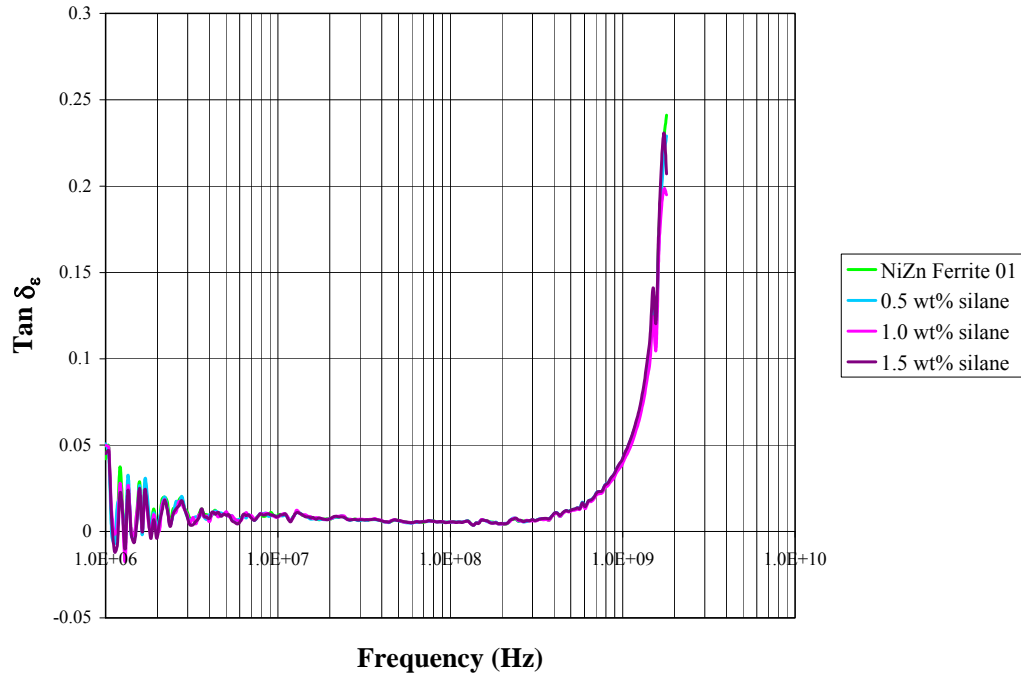


Figure 4.32: $\tan \delta_\epsilon$ versus frequency for different coupling agent treatments

Permeability

To continue investigation of the effect of the silane coupling agent used in formulation of the composite, the μ' , μ'' , and $\tan\delta_\mu$ values as a function of frequency were obtained and compared. The values of μ' , μ'' , and $\tan\delta_\mu$ as a function of frequency for the composites NiZn Ferrite 01, 0.5 wt% silane, 1.0 wt% silane, and 1.5 wt% silane are given in Figure 4.33, 4.34, and 4.35, respectively. In the figures, the values for the NiZn Ferrite 01 composite are the same as those shown previously in Figures 4.12, 4.13, and 4.14, because the NiZn Ferrite 01 composite serves as the experimental control. The values of ϵ' , ϵ'' , and $\tan\delta_\epsilon$ as a function of frequency for the composites formulated with silane are similar to the NiZn Ferrite 01 composite, indicating no detectable effect of the silane on permeability.

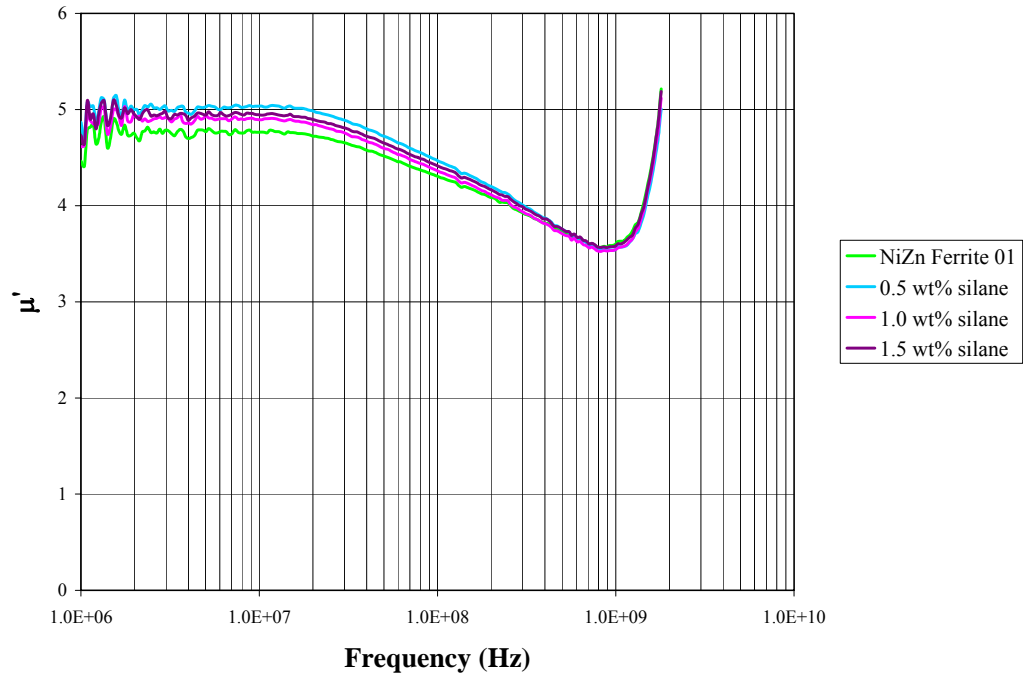


Figure 4.33: ϵ' versus frequency for different coupling agent treatments

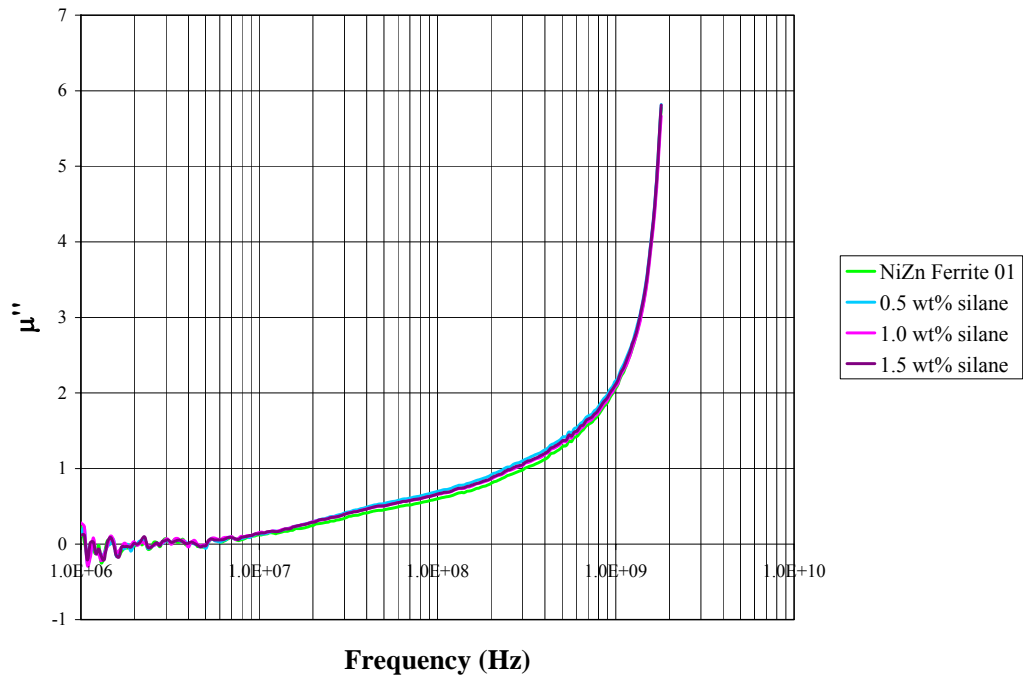


Figure 4.34: ϵ'' versus frequency for different coupling agent treatments

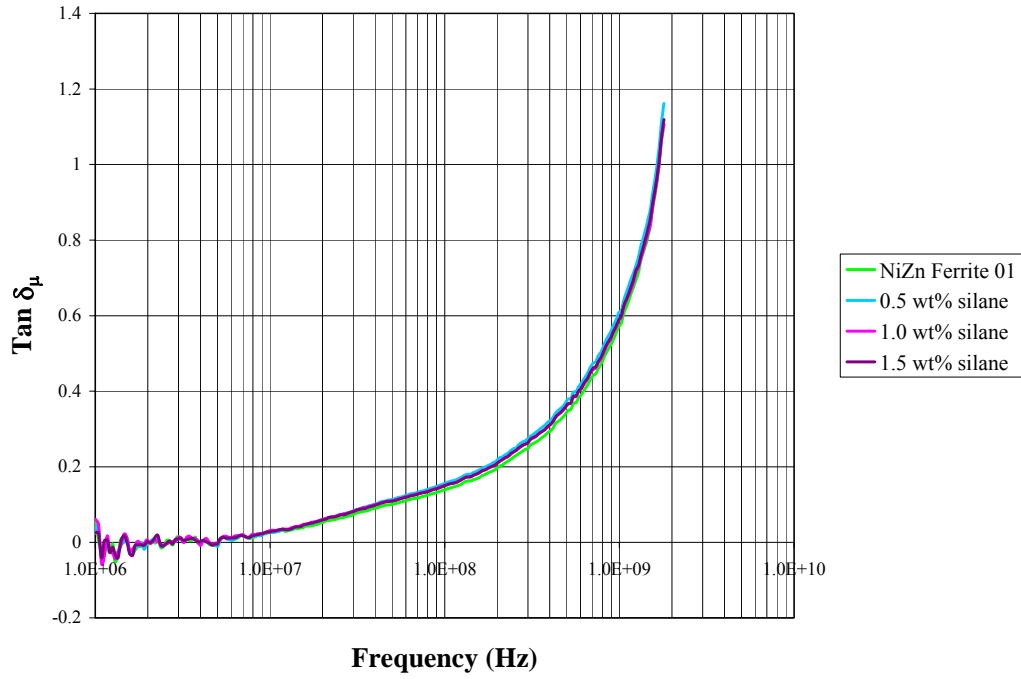


Figure 4.35: $\tan \delta_\mu$ versus frequency for different coupling agent treatments

Effect of Particle Size Distribution

Permittivity and Permeability

The measurements of ϵ' , μ' , $\tan\delta_\epsilon$, and $\tan\delta_\mu$ as a function of frequency for the composites BaCo Ferrite 02L-1, BaCo Ferrite 02L-2, BaCo Ferrite 02L-3, and BaCo Ferrite 02-1 were combined in individual plots in order to compare effect of particle size distribution. As previously described, the identification convention includes denoting the ferrite batch from which the composite is made and the ending number denoting the composite formulation. For the example of BaCo Ferrite 02L – 1, the composite is made from the BaCo Ferrite 02L batch and the number 1 denotes the first composite formulation. Losses quantified as $\tan\delta_\epsilon$, and $\tan\delta_\mu$ were used for the comparison because they are the normalized losses, which provide a more rigorous comparison. These plots of ϵ' , μ' , $\tan\delta_\epsilon$, and $\tan\delta_\mu$ as a function of frequency are shown in Figures 4.36, 4.37, 4.38 and 4.39, respectively. Referencing Table 3.7, the particle size distribution for the composites BaCo Ferrite 02L-1, BaCo Ferrite 02L-2, and BaCo Ferrite 02L-3 is 45-250 μm , whereas it is 45-150 μm for composite BaCo Ferrite 02-1. Due to the previously observed sources of variation, investigating the electromagnetic properties for composites having different particle size distributions but with particles coming from the same ferrite batch provides a sound comparison. By inspection of the plots shown in Figures 4.36, 4.37, 4.38 and 4.39, it appears the particle size distribution including larger particles (i.e. 45-250 μm) may provide higher values for ϵ' , μ' , $\tan\delta_\epsilon$, and $\tan\delta_\mu$ compared to the other particle size distribution (i.e. 45-150 μm).

To achieve confidence in the comparisons, statistical analyses were used to determine significant differences due to particle size distribution for ϵ' , μ' , $\tan\delta_\epsilon$, and $\tan\delta_\mu$. In order to

perform the comparisons, the point values of ϵ' , μ' , $\tan\delta_\epsilon$, and $\tan\delta_\mu$ at 400 MHz were used. This frequency was used because it is in the center of the lower UHF spectrum (~300-500 MHz), which is the frequency band of interest for the application in this work. The point values of ϵ' , μ' , $\tan\delta_\epsilon$, and $\tan\delta_\mu$ extracted from the raw data used to plot Figures 4.36, 4.37, 4.38 and 4.39, respectively, are given in Table 4.1. The values in Table 4.1 are the data on which the statistical analyses were performed.

To perform the statistical analysis, the Fit Y by X platform in JMP software was used [77]. Results of the statistical analyses on ϵ' , μ' , $\tan\delta_\epsilon$, and $\tan\delta_\mu$ for the different composites compared are shown in Figures 4.40, 4.41, 4.42 and 4.43, respectively. In the figures, data points are represented by bold dots and are shown with error bars of one standard error. Means diamonds are shown, and the lines across the diamonds represent the group means. Means of the groups are connected. Diamond heights are 95% confidence intervals and diamond widths represent group sample sizes. Horizontal lines seen outside of and on the diamonds represent one standard deviation. The comparison circles to the right represent the population for the conditions at the 95% confidence interval. In the individual figures, the red circle represents the group being compared and gray circles represent groups that are significantly different by the Tukey-Kramer test at the 95% confidence level.

For the analysis of ϵ' , the comparison circles to the right in Figure 4.40 sufficiently overlap for the composites BaCo Ferrite 02L – 1, BaCo Ferrite 02L – 2, and BaCo Ferrite 02L – 3, supporting that there is no statistically significant difference among these composites at the 95% confidence level. However, the comparison circle for the composites BaCo Ferrite 02 – 1 does not overlap the comparison circles for the composites BaCo Ferrite 02L – 1, BaCo Ferrite 02L – 2, and BaCo Ferrite 02L – 3, supporting that the composites

BaCo Ferrite 02 – 1 has a significantly lower value for ε' compared to the other composites BaCo Ferrite 02L – 1, BaCo Ferrite 02L – 2, and BaCo Ferrite 02L – 3 at the 95% confidence level.

For the analysis of μ' , the comparison circles to the right in Figure 4.41 do not overlap for the composites BaCo Ferrite 02 – 1, BaCo Ferrite 02L – 1, BaCo Ferrite 02L – 2, and BaCo Ferrite 02L – 3, supporting that all composites have significantly different values at the 95% confidence level. Additionally, because all composites have statistically different values for μ' and by inspection of the relative location of the group means for μ' , the composite BaCo Ferrite 02 – 1 has a significantly lower value for μ' compared to the other composites BaCo Ferrite 02L – 1, BaCo Ferrite 02L – 2, and BaCo Ferrite 02L – 3 at the 95% confidence level.

For the analysis of $\tan\delta_\varepsilon$, the comparison circles to the right in Figure 4.42 are sufficiently far apart for the composite BaCo Ferrite 02 to have significantly lower mean value for $\tan\delta_\varepsilon$ compared to the composites BaCo Ferrite 02L – 1, BaCo Ferrite 02L – 2, and BaCo Ferrite 02L – 3 at the 95% confidence level. Also, the comparison circle for the composite BaCo Ferrite 02L – 3 is sufficiently far apart from the comparison circles for the composites BaCo Ferrite 02L – 1 and BaCo Ferrite 02L – 2, such that the composite BaCo Ferrite 02L – 3 has a significantly higher mean value for $\tan\delta_\varepsilon$ compared to the composites BaCo Ferrite 02L – 1 and BaCo Ferrite 02L – 2.

For the analysis of $\tan\delta_\mu$, the comparison circles to the right in Figure 4.43 do not overlap for the composites BaCo Ferrite 02 – 1, BaCo Ferrite 02L – 1, BaCo Ferrite 02L – 2, and BaCo Ferrite 02L – 3, supporting that all composites have significantly different values at the 95% confidence level. Additionally, because all composites have statistically different

values for $\tan\delta_{\mu}$ and by inspection of the relative location of the group means for $\tan\delta_{\mu}$, the composite BaCo Ferrite 02 – 1 has a significantly lower value for $\tan\delta_{\mu}$ compared to the other composites BaCo Ferrite 02L – 1, BaCo Ferrite 02L – 2, and BaCo Ferrite 02L – 3 at the 95% confidence level.

The assumptions of normality and equal variances for the groups were investigated in order to validate use of the Tukey-Kramer tests, which includes the comparison circles. The assumptions of normality and equal variances were validated for the $\tan\delta_{\epsilon}$ comparison. However, the assumptions of equal variances were validated but the assumptions of normality was not validated for the ϵ' , μ' , $\tan\delta_{\mu}$ comparisons. Although the assumptions could not be validated for the ϵ' , μ' , $\tan\delta_{\mu}$ comparisons, the Tukey-Kramer tests are somewhat robust to these assumptions and the accompanying comparison circles provide a useful visuals for comparing the groups of data.

Because the assumptions of normality and equal variances for the groups could not be validated for all comparisons and in order to ensure valid statistical methods were used for the comparisons, nonparametric comparative methods were applied. The nonparametric comparison tests used were the Wilcoxon / Kruskal-Wallis Tests, the Median Tests, and the Van der Waerden Tests. All three tests employed both the normal and the Chi square approximations. The data were separated into one of two groups, namely, particle size distribution of 45-150 μm or 45-250 μm , and then compared for mean values of ϵ' , μ' , $\tan\delta_{\epsilon}$, and $\tan\delta_{\mu}$. The p-values for the tests were then compared to the assumed α risk of 0.05. P-values less than 0.05 indicate there is a statistically significant difference between the groups at the 95% confidence level. The results of the tests showed all p-values to be less than 0.05. The actual p-values for the tests are shown in Tables 4.2, 4.3, 4.4, and 4.5. These p-values

provides valid statistical support at the 95% confidence level for all results found previously in the Tukey-Kramer analyses relative to differences in mean values of ϵ' , μ' , $\tan\delta_\epsilon$, $\tan\delta_\mu$ for composites with ferrite size distributions of 45-150 μm compared to 45-250 μm . In summary, composites with ferrite size distributions of 45-150 μm have significantly lower values of ϵ' , μ' , $\tan\delta_\epsilon$, and $\tan\delta_\mu$ compared to composites with ferrite size distributions of 45-250 μm at the 95% confidence level.

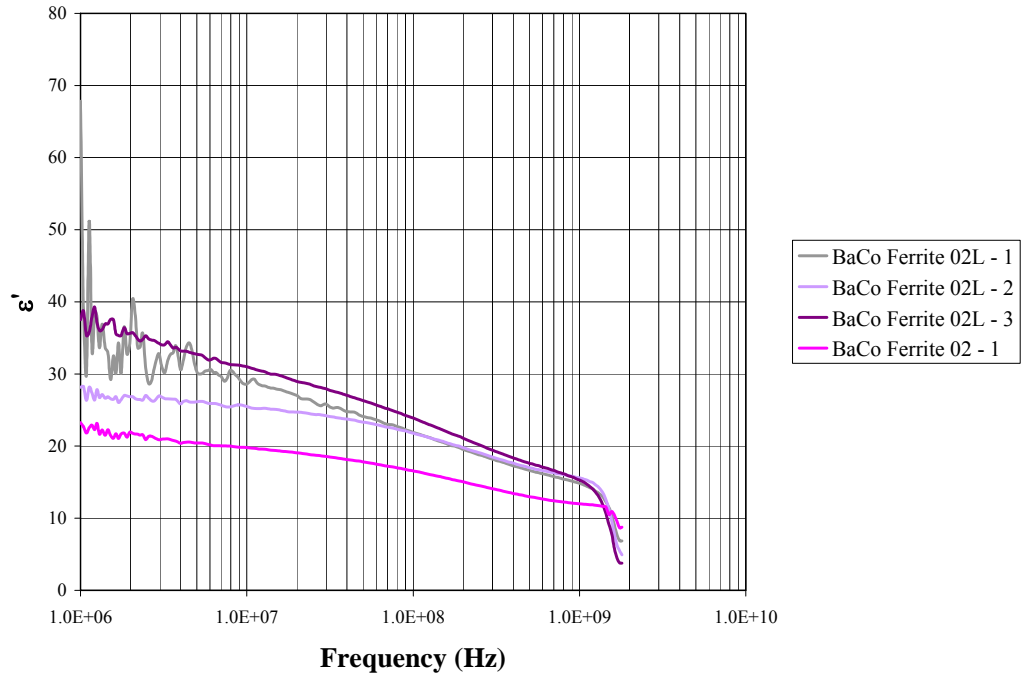


Figure 4.36: ϵ' versus frequency for composites made from BaCo Ferrite 02L and BaCo Ferrite 02

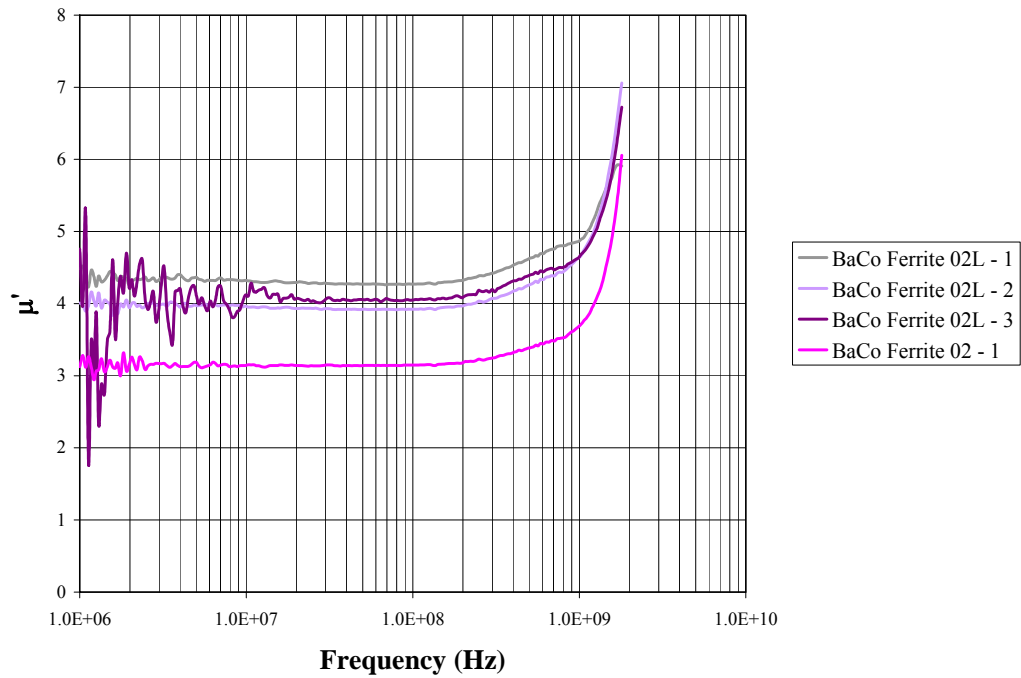


Figure 4.37: μ' versus frequency for composites made from BaCo Ferrite 02L and BaCo Ferrite 02

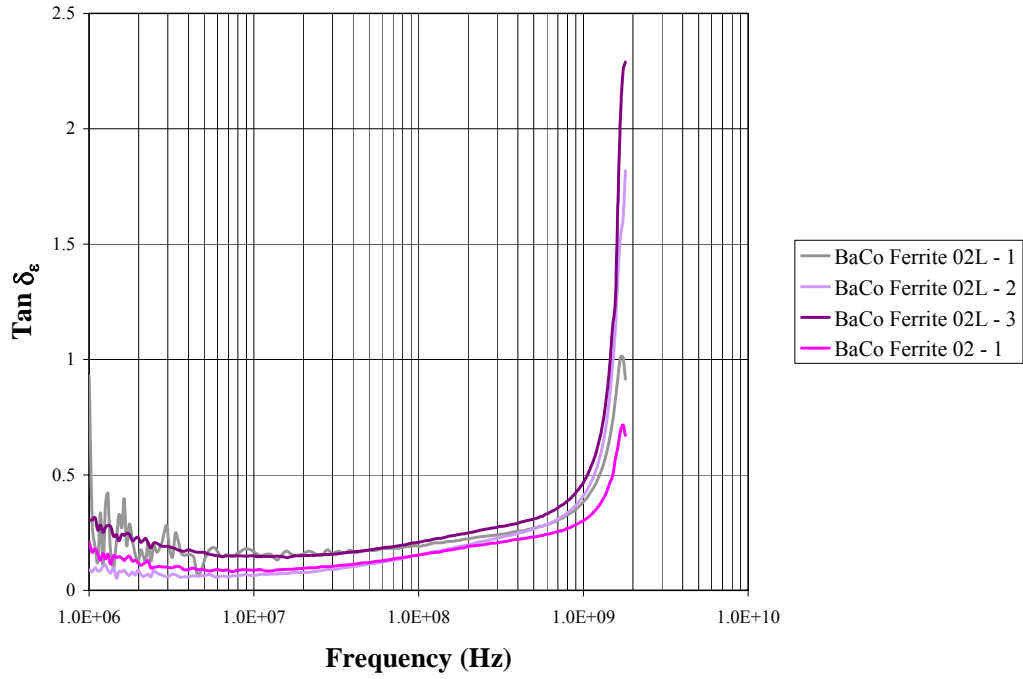


Figure 4.38: $\text{Tan } \delta_\epsilon$ versus frequency for composites made from BaCo Ferrite 02L and BaCo Ferrite 02

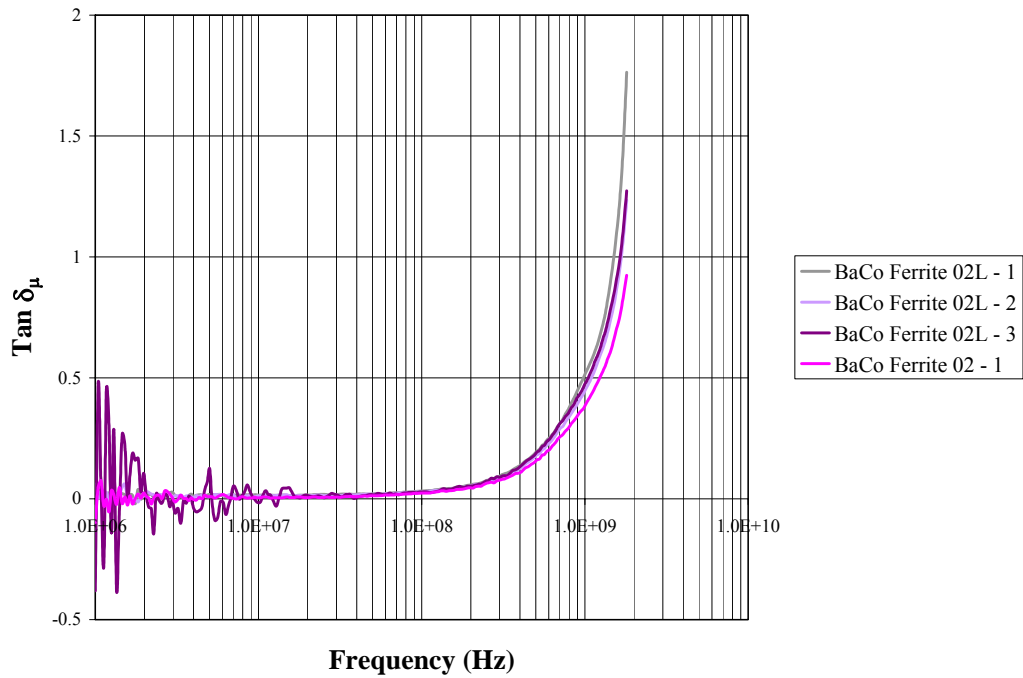


Figure 4.39: $\text{Tan } \delta_\mu$ versus frequency for composites made from BaCo Ferrite 02L and BaCo Ferrite 02

Table 4.1: Summary of Measurements for ϵ' , μ' , $\tan\delta_\epsilon$, and $\tan\delta_\mu$ at 400 MHz for Composites Made from BaCo Ferrite 02L and BaCo Ferrite 02

Measurement	ϵ'	μ'	$\tan\delta_\epsilon$	$\tan\delta_\mu$
BaCo Ferrite 02L - 1.1	17.2817	4.5287	0.2699	0.1357
BaCo Ferrite 02L - 1.2	17.3918	4.5360	0.2475	0.1377
BaCo Ferrite 02L - 1.3	17.6716	4.5315	0.2674	0.1388
BaCo Ferrite 02L - 1.4	17.4887	4.5362	0.2549	0.1383
BaCo Ferrite 02L - 1.5	16.5108	4.5240	0.2400	0.1372
BaCo Ferrite 02L - 2.1	18.5112	4.1793	0.2614	0.1238
BaCo Ferrite 02L - 2.2	18.5395	4.1414	0.2618	0.1250
BaCo Ferrite 02L - 2.3	17.7759	4.1743	0.2460	0.1244
BaCo Ferrite 02L - 2.4	15.1054	4.1831	0.2159	0.1271
BaCo Ferrite 02L - 2.5	18.2405	4.1758	0.2493	0.1265
BaCo Ferrite 02L - 3.1	18.8692	4.3262	0.2969	0.1324
BaCo Ferrite 02L - 3.2	18.8015	4.3243	0.2964	0.1334
BaCo Ferrite 02L - 3.3	18.1921	4.3080	0.2910	0.1336
BaCo Ferrite 02L - 3.4	17.4957	4.3154	0.2774	0.1318
BaCo Ferrite 02L - 3.5	18.5112	4.2886	0.2931	0.1328
BaCo Ferrite 02 - 1.1	13.9403	3.3223	0.2313	0.1081
BaCo Ferrite 02 - 1.2	11.7236	3.3286	0.1985	0.1100
BaCo Ferrite 02 - 1.3	13.6718	3.3190	0.2276	0.1080
BaCo Ferrite 02 - 1.4	14.2777	3.3180	0.2360	0.1083
BaCo Ferrite 02 - 1.5	13.5262	3.3232	0.2111	0.1084

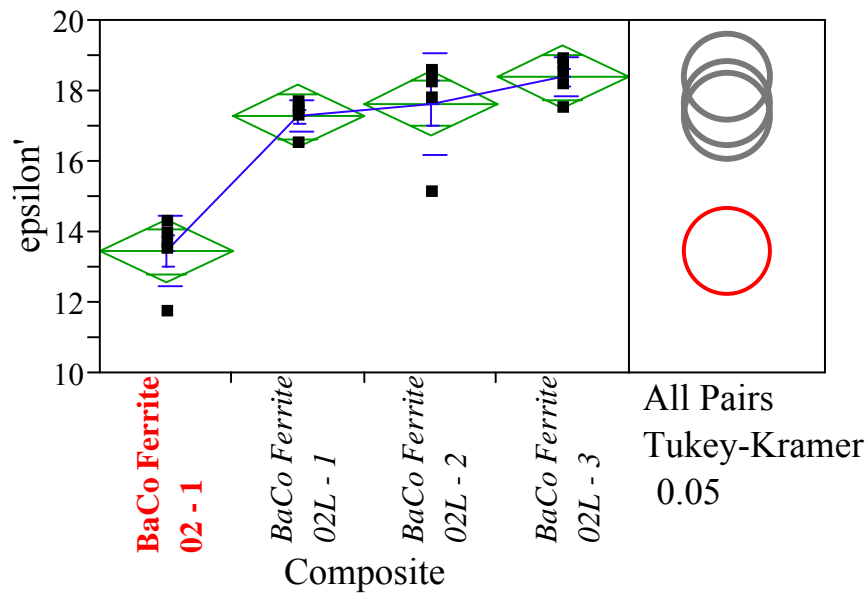


Figure 4.40: Statistical analysis of ϵ'' at 400 MHz for composites made from BaCo Ferrite 02L and BaCo Ferrite 02. Red circle represents group being compared and gray circles represent groups that are significantly different by Tukey-Kramer test at the 95% confidence level.

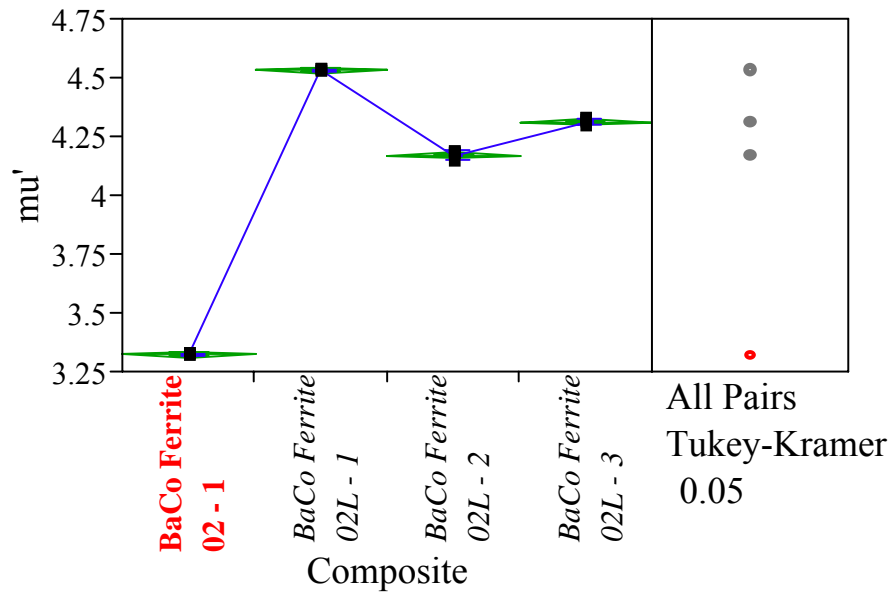


Figure 4.41: Statistical analysis of μ' at 400 MHz for composites made from BaCo Ferrite 02L and BaCo Ferrite 02. Red circle represents group being compared and gray circles represent groups that are significantly different by Tukey-Kramer test at the 95% confidence level.

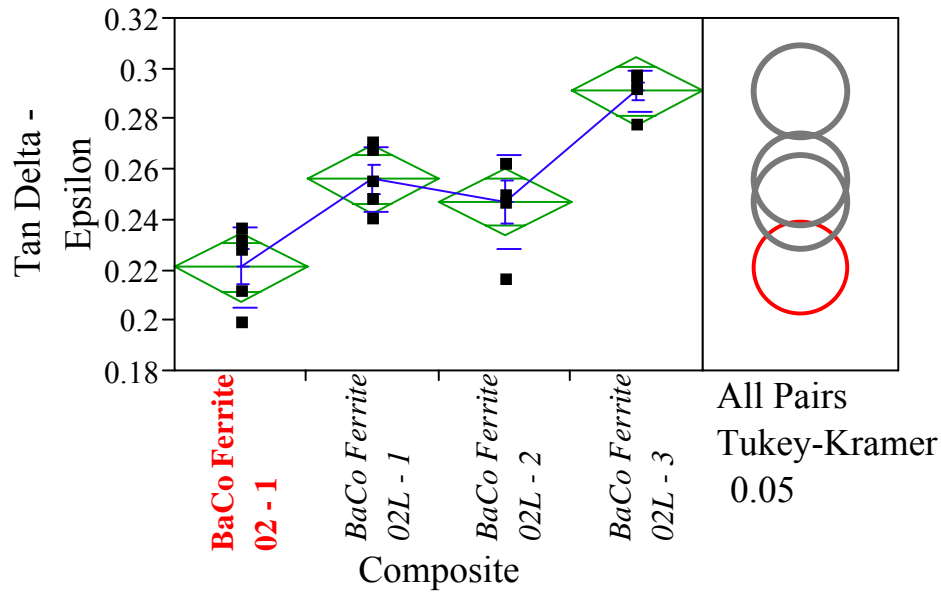


Figure 4.42: Statistical analysis of $\tan \delta_\epsilon$ at 400 MHz for composites made from BaCo Ferrite 02L and BaCo Ferrite 02. Red circle represents group being compared and gray circles represent groups that are significantly different by Tukey-Kramer test at the 95% confidence level.

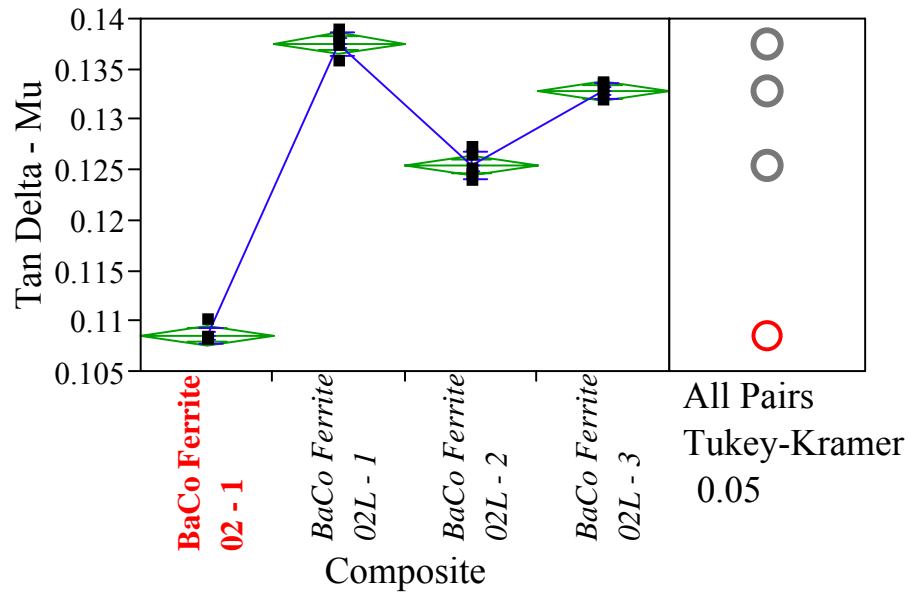


Figure 4.43: Statistical analysis of $\tan \delta_\mu$ at 400 MHz for composites made from BaCo Ferrite 02L and BaCo Ferrite 02. Red circle represents group being compared and gray circles represent groups that are significantly different by Tukey-Kramer test at the 95% confidence level.

Table 4.2: Summary of P-Values for Nonparametric Tests to Test Differences in ϵ' at 400 MHz for Two Groups of Particle Size Distributions. P-values less than 0.05 indicate significant differences between the compared groups at the 95% confidence level.

Particle Size Distribution	Composite	Wilcoxon / Kruskal-Wallis Tests		Median Tests		Van der Waerden Tests	
		Normal	ChiSquare	Normal	ChiSquare	Normal	ChiSquare
45-150 μm	BaCo Ferrite 01 - 1	0.0012	0.0011	0.0118	0.0118	0.0011	0.0011
45-250 μm	BaCo Ferrite 02L - 1						
	BaCo Ferrite 02L - 2						
	BaCo Ferrite 02L - 3						

Table 4.3: Summary of P-Values for Nonparametric Tests to Test Differences in μ' at 400 MHz for Two Groups of Particle Size Distributions. P-values less than 0.05 indicate significant differences between the compared groups at the 95% confidence level.

Particle Size Distribution	Composite	Wilcoxon / Kruskal-Wallis Tests		Median Tests		Van der Waerden Tests	
		Normal	ChiSquare	Normal	ChiSquare	Normal	ChiSquare
45-150 μm	BaCo Ferrite 01 - 1	0.0012	0.0011	0.0118	0.0118	0.0011	0.0011
45-250 μm	BaCo Ferrite 02L - 1						
	BaCo Ferrite 02L - 2						
	BaCo Ferrite 02L - 3						

Table 4.4: Summary of P-Values for Nonparametric Tests to Test Differences in $\tan\delta_e$ at 400 MHz for Two Groups of Particle Size Distributions. P-values less than 0.05 indicate significant differences between the compared groups at the 95% confidence level.

Particle Size Distribution	Composite	Wilcoxon / Kruskal-Wallis Tests		Median Tests		Van der Waerden Tests	
		Normal	ChiSquare	Normal	ChiSquare	Normal	ChiSquare
45-150 μm	BaCo Ferrite 01 - 1	0.0030	0.0026	0.0118	0.0118	0.0029	0.0029
45-250 μm	BaCo Ferrite 02L - 1						
	BaCo Ferrite 02L - 2						
	BaCo Ferrite 02L - 3						

Table 4.5: Summary of P-Values for Nonparametric Tests to Test Differences in $\text{Tan}\delta_{\mu}$ at 400 MHz for Two Groups of Particle Size Distributions. P-values less than 0.05 indicate significant differences between the compared groups at the 95% confidence level.

Particle Size Distribution	Composite	Wilcoxon / Kruskal-Wallis Tests		Median Tests		Van der Waerden Tests	
		Normal	ChiSquare	Normal	ChiSquare	Normal	ChiSquare
45-150 μm	BaCo Ferrite 01 - 1	0.0012	0.0011	0.0118	0.0118	0.0011	0.0011
45-250 μm	BaCo Ferrite 02L - 1						
	BaCo Ferrite 02L - 2						
	BaCo Ferrite 02L - 3						

Discussion

One of the most notable observations was the similar ϵ^* behavior the composites showed when compared to the ϵ^* behavior of the ferrites from which they were made. The comparison was made by visually inspecting the ϵ^* behavior of the composites in Figures 4.9, 4.10, and 4.11 and the ϵ^* behavior of the pressed ferrite powder in Figures 3.15, 3.16, and 3.17. Even the occurrence of the permittivity relaxation peak observed for the composite and pressed powder made from the BaCo Ferrite 02L occurred at nearly the same frequencies, which were 1.503 GHz for the composite and 1.401 GHz for the pressed ferrite powder. The ϵ^* behavior the composites was also inspected for considering their application as the substrate to an antenna. For their application, the favored behavior is constant ϵ^* properties with frequency, extending to the targeted operating frequency, and low loss quantified by ϵ'' and $\tan\delta_\epsilon$. The ϵ^* behavior for the BaCo Ferrite 02 and BaCo Ferrite 02L composites showed ϵ' not constant with frequency and also substantially higher loss quantified as ϵ'' and $\tan\delta_\epsilon$, making these composites less favorable for the antenna substrate application.

The μ^* behavior for the composites was measured and considered for application as the substrate to an antenna. By inspecting the μ^* behavior as a function of frequency, the frequency limit at which the material is applicable for designs can be determined. In Figures 4.12, 4.13, and 4.14, the μ^* properties showed dependence on frequency for the composite made from NiZn ferrite beginning at about 20 MHz and composites made from BaCo ferrite beginning at about 200 MHz. For their application, the favored behavior is constant μ^* properties with frequency, extending to the targeted operating frequency, and low loss quantified by μ'' and $\tan\delta_\mu$. Given the targeted operating frequency in the lower UHF

spectrum (~300-500 MHz), the composite made from the NiZn ferrite does not appear to be a reasonable candidate for the antenna application, whereas the composites made from the BaCo ferrite continue to be possible candidates. Upon closer inspection of the μ^* properties, a notable observation of the composites made from BaCo ferrite was that, even with normalized $\tan\delta_\mu$ values, both the BaCo Ferrite 02 and BaCo Ferrite 02L composite provided proportionally higher magnetic loss compared to the BaCo Ferrite 01 and BaCo Ferrite 04 composites. This result is attributable to the presence of M- and Y-phase included as impurities in the targeted Z-phase for the BaCo Ferrite 02 and BaCo Ferrite 02L batches, which was determined and noted in the previous chapter. With this observation of magnetic loss and continuing by process of elimination, the remaining candidates for the antenna application were the BaCo Ferrite 01 and BaCo Ferrite 04 composites.

Sources of variation in the measurements as well as in the formulation of composites were investigated. The measurements provided information on repeatability of the measurement systems and multiple formulation of the composites provided information on reproducibility of the composite formulation process. For the repeatability of the measurement system, the amount of variation as well as occurrences of two measurements appearing different than the others substantiated the need to report an average value of measurements for any sample. This work reports an average of five measurements for all samples. For the reproducibility of the composite formulation process, both the values and the behavior, or shape, of the ϵ^* and μ^* measurements were considered. By visual inspection of the average ϵ' and μ' values for the composites at 100 MHz, the values of ϵ' were observed to vary as much as 10% and more, and the values of μ' were observed to vary as much as about 10%. Due to the small values measured for $\tan\delta_\epsilon$ and $\tan\delta_\mu$, the variation at

100 MHz was calculated and found to be about higher. In particular, the lower loss BaCo Ferrite 04 composite has values of $\tan\delta_\epsilon$ and $\tan\delta_\mu$ that approach the limits of the instrument's capability to measure, making the variation high for the measured $\tan\delta_\epsilon$ and $\tan\delta_\mu$ values. With regard to the behavior, or shape, of the ϵ^* and μ^* measurements, the behavior of the ϵ^* and μ^* measurements as a function of frequency was found to be repeatability in the different measurements and reproducible in the different formulations for the types of composites investigated. As previously discussed for identifying possible material candidates for antenna applications, the behavior of both the ϵ^* and μ^* measurements as a function of frequency is critical to ensuring efficient and successful antenna designs.

The effect of treating ferrite particles with silane in the formulation process was also investigated. For this work, any effect of the silane was not detectable for the CTE, E^* , ϵ^* , and μ^* . For CTE and E^* , this result may be attributable to the large loading volume of 40 vol% ferrite. As previously observed, both the behavior and relative values of the ϵ^* properties for the composite largely follows the ferrite from which the composite was made. Even if the silane did have an effect, the behavior and values of ϵ^* and μ^* is likely largely dominated by the bulk properties of the ferrite filler as opposed to the filler-matrix interfaces.

Finally, the effect of ferrite particle size distribution in the composites was also investigated. The effect of the particle size distributions 45-150 μm and 45-250 μm was statistically tested and found to affect the ϵ^* and μ^* properties, specifically, increase ϵ' , μ' , $\tan\delta_\epsilon$, and $\tan\delta_\mu$ for the particle size distribution containing larger particles, at the 95% confidence level. It is likely that the larger particle sizes preserved a larger proportion of domains, providing higher values of μ' . These results support the previously stated approach

for this work, which is to use particle sizes that are sufficiently large in order to not disrupt the magnetic domains, therefore avoiding undesirable hysteresis loss and preserving μ_r values.

Conclusions

For the investigations performed in this work, it appears that the composite properties are largely dominated by the bulk properties of the ferrite filler. In particular, the ϵ^* properties measured for the composites closely mimic those for the ferrite from which they are made. Additionally, any effect due to treating the ferrite filler with silane in the composite formulation process was not detectable in this work, which further supports that the ϵ^* and μ^* properties of the composites were dominated more by the bulk properties of the ferrite filler compared to the filler-matrix interface. The effect of the ferrite particle size distributions of 45-150 μm and 45-250 μm were statistically compared, and it was found that the 45-250 μm particle size distribution gave larger values of ϵ' , μ' , $\tan\delta_\epsilon$, and $\tan\delta_\mu$ than the 45-150 μm particle size distribution at the 95% confidence level.

To continue onto the antenna application study, candidate materials for the antenna application in the targeted lower UHF spectrum ($\sim 300\text{-}500$ MHz) were identified to be the BaCo Ferrite 01 and BaCo Ferrite 04 composites. Also important for the antenna application study is that about 10% variation for the constant ϵ' and μ' values was determined in the composite formulation process.

CHAPTER V: ANTENNA EM SIMULATION AND EVALUATION

Introduction

The purpose of this chapter is to investigate the antenna performance and miniaturization capability attributable to the developed flexible magnetic composite and feasibility of applying the developed material to the lower UHF spectrum (~300-500 MHz). This investigation was carried out by designing patch antenna structures on both pure silicone and the developed magnetic composite and then comparing their performance. Additionally, the effects of material property variation on antenna performance were also studied.

Materials and Characterization

Material Formulation

Pure silicone and the developed magnetic composite were both used as substrates for an antenna structure, in order to compare antenna performance and determine capability for miniaturization. The developed magnetic composite was comprised of ferrite particles from the BaCo Ferrite 04 batch in a matrix of Dow Corning Sylgard 184 silicone. As described in Table 3.7, the BaCo Ferrite batch had particle size distribution of 45-150 μm . The magnetic composite was formulated by mixing 40 vol% ferrite particles in the uncured silicone, to form a wet powder.

Substrate Preparation

To fabricate the substrate, the wet powder was transferred to a pre-made flat mold, constructed of a 1 oz Cu foil sheet adhered with pure silicone to a bare 12" X 18" FR-4 laminate panel with a cut out in shape of the targeted substrate dimensions. Another 1 oz Cu foil sheet was then placed on top and more pure silicone was applied to the panel edges for

adhesion. The final panel was then placed in a printed circuit board press and processed at 121°C for 80 minutes. The silicone substrate was fabricated using the identical steps with the exception of using pure uncured silicone in the pre-made flat mold. Once the substrates were fabricated, the antenna structure was then made by standard double-sided printed circuit board processing techniques.

Impedance Analysis

The material properties of the resulting substrates were obtained to investigate applicability to the targeted operating frequency, that is, in the lower UHF band (~300-500 MHz) and determine inputs for antenna design via electromagnetic (EM) simulation. The materials were measured using an HP4291A impedance analyzer to obtain ϵ^* and μ^* (real and imaginary parts) with material fixtures 16453A for ϵ^* and 16454A for μ^* over the frequency range of 1 MHz to 1.8 GHz. There were 5 measurements taken for each relative permittivity (ϵ_r), relative permeability (μ_r), dielectric loss tangent ($\tan\delta_\epsilon$), and magnetic loss tangent ($\tan\delta_\mu$) to ensure repeatability.

Applied Material Properties

Measuring the pure silicone substrate, it was determined that the constant manufacturer specified properties shown in Table 5.1 were reasonable to use over the targeted operating frequency. For the magnetic composite, the properties ϵ_r , μ_r , $\tan\delta_\epsilon$ and $\tan\delta_\mu$ as a function of frequency were applied due their variation over the targeted operating frequency range, particularly near the upper limit of their applicability at ~400-500 MHz. The values of ϵ_r and $\tan\delta_\epsilon$ obtained in a single measurement are shown in Figure 5.1, and the values of μ_r and $\tan\delta_\mu$ obtained in single measurements are shown in Figure 5.2. The final material properties used were 11-point moving averages of the values shown in Figures 5.1 and 5.2 for removing

measurement artifacts and producing smoothed data, which is better handled by EM simulation packages.

Table 5.1: Material Properties for Pure Silicone

ϵ_r	2.65
$\tan\delta_\epsilon$	0.001
μ_r	1
$\tan\delta_\mu$	0

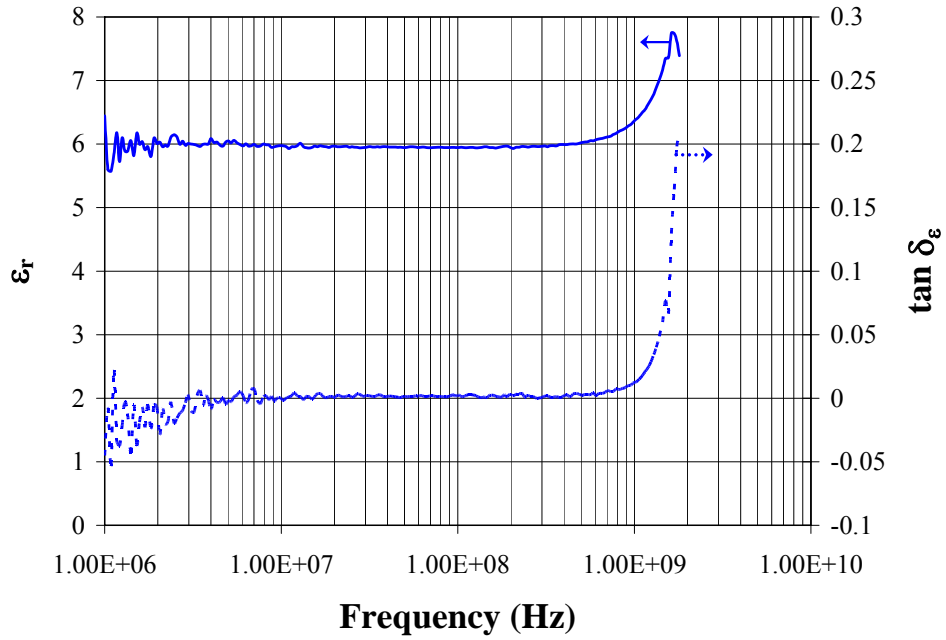


Figure 5.1: Values of ϵ_r and $\tan \delta_\epsilon$ obtained in a single measurement

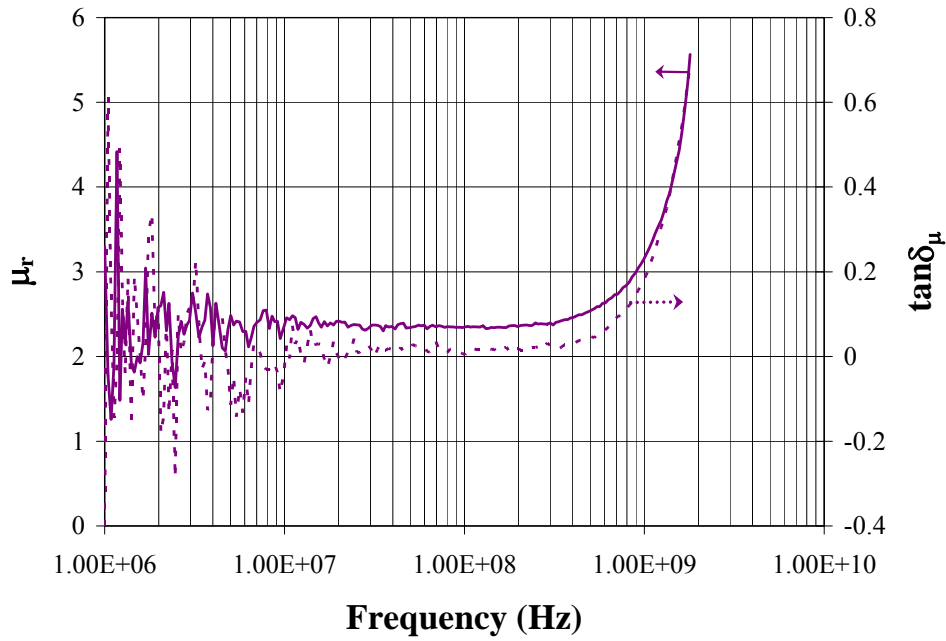


Figure 5.2: Values of μ_r and $\tan \delta_\mu$ obtained in a single measurement

Analytical Equipment and Methods

Figures of Merit

The performance figures of merit for the patch antennas were resonant frequency (f_r), return loss (RL), the -10dB bandwidth (BW), the two-dimensional (2-D) radiation patterns at $\phi = 0^\circ$ and 90° , maximum gain, and circuit Q as defined by (2.1). These figures of merit were obtained from the reflection coefficient (S_{11}) values measured by a network analyzer and the radiation patterns measured in an anechoic chamber.

Measurement Methodology

For the S_{11} values, the measurement was performed using a Wiltron 37217B Vector Network Analyzer across frequency range of 300-400 MHz. In this measurement, a quarter-wave choke was used to isolate the ground return current on the cable connected to the network analyzer. Figure 5.3 shows a picture of the measurement setup for obtaining S_{11} values.

For the 2-D radiation patterns, the measurement was conducted in an anechoic chamber. Gain was obtained using the gain substitution method, by which an adjustable dipole antenna (Scientific Atlanta, Model No. 15-350, Serial No. 264) with fixed 2.0 dBi gain was used as the reference. In this measurement, a quarter-wave choke was used to isolate the ground return current on the cable. Figure 5.4 shows pictures of the measurement setup for obtaining 2-D radiation pattern in the anechoic chamber, including antenna under test in vertical position, antenna under test in horizontal position, receiving antenna in vertical position, receiving antenna in horizontal position, view through anechoic chamber, in direction of antenna under test from receiving antenna end, and adjustable reference dipole antenna under test. The radiation pattern measurements convention for ϕ and θ is given in

Figure 5.5. The convention is that ϕ is rotated away from the x-axis and θ is rotated away from the z-axis. The 2-D radiation patterns and adjusted gain at $\phi = 0^\circ$ and 90° were obtained for the patch antenna on the magnetic composite as measured and simulated and the pure silicone as simulated.

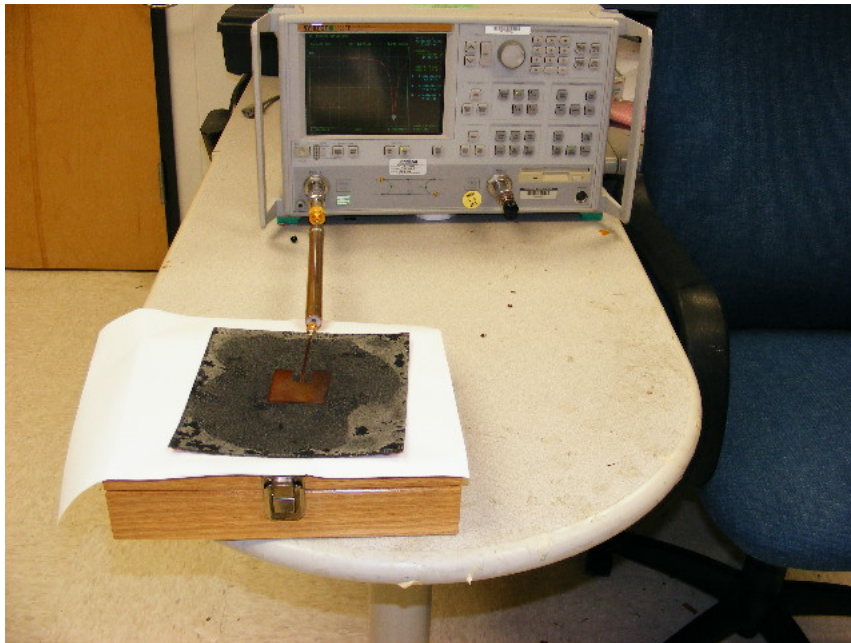


Figure 5.3: Picture of the measurement setup for obtaining S_{11} values

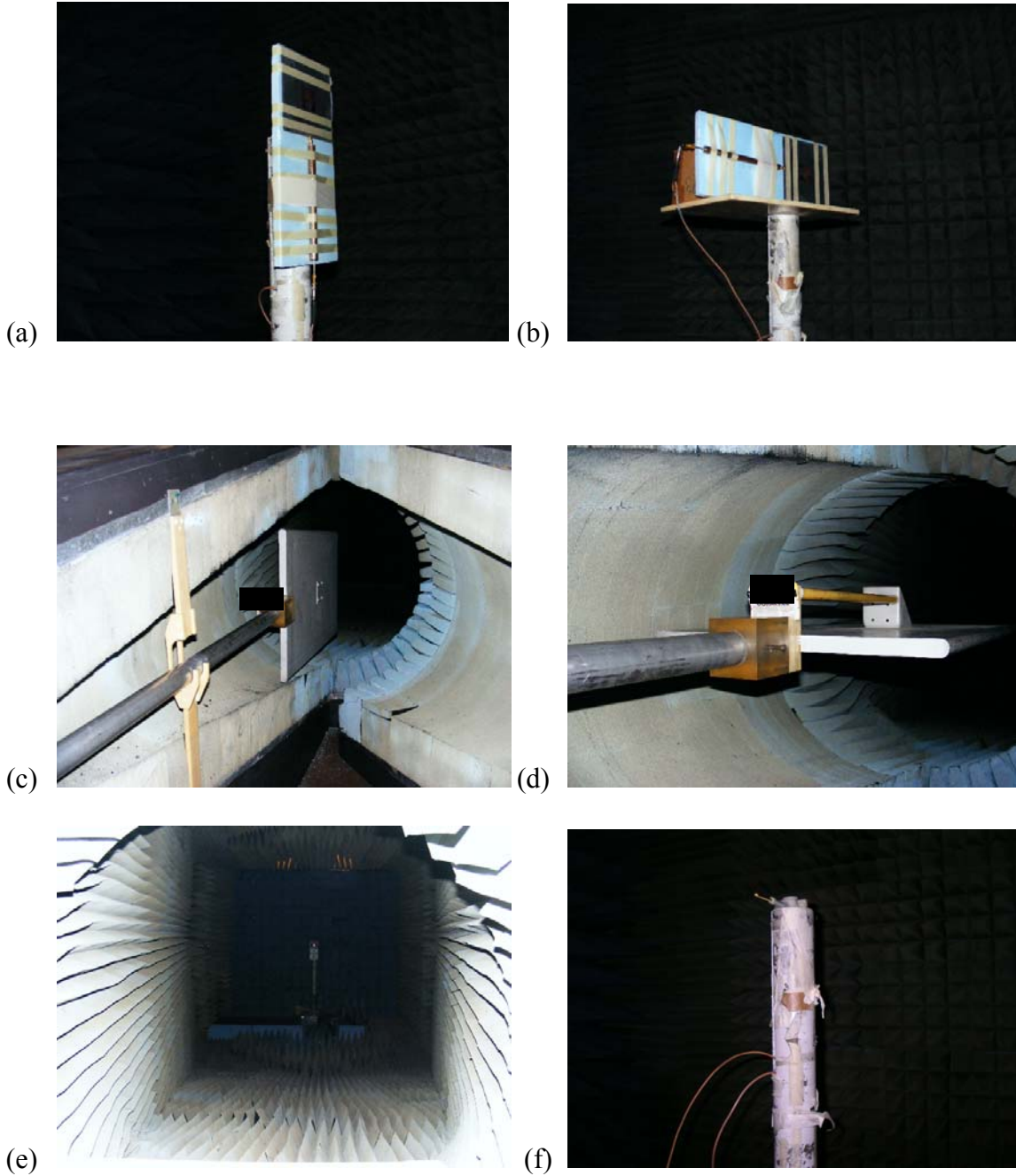


Figure 5.4: Pictures of measurement setup for obtaining 2-D radiation pattern in anechoic chamber. (a) Antenna under test in vertical position, (b) antenna under test in horizontal position, (c) receiving antenna in vertical position, (d) receiving antenna in horizontal position, (e) view through anechoic chamber, in direction of antenna under test from receiving antenna end, and (f) adjustable reference dipole antenna under test.

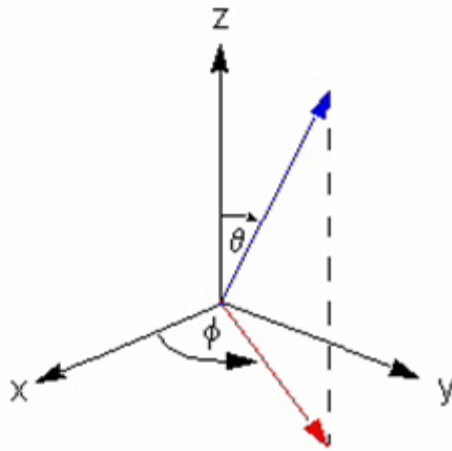


Figure 5.5: Radiation pattern measurement convention for ϕ and θ . ϕ is rotated away from the x-axis and θ is rotated away from the z-axis.

Antenna Structure and Design Methodology

Benchmark Antenna Structure

The analyzed structure was a quarter-wavelength microstrip patch antenna in the lower UHF band (~300-500 MHz). The approach was to apply the previously determined material properties ϵ_r , μ_r , $\tan\delta_\epsilon$ and $\tan\delta_\mu$ and assume several initial design rules for the comparison of the patch antennas built on the pure silicone versus the magnetic composite substrate. Table 5.2 shows the initial design rules for the targeted operating frequency, substrate thickness (h), and the ratio of patch size : ground size.

Table 5.2: Initial Design Rules for Patch Antennas

Operating Frequency	386 MHz
h (Substrate Thickness)	3.2 mm
Patch Size : Ground Size	0.27

Design Methodology

For designing the analyzed antenna structures, Ansoft HFSS version 11.0.1 simulation package, a full wave, finite element method (FEM) EM solver, was applied. The material properties ϵ_r , μ_r , $\tan\delta_\epsilon$ and $\tan\delta_\mu$ for the magnetic composite were input in the simulation as a function of frequency. The design methodology included first developing an isolated microstrip model on the substrate and determining microstrip width (w) that gave characteristic impedance (Z_0) of 50 Ω . Then, the patch size was adjusted to tune to the targeted operating frequency. Finally, the inset (d) was adjusted to minimize RL.

Final Antenna Designs

The patch antenna designs resulting from the EM simulations for the pure silicone and the magnetic composite substrate are shown in Figures 5.6 and 5.7, respectively. The patch antenna design on pure silicone substrate includes a microstrip feed to a 115.6 mm square patch over a 425 mm square ground and shorting of the patch to ground along the feed side. The patch antenna design on the magnetic composite substrate includes a microstrip feed to a 49 mm square patch over a 180 mm square ground and shorting of the patch to ground along the feed side. The patch on the magnetic composite is smaller (miniaturized) compared to the patch on pure silicone in order to achieve the targeted operating frequency of 386 MHz.

To fabricate the prototype antenna on the magnetic composite substrate, the design was panelized on the standard 305 x 457 x 1.6 mm panel for processing. Shown in Figure 5.8 is the layout of the prototype magnetic composite antenna, utilizing the mold design on the 305 x 457 x 1.6 mm FR-4 panel illustrated in Figure 4.5. The prototype antenna was fabricated over the 180 x 180 mm cavity, which contains the magnetic composite substrate. Standard double-sided printed circuit board (PCB) processing techniques were used to fabricate the prototype. The process started with the standard 305 x 457 x 1.6 mm panel that included trimmed edges and the 180 x 180 mm cavity containing the cured magnetic substrate. Then, the panel was drilled for alignment holes and vias having 0.508 mm diameter and 2.032 mm pitch along the feed side. Next, the panel was chemically cleaned. The panel was plated with electroless copper followed by electroplated copper, plated for 70 minutes at 45 amps per panel. The photolithography process was performed, including lamination of a negative photoresist, exposure, and development. The exposed copper was then etched followed by stripping the remaining photoresist. Then, the panel was rinsed and dried with hot air.

Finally, the panel was routed in order to remove the prototype antenna. The resulting prototype of the patch antenna design on the magnetic composite was built and is shown in Figure 5.9.

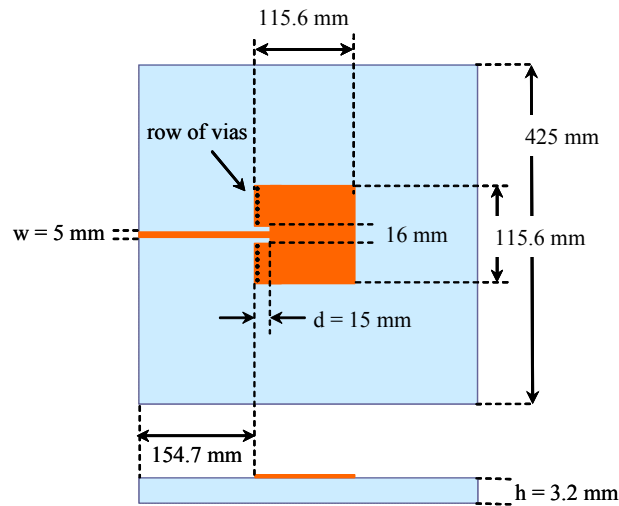


Figure 5.6: Dimensions of patch antenna design on pure silicone substrate (not drawn to scale)

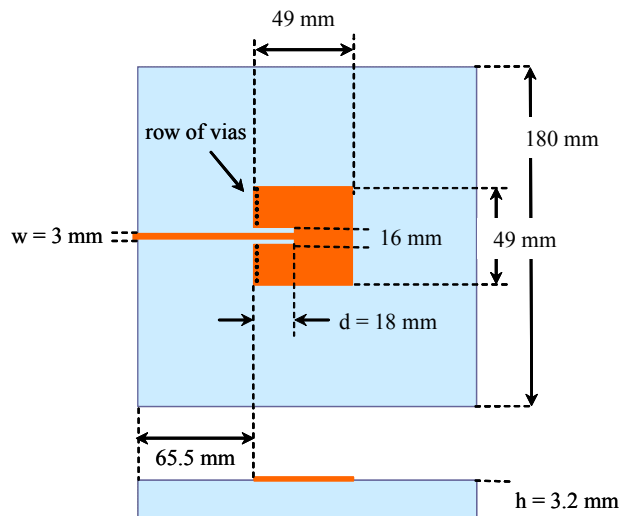


Figure 5.7: Dimensions of patch antenna design on magnetic composite substrate (not drawn to scale)

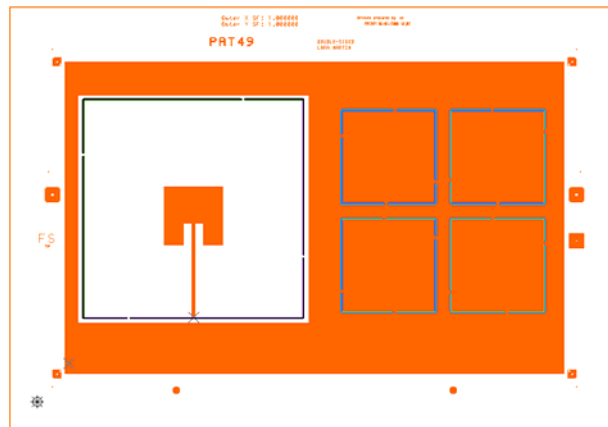


Figure 5.8: Layout of the prototype magnetic composite antenna, utilizing the mold design on the 305 x 457 x 1.6 mm FR-4 panel illustrated in Figure 4.5. The prototype antenna was fabricated over the 180 x 180 mm cavity, which contains the magnetic composite substrate.

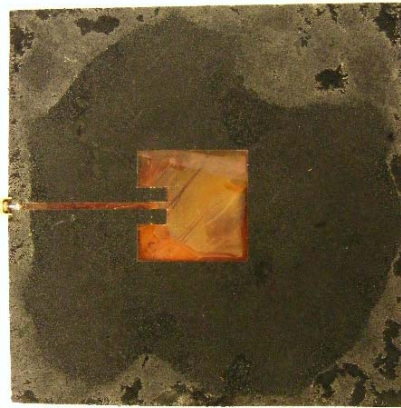


Figure 5.9: Photograph of prototype patch antenna on magnetic composite substrate

Results

Reflection Coefficients

The S_{11} values obtained for the patch antenna on the magnetic composite as measured and simulated and the pure silicone as simulated are shown in Figure 5.10.

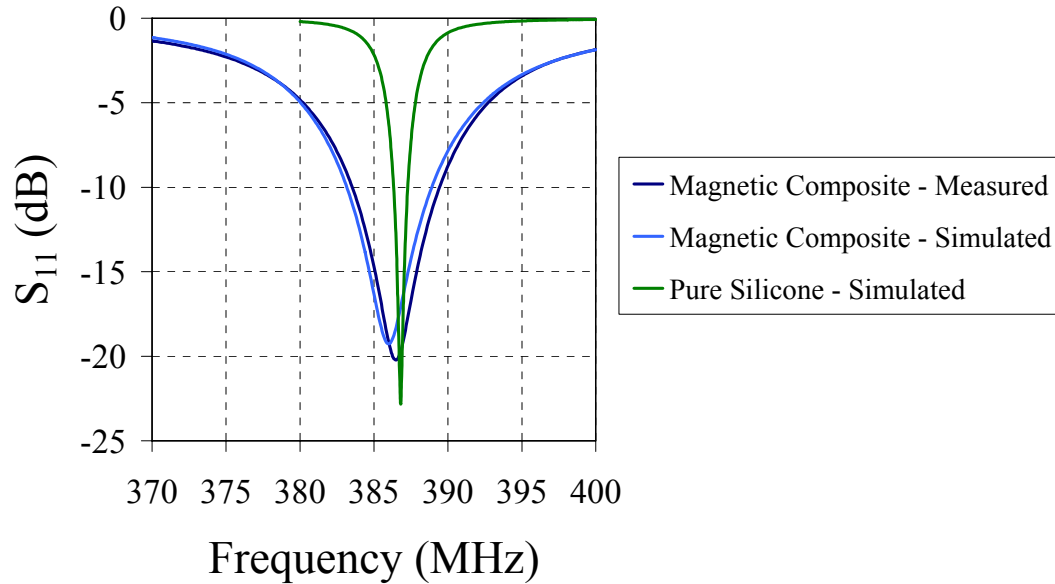


Figure 5.10: S_{11} versus frequency for patch antennas on magnetic composite as measured, magnetic composite as simulated, and pure silicone as simulated

Radiation Patterns

The 2-D radiation patterns and adjusted gain at $\phi = 0^\circ$ and 90° for the patch antenna on the pure silicone as simulated and the magnetic composite as measured and simulated are shown in Figures 5.11 and 5.12, respectively. The radiation patterns were taken at the f_r determined by the S_{11} values for each of the corresponding antenna designs.

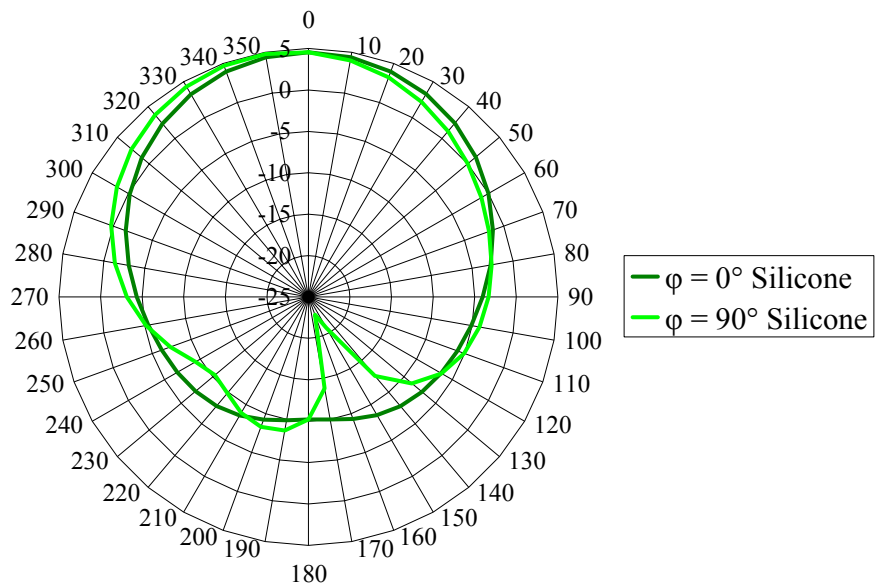


Figure 5.11: Radiation pattern and adjusted gain at $\phi = 0^\circ$ and 90° for patch antenna on silicone as simulated, taken at f_r

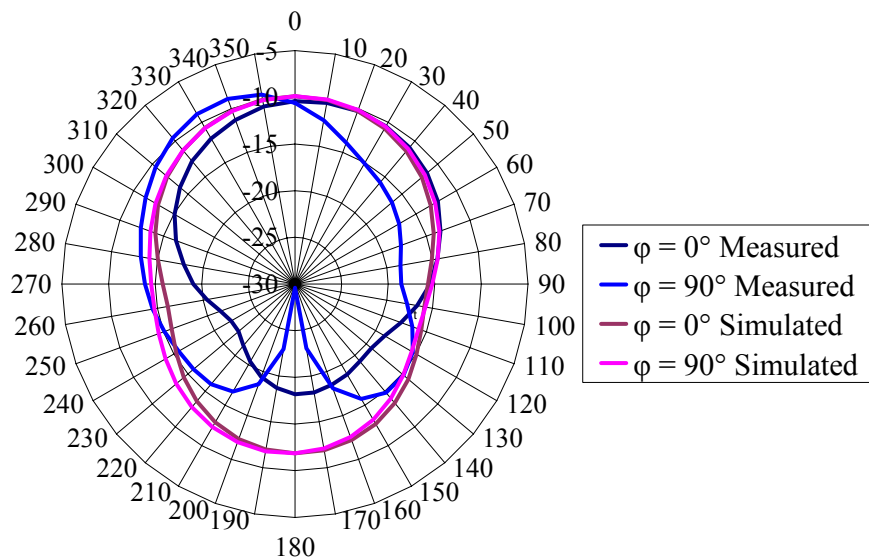


Figure 5.12: Radiation pattern and adjusted gain at $\phi = 0^\circ$ and 90° for patch antenna on magnetic composite as measured and simulated, taken at f_r

Summary of Figures of Merit

The antenna performance for the measured magnetic composite antenna, the simulated magnetic composite antenna, and the simulated pure silicone antenna was determined for the figures of merit f_r , RL, -10 dB BW, maximum gain, and circuit Q. The summary of antenna performance for all cases is shown in Table 5.3.

Table 5.3: Summary of Antenna Performance

Antenna	f_r (MHz)	RL (dB)	-10 dB BW (MHz)	Max Gain (dBi)	Circuit Q
Magnetic Composite – Measured	386.5	-20.2	5.90	-8.9	66
Magnetic Composite – Simulated	386.0	-19.3	5.74	-9.9	67
Pure Silicone – Simulated	386.8	-22.8	0.96	4.8	403

Effects of Material Variation on Antenna Performance

Statistical Methodology and Objectives

With demonstrated performance of the antenna by both simulation and prototype, the effects of material variation on antenna performance was investigated using a hybrid EM simulation and statistical tools methodology. To begin, the antenna figures of merit were defined as the experimental outputs, or the responses, and the material properties were defined as the experimental inputs, or factors.

The antenna figures of merit selected as the output variables were f_r , RL at 386 MHz, and Maximum Gain at 386 MHz. These figures of merit describe the capability of the antenna to operate at the targeted operating frequency of 386 MHz.

Based on the previous variation study of the material properties ϵ' , μ' , $\tan\delta_\epsilon$, and $\tan\delta_\mu$, the properties ϵ' and μ' were chosen as the factors. It was previously observed that ϵ' and μ' for the BaCo ferrite could vary for different batches and, from experience gained in the work, it was observed that ϵ' and μ' can significantly affect the antenna figures of merit.

Additionally, the higher purity Z-phase BaCo ferrite (that is, BaCo Ferrite 01 and BaCo Ferrite 04) showed variation of $\tan\delta_\epsilon$ and $\tan\delta_\mu$ values that were sufficiently low for successful operation of the antenna. Based on the previous variation study, reasonable values of the higher purity Z-phase BaCo ferrite for the ϵ' and μ' properties were chosen to be 6 and 3 at 386 MHz, respectively, as the nominal values. Additionally, variation of $\pm 1.0\%$ tolerance for ϵ' and μ' was assumed, because it was expected that even this relatively small variation may significantly affect the antenna figures of merit. Assuming $\pm 1.0\%$ tolerance for the ϵ' and μ' was a 3σ process, the value of σ was calculated to be 0.02 and 0.01 for ϵ' and μ' , respectively. A process that is 3σ capable yields 99.73% of the values within the $\pm 3\sigma$ limits, and 6σ capable yields 99.9999998% [77]. Based on these assumptions and the initial calculations for the values of σ , the 3σ process control limits and 6σ process control limits were calculated. A summary of the variation assumed for the material properties at 386 MHz is shown in Table 5.4.

Table 5.4: Variation Assumed for the Material Properties at 386 MHz. Assumed variation is based on a 3σ process capable of a $\pm 1.0\%$ tolerance for the material properties.

Material Property	Nominal	Tolerance	σ	3σ Process Control Limits	6σ Process Control Limits
ϵ'	6	$\pm 1\%$	0.02	(5.94, 6.06)	(5.88, 6.12)
μ'	3	$\pm 1\%$	0.01	(2.97, 3.03)	(2.94, 3.06)

To vary the values of ϵ' and μ' in the EM simulation, files that represented the typical behavior observed for ϵ' and μ' as a function of frequency were selected and modified by an offset. The offset was determined by the value required to give the targeted value of ϵ' or μ' at 386 MHz. This approach is reasonable given a major finding discussed in the previous chapter, in particular, that the behavior, or shape, of the ϵ^* and μ^* measurements as a function of frequency was found to be repeatability in the different measurements and reproducible in the different composite formulations. The modified files of ϵ' and μ' as a function of frequency were applied to the EM simulation.

Because the nominal values for ϵ' and μ' of 3 and 6 at 386 MHz were assumed, respectively, the previous antenna design on the magnetic composite, shown in Figure 5.7, was slightly modified to resonate at the target operating frequency of 386 MHz. The previous antenna design shown in Figure 5.7 was optimized for the ϵ^* and μ^* properties measured for the specific BaCo Ferrite 04 composite on which it was fabricated. For the variation study, the only change in the antenna design was the square patch size from 49 mm to 44.75 mm in order to accommodate the slight increase in the nominal material property

values. The design used for this variation study is shown in Figure 5.13, which can be compared to the previous design in Figure 5.7.

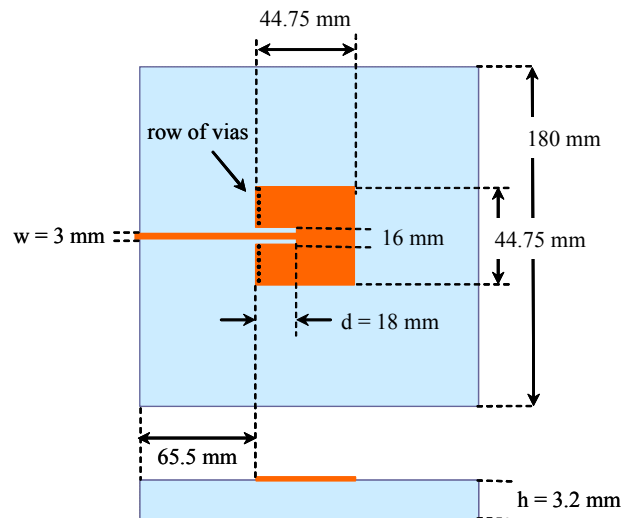


Figure 5.13: Dimensions of patch antenna design on magnetic composite substrate for the variation study (not drawn to scale)

The methodology used to develop the statistical models that describe antenna performance as functions of the material properties is presented in Figure 5.14. To perform the statistical analysis required to execute this methodology, JMP software was used [77]. The experimental design chosen for the first-order statistical model was a full factorial DOE with center points [78, 79]. Factorial designs are used in experiments involving several factors where the goal is the study of the joint effects of the factors on a response or responses [80, 81, 82, 83, 84, 85, 86, 87, 88, 89, 90, 91, 92, 93, 94, 95, 96, 97]. Prior knowledge of the analyzed system is required for choosing the factors and their studied

ranges. The 2^k factorial design is the simplest design type, with k factors at two levels each. The two levels, low and high, of the factors define the design space of the experiment. The 2^k experimental design provides the smallest number of runs for studying k factors. Center points are defined at the center of the design space and increase the capability for investigating the validity of the model, including curvature in the response, and account for variation inherent in obtaining the true values of both the factors and responses. Since the statistical models were based on deterministic simulations, the variation of the center points was based on an assumed capability for measuring the material properties. The center points were statistically simulated based on an assumed $\pm 0.1\%$ tolerance for a 3σ process of measuring ε' and μ' . This assumption is reasonable when compared to the assumed $\pm 1.0\%$ tolerance for the ε' and μ' properties shown in Table 5.4, which implies that inherent variation in obtaining true values can come from the measurement system and it comprises about 10% of the variation in the measured values. The center points were randomly generated assuming a mean equal to the exact center point value and the calculated standard deviations of 0.002 and 0.001 for ε' and μ' , respectively. If sufficient curvature occurs in the response, ultimate lack of fit may be determined for the first-order statistical model.

As further described by Figure 5.14, if ultimate lack of fit is determined for the models, the analysis is extended to develop second-order models. Developing second-order models requires addition of axial points for RSM, which can account for the curvature [79]. The second-order models can be reasonable approximations of the true functional relationship over relatively small ranges.

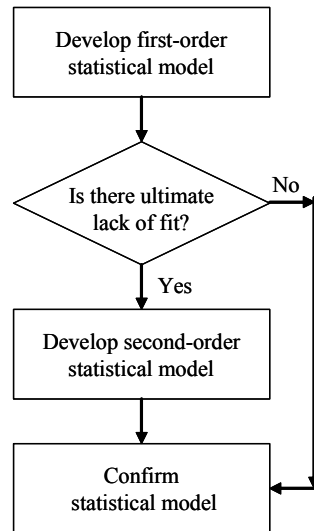


Figure 5.14: Methodology for developing statistical models

Once the statistical models were developed, the best models were identified based on values of statistical diagnostics for model fit and whether the models could be both validated and confirmed. Statistical diagnostics were used to assess model fit, and the models with best fit were chosen. To validate the models, the assumptions of independence of the data, normality of the residuals, and equal variance of the residuals were considered. Because the data were deterministically simulated, the assumption of independence was considered valid. The assumptions of normality and equal variance of the residuals were investigated for the models. Both assessment of model fit and model validation were done as part of the investigation for ultimate lack of fit. To confirm the models, a unique point within the design space was selected, and several runs with the same variation as that assumed for the center points were performed. The mean of the runs was compared to the 95% confidence interval for the mean predicted by the model. If the mean of the runs falls within the interval, the model is confirmed. When results show models to be similar in their fit, validation, and

confirmation, the simpler of the models was selected. Taking into account the combined results of model fit, validation, and confirmation, the best models were declared as the final statistical models. These final models approximate the actual system within the defined design space.

Using the final statistical models, Monte Carlo simulation was applied to investigate the effects of ε' and μ' on f_r , RL at 386 MHz, and Maximum Gain at 386 MHz. To perform the Monte Carlo simulation and analyses, Crystal Ball software was used [98]. A total of 20,000 trials were performed that assumed variation of ε' and μ' described by Table 5.4. After the 20,000 trials were generated, the variation of ε' and μ' was compared to the assumptions. Then, capability analysis was performed to determine whether f_r , RL at 386 MHz, and Maximum Gain at 386 MHz were capable of 6σ performance. Six Sigma capability is reached for processes that have both lower specification limit (LSL) and upper specification limit (USL) and achieve $C_p > 2.0$ and $C_{pk} > 1.5$, realizing no more than 3.4 parts per million opportunities and assuming long term process shift of ± 1.5 sigma shift. Six Sigma capability is reached for processes that have either LSL or USL and achieve $C_{pk} > 1.5$, realizing no more than 3.4 parts per million opportunities and assuming long term process shift of ± 1.5 sigma shift. C_{npk} is substituted for C_{pk} when the data is non-normal. All figures of merit f_r , RL at 386 MHz, and Maximum Gain at 386 MHz were statistically tested for normality. Finally, sensitivity analysis was performed to determine relative contributions of ε' and μ' to the variation in f_r , RL at 386 MHz, and Maximum Gain at 386 MHz.

Experiment

The original DOE design assumed $\pm 1.5\%$ ranges for material properties as the experimental design space. The DOE experimental design is described by Table 5.5. The

$\pm 1.5\%$ ranges were chosen to minimize probability of extrapolating beyond the design space that the statistical models describe, when the $\pm 1.0\%$ tolerances for the material properties shown in Table 5.4 were applied for the Monte Carlo simulations. Because curvature was found in at least one of the responses, axial points were added to the DOE, thereby producing an RSM experimental design. The RSM experimental runs and results for f_r , RL at 386 MHz, and Max Gain at 386 MHz are shown in Table 5.6.

For the confirmation of the statistical models, the unique point selected within the design space was nominal values for ϵ' and μ' equal to 6.080 and 3.040, respectively. A total of three confirmation runs were randomly generated with the same variation as that assumed for the center points. The RSM confirmation runs and results for f_r , RL at 386 MHz, and Max Gain at 386 MHz are shown in Table 5.7.

Additionally, to investigate the effect of dielectric loss and magnetic loss, a run for $\tan\delta_\epsilon$ and $\tan\delta_\mu$ both equal to zero was performed. This run was performed at the center point for the RSM, which was ϵ' and μ' equal to 6.000 and 3.000, respectively. For this run, f_r of 385.9 MHz and RL of only -0.8472 dB were determined. The poor RL was attributed to the change in Z_O , which was no longer equal to 50Ω and thereby caused reflection of the input power. Subsequently, the original design shown in Figure 5.13 was retuned by adjusting w and d equal to 1.0 mm and 1.4 mm, respectively, in order to achieve Z_O of 50Ω and minimize RL. Then, another run was performed with the retuned design assuming $\tan\delta_\epsilon$ and $\tan\delta_\mu$ both equal to zero. For the runs on the original design and retuned design, the results for f_r , RL at 386 MHz, and Max Gain at 386 MHz assuming $\tan\delta_\epsilon$ and $\tan\delta_\mu$ equal to zero are shown in Table 5.8.

Table 5.5: DOE Experimental Design. Design assumes $\pm 1.5\%$ ranges for material properties.

Material Property	Center Point	Low (-)	High (+)
ϵ'	6	5.91	6.09
μ'	3	2.955	2.955

Table 5.6: RSM Experimental Runs and Results for f_r , RL at 386 MHz, and Max Gain at 386 MHz

Pattern	ϵ'	μ'	f_r (MHz)	RL at 386 MHz (dB)	Max Gain at 386 MHz (dBi)
--	5.91	2.955	390.6	-7.8551	-8.9571
+-	5.91	3.045	386.3	-27.0005	-9.4336
+--	6.09	2.955	385.6	-23.6456	-9.7659
+++	6.09	3.045	380.6	-6.679	-9.5039
a0	5.8727	3	389.7	-9.5148	-8.1405
A0	6.1273	3	381.8	-8.6491	-9.4669
0a	6	2.9364	388.7	-11.8525	-10.122
0A	6	3.0636	382.4	-9.5865	-9.6017
0	6	3	385.9	-26.4044	-9.653
0	6.0003	3.0006	385.9	-27.06	-9.1001
0	5.9978	3.0021	385.6	-24.0879	-9.5071
0	6.0008	3.0014	385.8	-26.4812	-9.8287
0	5.9999	3.0003	385.6	-24.3267	-9.8179

Table 5.7: RSM Confirmation Runs and Results for f_r , RL at 386 MHz, and Max Gain at 386 MHz

Run	ϵ'	μ'	f_r (MHz)	RL at 386 MHz (dB)	Max Gain at 386 MHz (dBi)
1	6.085	3.040	381.7	-8.2432	-9.4179
2	6.080	3.040	380.6	-6.6990	-9.5726
3	6.079	3.048	380.6	-6.6923	-9.4994

Table 5.8: Results for f_r , RL at 386 MHz, and Max Gain at 386 MHz Assuming $\tan\delta_\epsilon$ and $\tan\delta_\mu$ Equal to Zero

Run	ϵ'	μ'	f_r (MHz)	RL at 386 MHz (dB)	Max Gain at 386 MHz (dBi)
1 Original Design	6.000	3.000	385.9	-0.8472	3.7140
2 Retuned Design	6.000	3.000	386.3	-7.9137	3.5817

Final Statistical Models

Resonant Frequency

The final statistical model for f_r is given by (5.1). The model includes the terms for the intercept and the main effects ε' and μ' . The plot of actual versus predicted values for the f_r model is shown in Figure 5.15. The plot shows high correlation of actual values and values predicted by the model, indicating a good model fit.

$$f_r = 385.73 - 2.734\left(\frac{\varepsilon' - 6}{0.09}\right) - 2.276\left(\frac{\mu' - 3}{0.045}\right) \quad (5.1)$$

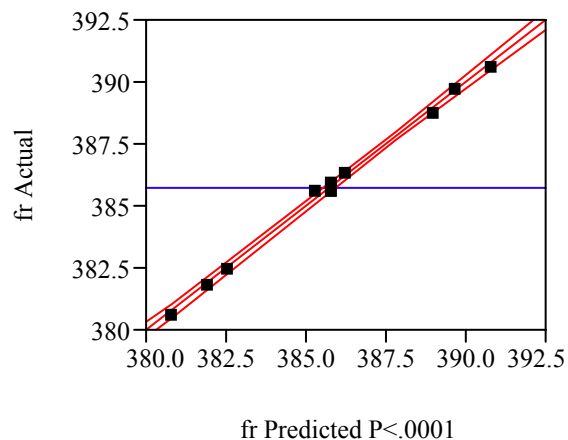


Figure 5.15: Plot of actual versus predicted values for the f_r model. The actual data from the experiment are shown in Table 5.6.

Statistical diagnostics for fit of the f_r model are shown in Table 5.9. The Rsquare is high, which corresponds to the high correlation of actual and predicted values observed in Figure 5.15. Additionally, the difference in Rsquare and Rsquare Adjusted is small, indicating that there are likely no extraneous terms in the model. The ANOVA p-value (Prob>F) is less

than 0.05, indicating the model is significant at the 95% confidence level. The Lack of Fit test p-value (Prob>F) is greater than 0.05, indicating that there is no significant lack of fit at the 95% confidence level.

Table 5.9: Statistical Diagnostics for Fit of the f_r Model. Good fit is indicated by maximizing Rsquare, minimizing difference between Rsquare and Rsquare adjusted, ANOVA Prob>F less than 0.05, and Lack of Fit Prob>F greater than 0.05.

Rsquare	0.996657
Rsquare Adjusted	0.995988
ANOVA Prob>F	<0.0001
Lack of Fit Prob>F	0.2974

The statistical significance of the parameter estimates for the f_r model is shown in Table 5.10. Because the p-values (Prob>t) are less than 0.05, all estimates are significant at 95% confidence level, indicating all terms in the model are significant in predicting the response.

Table 5.10: Statistical Significance of Parameter Estimates for the f_r Model. Because Prob>t values are less than 0.05, all estimates are significant at 95% confidence level.

Term	Parameter Estimate	Prob>t
Intercept	385.73	<0.0001
ε'	-2.734	<0.0001
μ'	-2.276	<0.0001

The assumptions of normality and equal variance of the residuals were investigated for the models by residual analysis. The histogram of residuals for the f_r model is shown in

Figure 5.16. The Goodness of Fit test p-value (Prob<W) was greater than 0.05, indicating the residuals fit the normal distribution at 95% confidence level. The plot of residuals versus predicted values for the f_r model is shown in Figure 5.17. By visual inspection, the residuals appear random, supporting equal variance of residuals for the model fit. Based on these results, the assumptions of normality and equal variance of the residuals were validated for the f_r model.

The confirmation results for the f_r model are shown in Table 5.11. Because the average of the confirmation runs falls within the 95% LCL and UCL for the confirmation, the f_r model is confirmed.

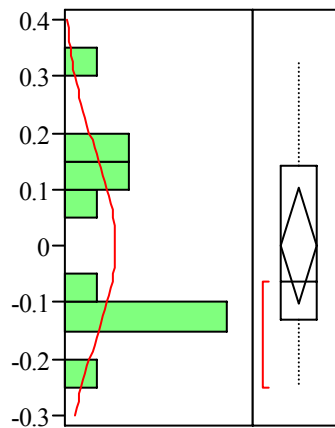


Figure 5.16: Histogram of residuals for the f_r model. Goodness of Fit Prob<W= 0.286. Because Prob<W value is greater than 0.05, the residuals fit the normal distribution at 95% confidence level.

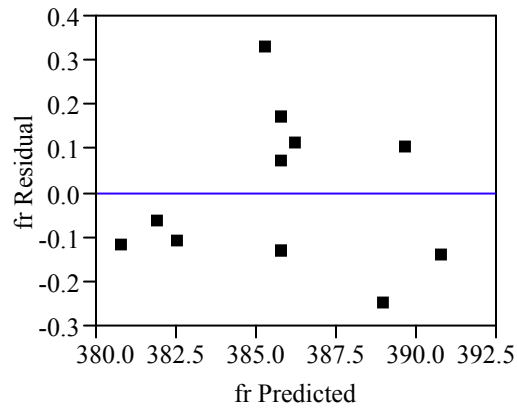


Figure 5.17: Plot of residuals versus predicted values for the f_r model. The residuals appear random, supporting equal variance of residuals for the model fit.

Table 5.11: Confirmation Results for the f_r Model. Because the average of the confirmation runs falls within the 95% LCL and UCL for the confirmation, the f_r model is confirmed. The raw data of the confirmation runs are shown in Table 5.7.

Average of Confirmation Runs	380.9667
95% LCL for Confirmation	380.9571
95% UCL for Confirmation	381.5974

Return Loss at 386 MHz

The final statistical model for RL at 386 MHz is given by (5.2). The model includes terms for the intercept, the main effects ε' and μ' , the interaction $\varepsilon'\mu'$, and second-order $\varepsilon' \varepsilon'$ and $\mu' \mu'$. The plot of actual versus predicted values for the RL at 386 MHz model is shown in Figure 5.18. The plot shows good correlation of actual values and values predicted by the model, indicating a good model fit.

$$\begin{aligned} \text{RL at 386 MHz} = & -25.672 + 0.7194\left(\frac{\varepsilon'-6}{0.09}\right) + 0.1282\left(\frac{\mu'-3}{0.045}\right) \\ & + 9.028\left(\frac{\varepsilon'-6}{0.09}\right)\left(\frac{\mu'-3}{0.045}\right) + 6.696\left(\frac{\varepsilon'-6}{0.09}\right)^2 + 5.878\left(\frac{\mu'-3}{0.045}\right)^2 \end{aligned} \quad (5.2)$$

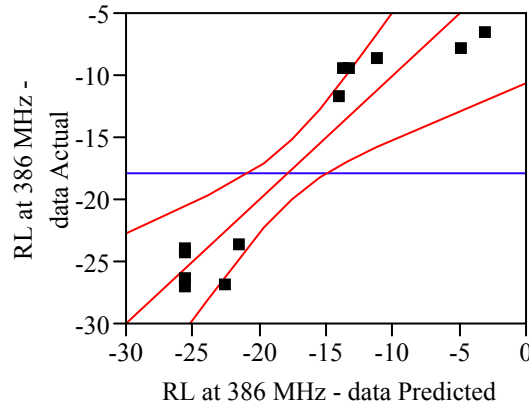


Figure 5.18: Plot of actual versus predicted values for the RL at 386 MHz model. The actual data from the experiment are shown in Table 5.6.

Statistical diagnostics for fit of the RL at 386 MHz model are shown in Table 5.12. The Rsquare is relatively high, which corresponds to the good correlation of actual and predicted values observed in Figure 5.18. Additionally, the difference in Rsquare and Rsquare

Adjusted is moderately small, indicating that extraneous terms may or may not be present in the model. The ANOVA p-value (Prob>F) is less than 0.05, indicating the model is significant at the 95% confidence level. The Lack of Fit test p-value (Prob>F) is less than 0.05, indicating that there is significant lack of fit at the 95% confidence level.

Table 5.12: Statistical Diagnostics for Fit of the RL at 386 MHz Model. Good fit is indicated by maximizing Rsquare, minimizing difference between Rsquare and Rsquare adjusted, ANOVA Prob>F less than 0.05, and Lack of Fit Prob>F greater than 0.05.

Rsquare	0.896897
Rsquare Adjusted	0.823253
ANOVA Prob>F	0.0024
Lack of Fit Prob>F	0.0114

The statistical significance of the parameter estimates for the RL at 386 MHz model is shown in Table 5.13. P-values (Prob>t) less than 0.05 indicate estimates that are significant at 95% confidence level. The estimates for the main effects ε' and μ' are not significant at the 95% confidence level but are retained in the model because other terms in the model include them.

Table 5.13: Statistical Significance of Parameter Estimates for the RL at 386 MHz Model. Prob>t values less than 0.05 indicate estimates that are significant at 95% confidence level. The main effects ε' and μ' are retained in the model because other terms in the model include them.

Term	Parameter Estimate	Prob>t
Intercept	-25.672	<0.0001
ε'	0.7194	0.5964
μ'	0.1282	0.9240
$\varepsilon' * \mu'$	9.028	0.0017
$\varepsilon' * \varepsilon'$	6.696	0.0019
$\mu' * \mu'$	5.878	0.0039

The assumptions of normality and equal variance of the residuals were investigated for the models by residual analysis. The histogram of residuals for the RL at 386 MHz model is shown in Figure 5.19. The Goodness of Fit test p-value (Prob<W) was greater than 0.05, indicating the residuals fit the normal distribution at 95% confidence level. The plot of residuals versus predicted values for the RL at 386 MHz model is shown in Figure 5.20. By visual inspection, the residuals appear somewhat random, supporting equal variance of residuals for the model fit. Based on these results, the assumptions of normality and equal variance of the residuals were validated for the RL at 386 MHz model.

The confirmation results for the RL at 386 MHz model are shown in Table 5.14. Because the average of the confirmation runs falls within the 95% LCL and UCL for the confirmation, the RL at 386 MHz model is confirmed.

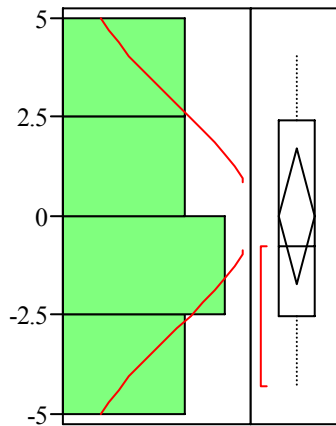


Figure 5.19: Histogram of residuals for the RL at 386 MHz model. Goodness of Fit Prob<W= 0.5708. Because Prob<W value is greater than 0.05, the residuals fit the normal distribution at 95% confidence level.

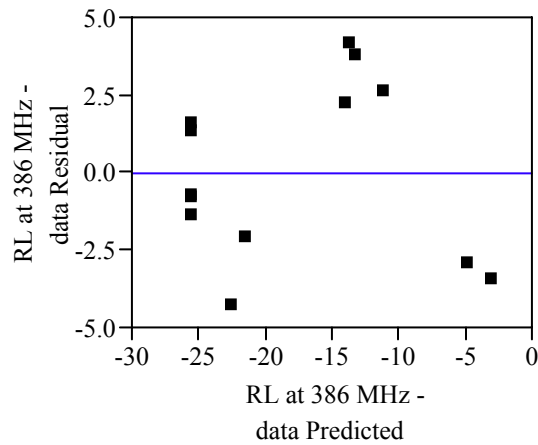


Figure 5.20: Plot of residuals versus predicted values for the RL at 386 MHz model. The residuals appear somewhat random, supporting equal variance of residuals for the model fit.

Table 5.14: Confirmation Results for the RL at 386 MHz Model. Because the average of the confirmation runs falls within the 95% LCL and UCL for the confirmation, the RL at 386 MHz model is confirmed. The raw data of the confirmation runs are shown in Table 5.7.

Average of Confirmation Runs	-7.2115
95% LCL for Confirmation	-15.4807
95% UCL for Confirmation	-0.2197

Maximum Gain at 386 MHz

The final statistical model for Maximum Gain at 386 MHz is given by (5.3). The model includes the terms for the intercept, the main effect ε' , and second-order $\varepsilon' \varepsilon'$. The plot of actual versus predicted values for the Maximum Gain at 386 MHz model is shown in Figure 5.21. The plot shows reasonable correlation of actual values and values predicted by the model, indicating reasonable model fit.

$$\text{Max Gain at 386 MHz} = -9.693 - 0.3444\left(\frac{\varepsilon' - 6}{0.09}\right) + 0.3892\left(\frac{\varepsilon' - 6}{0.09}\right)^2 \quad (5.3)$$

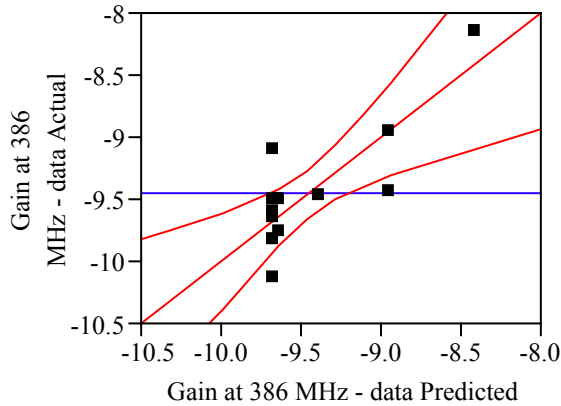


Figure 5.21: Plot of actual versus predicted values for the Maximum Gain at 386 MHz model. The actual data from the experiment are shown in Table 5.6.

Statistical diagnostics for fit of the Maximum Gain at 386 MHz model are shown in Table 5.15. The Rsquare is sufficiently high, which corresponds to the reasonable correlation of actual and predicted values observed in Figure 5.21. Additionally, the difference in Rsquare and Rsquare Adjusted is moderately small, indicating that extraneous terms may or

may not be present in the model. The ANOVA p-value (Prob>F) is less than 0.05, indicating the model is significant at the 95% confidence level. The Lack of Fit test p-value (Prob>F) is greater than 0.05, indicating that there is no significant lack of fit at the 95% confidence level.

Table 5.15: Statistical Diagnostics for Fit of the Maximum Gain at 386 MHz Model.

Good fit is indicated by maximizing Rsquare, minimizing difference between Rsquare and Rsquare adjusted, ANOVA Prob>F less than 0.05, and Lack of Fit Prob>F greater than 0.05.

Rsquare	0.677875
Rsquare Adjusted	0.613450
ANOVA Prob>F	0.0035
Lack of Fit Prob>F	0.3821

The statistical significance of the parameter estimates for the Maximum Gain at 386 MHz model is shown in Table 5.16. Because the p-values (Prob>t) are less than 0.05, all estimates are significant at 95% confidence level, indicating all terms in the model are significant in predicting the response.

Table 5.16: Statistical Significance of Parameter Estimates for the Maximum Gain at 386 MHz Model. Because Prob>t values are less than 0.05, all estimates are significant at 95% confidence level.

Term	Parameter Estimate	Prob>t
Intercept	-9.693	<0.0001
ε'	-0.3444	0.0105
$\varepsilon' * \varepsilon'$	0.3892	0.0075

The assumptions of normality and equal variance of the residuals were investigated for the models by residual analysis. The histogram of residuals for the Maximum Gain at 386 MHz model is shown in Figure 5.22. The Goodness of Fit test p-value (Prob<W) was greater than 0.05, indicating the residuals fit the normal distribution at 95% confidence level. The plot of residuals versus predicted values for the Maximum Gain at 386 MHz model is shown in Figure 5.23. By visual inspection, the residuals appear random, supporting equal variance of residuals for the model fit. Based on these results, the assumptions of normality and equal variance of the residuals were validated for the Maximum Gain at 386 MHz model.

The confirmation results for the Maximum Gain at 386 MHz model are shown in Table 5.17. Because the average of the confirmation runs falls within the 95% LCL and UCL for the confirmation, the Maximum Gain at 386 MHz model is confirmed.

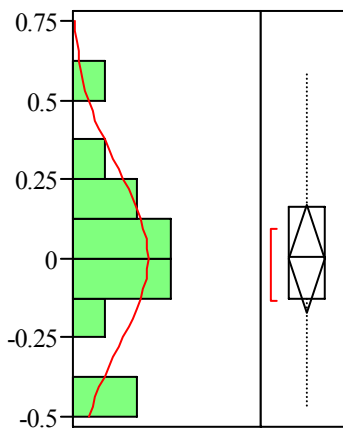


Figure 5.22: Histogram of residuals for the Maximum Gain at 386 MHz model. Goodness of Fit Prob<W= 0.8131. Because Prob<W value is greater than 0.05, the residuals fit the normal distribution at 95% confidence level.

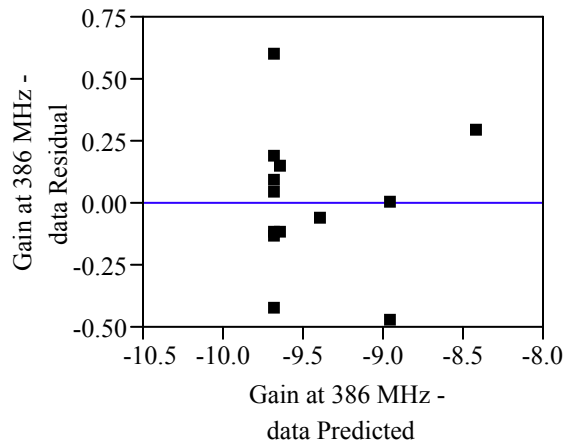


Figure 5.23: Plot of residuals versus predicted values for the Maximum Gain at 386 MHz model. The residuals appear random, supporting equal variance of residuals for the model fit.

Table 5.17: Confirmation Results for the Maximum Gain at 386 MHz Model. Because the average of the confirmation runs falls within the 95% LCL and UCL for the confirmation, the Maximum Gain at 386 MHz model is confirmed. The raw data of the confirmation runs are shown in Table 5.7.

Average of Confirmation Runs	-9.4966
95% LCL for Confirmation	-10.1865
95% UCL for Confirmation	-9.1971

Model Contour Plots

The contour plots of the final statistical models given by (5.1), (5.2), and (5.3) for f_r , RL at 386 MHz, and Maximum Gain at 386 MHz, respectively, are shown in Figure 5.24. The 3-dimensional relationships shown in this figure are plots of the statistical models for f_r , RL at 386 MHz, and Maximum Gain at 386 MHz. The relationship of each of the experimental responses f_r , RL at 386 MHz, and Maximum Gain at 386 MHz can be viewed as a function of

the experimental factors ε' and μ' . The relationship between f_r and the factors ε' and μ' is linear. The relationship between RL at 386 MHz and the factors ε' and μ' includes curvature. The relationship between Maximum Gain at 386 MHz and the factor ε' includes curvature.

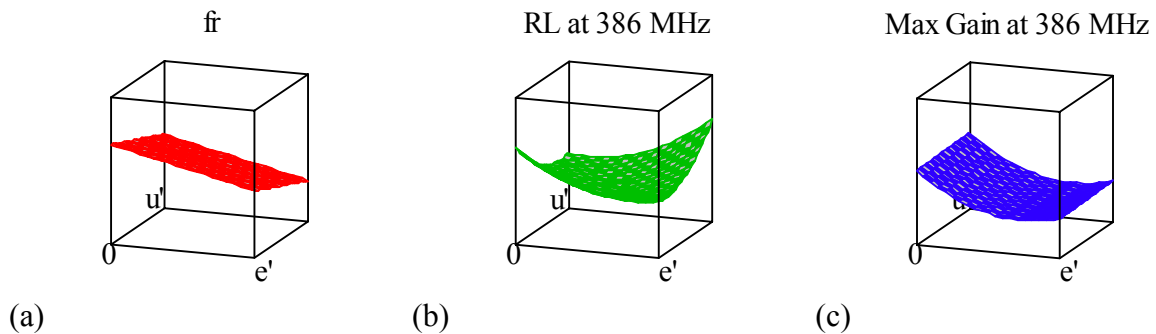


Figure 5.24: Contour plots of the final statistical models for (a) f_r , (b) RL at 386 MHz, and (c) Maximum Gain at 386 MHz

Simulated Antenna Performance Capability

The statistical models given by (5.1), (5.2), and (5.3), which are graphically shown in the Figure 5.24, were used in the application of Monte Carlo simulation to investigate the effects of ε' and μ' on f_r , RL at 386 MHz, and Maximum Gain at 386 MHz. For the Monte Carlo simulations, the variation assumed for ε' and μ' was the $\pm 1.0\%$ tolerances for the material properties shown in Table 5.4. To check the agreement of the 20,000 trials with the assumed variation, the trials for ε' and μ' were plotted in a histogram, and the mean and σ were calculated. The histograms of 20,000 trials for the inputs ε' and μ' that were generated in the Monte Carlo simulation are shown in Figure 5.25. The mean and σ were determined to be 6 and 0.02, respectively, for ε' , and 3 and 0.1, respectively, for μ' , which indicates agreement with the assumed variation.

The histograms of 20,000 trials for the outputs f_r , RL at 386 MHz, and Maximum Gain at 386 MHz are shown in Figure 5.26. Capability analysis was performed on these results to determine whether f_r , RL at 386 MHz, and Maximum Gain at 386 MHz were capable of 6σ performance. Because the optimization goal for f_r is to match the target of 386 MHz, the LSL and USL were assumed to be 384 and 388 MHz, which gave the target performance of 386 MHz centered in the limits. Because the optimization goal for RL at 386 MHz is to minimize, an USL of -10 dB was assumed. Because the optimization goal for Maximum Gain at 386 MHz is to maximize, a LSL of -10 dBi was assumed.

The results of f_r , RL at 386 MHz, and Maximum Gain at 386 MHz were statistically tested to determine if they were normally distributed. Normality test on f_r gave p-value of 0.925, which is greater than 0.05 and indicates that f_r is normally distributed at the 95% confidence level. The same normality test on RL at 386 MHz and Maximum Gain at 386 MHz gave p-values of 0.00, which is less than 0.05 and indicates that RL at 386 MHz and Maximum Gain at 386 MHz are both not normally distributed at the 95% confidence level.

Based on results of the normality tests, the appropriate capability metrics were selected and calculated to determine 6σ capability of f_r , RL at 386 MHz, and Maximum Gain at 386 MHz. For f_r , the capability metrics Cp and Cpk were calculated to be 0.84 and 0.73, respectively. Because Cp and Cpk were found to be less than 2.0 and 1.5, respectively, f_r was determined to not be 6σ capable for the assumed specification limits. For RL at 386 MHz and Maximum Gain at 386 MHz, the capability metric CnPk was calculated to be 3.74 and 3.88, respectively. Because the CnPk values were found to be greater than 1.5, RL at 386 MHz and Maximum Gain at 386 MHz were determined to be 6σ capable for the assumed

specification limits. The summary of process specification limits and capability metrics for f_r , RL at 386 MHz, and Maximum Gain at 386 MHz are shown in Table 5.18.

Sensitivity analysis was performed to determine relative contributions of ϵ' and μ' to the variation in f_r , RL at 386 MHz, and Maximum Gain at 386 MHz. The sensitivity charts showing contribution to variance of ϵ' and μ' for the outputs f_r , RL at 386 MHz, and Maximum Gain at 386 MHz are given in Figure 5.27. The inputs ϵ' and μ' contributed 59.1% and 40.9%, respectively, to the variation in f_r . The inputs ϵ' and μ' contributed 94.5% and 5.5%, respectively, to the variation in RL at 386 MHz. Only ϵ' contributed to the variation in Maximum Gain at 386 MHz, which was expected since the model developed for Maximum Gain at 386 MHz included dependence on ϵ' alone.

Finally, for investigation of the effect of dielectric loss and magnetic loss, the S_{11} values as a function of frequency for the patch antenna on magnetic composite assuming the original design with no loss, the original design with actual loss, and the retuned design with no loss were plotted for comparison. The original design is shown in Figure 5.13, and the retuned design was the same except w and d were equal to 1.0 mm and 1.4 mm, respectively. The plot of S_{11} versus frequency for patch antenna on magnetic composite assuming the original design with no loss ($\tan\delta_\epsilon$ and $\tan\delta_\mu$ equal to zero), the original design with actual loss ($\tan\delta_\epsilon$ and $\tan\delta_\mu$ equal to measured values), and the retuned design with no loss ($\tan\delta_\epsilon$ and $\tan\delta_\mu$ equal to zero) is shown in Figure 5.28. Additionally, the results in Table 5.8, the results for the center point ($\epsilon' = 6$ and $\mu' = 3$) in Table 5.6, and the result for Max Gain for pure silicone in Table 5.3 were considered. The dielectric and magnetic losses slightly affected f_r , with values of 385.9, 385.9, and 386.3 MHz for the patch antenna on magnetic composite assuming the original design with no loss, the original design with actual loss, and the

retuned design with no loss, respectively. The loss did affect RL at 386 MHz, as the values of -0.8472, -26.4044, and -7.9137 for the patch antenna on magnetic composite assuming the original design with no loss, the original design with actual loss, and the retuned design with no loss, respectively, were substantially different. This difference between the patch antenna on magnetic composite assuming the original design with no loss and the original design with actual loss was attributed to the change in Z_0 , which was no longer equal to 50Ω and thereby caused reflection of the input power. After adjusting w and d to 1.0 mm and 1.4 mm, respectively, for the retuned design, only limited RL at 386 MHz was achieved, which was attributed to the slight change in f_r and the comparatively narrower BW. The loss also affected Max Gain at 386 MHz, as observed when the values of 3.7, -9.7, 3.6, and 4.8 dBi were compared for the patch antenna on magnetic composite assuming the original design with no loss, the original design with actual loss, the retuned design with no loss, and the previous design on pure silicone shown in Figure 5.6, respectively. It was noted that the values of Max Gain at 386 MHz that were obtained from the simulation did not include effects of the microstrip impedance matching. Considering the differences in the values for Max Gain at 386 MHz, the decrease in the maximum gain for the patch antenna on the magnetic composite substrate compared to the pure silicone substrate may be attributable to both the addition of the dielectric and magnetic losses as well as the decrease in the patch size.

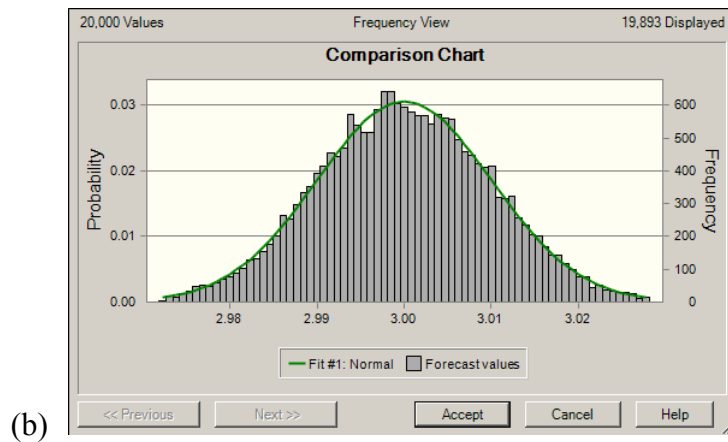
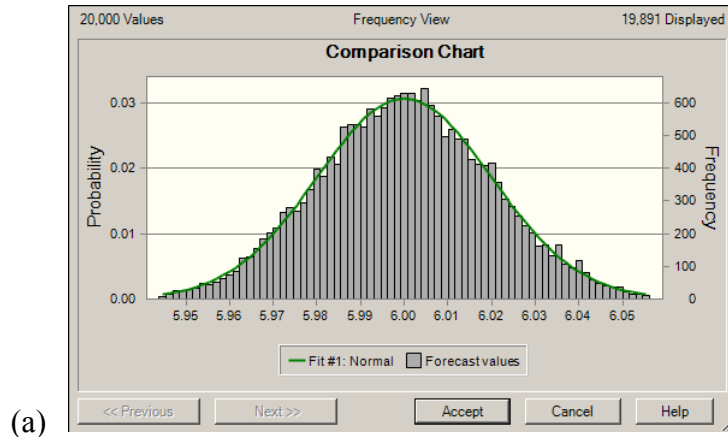


Figure 5.25: Histograms of 20,000 trials for the inputs (a) ε' and (b) μ' that were generated in the Monte Carlo simulation. (a) ε' mean = 6.00, $\sigma = 0.02$, and (b) μ' mean = 3.00, $\sigma = 0.01$.

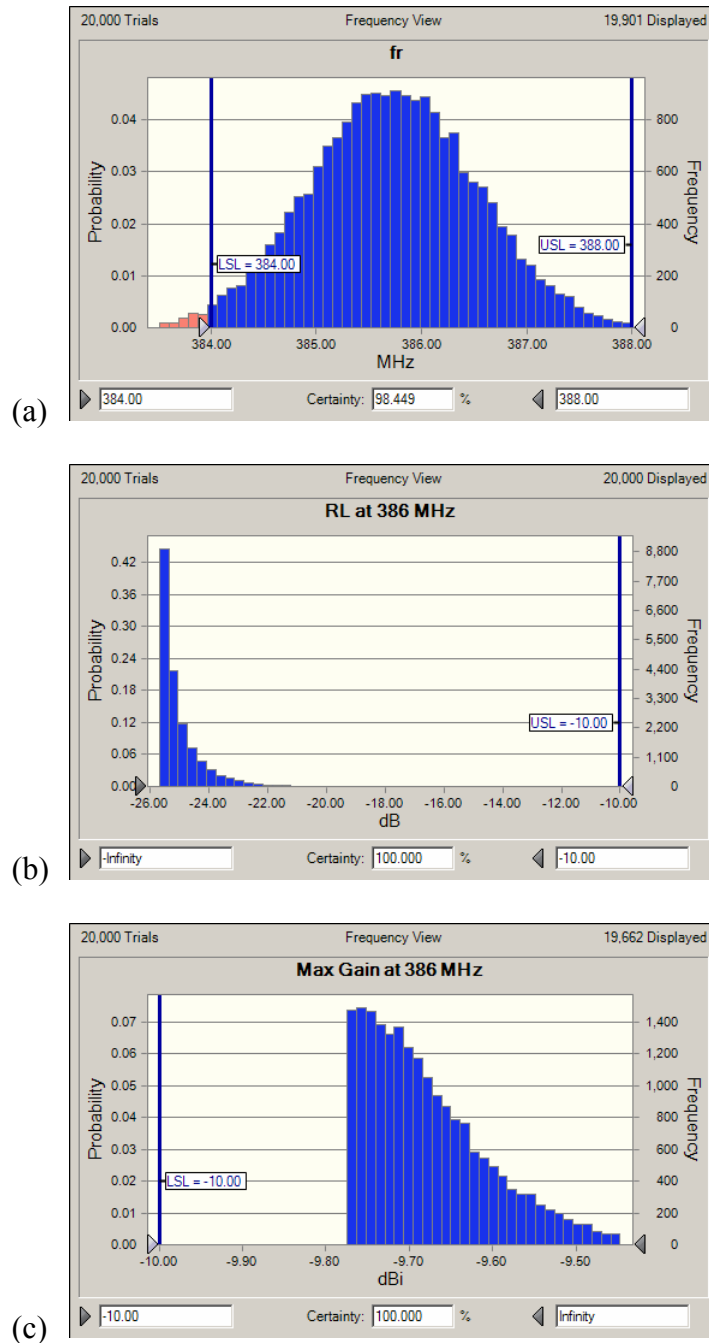


Figure 5.26: Histograms of 20,000 trials for the outputs (a) f_r , (b) RL at 386 MHz, and (c) Maximum Gain at 386 MHz. (a) f_r , Normality test passed with p-value 0.925, (b) RL at 386 MHz Normality test failed with p-value 0.00, and (c) Maximum Gain at 386 MHz Normality test failed with p-value 0.00.

Table 5.18: Summary of Process Specification Limits and Capability Metrics for f_r , RL at 386 MHz, and Maximum Gain at 386 MHz. With $\pm 1\%$ tolerance of the inputs ε' and μ' , f_r is performing at less than 6σ capability with $C_p = 0.84$ and $C_{pk} = 0.73$, RL at 386 MHz is performing at better than 6σ capability with $C_{npk} = 3.74$, and (c) Maximum Gain at 386 MHz is performing at better than 6σ capability with $C_{npk} = 3.88$.

Process Information	f_r	RL at 386 MHz	Max Gain at 386 MHz
Target	386 MHz	not applicable	not applicable
LSL	384 MHz	not applicable	-10 dBi
USL	388 MHz	- 10 dB	not applicable
C_p	0.84	not applicable	not applicable
C_{pk}	0.73	not applicable	not applicable
C_{npk}	not applicable	3.74	3.88

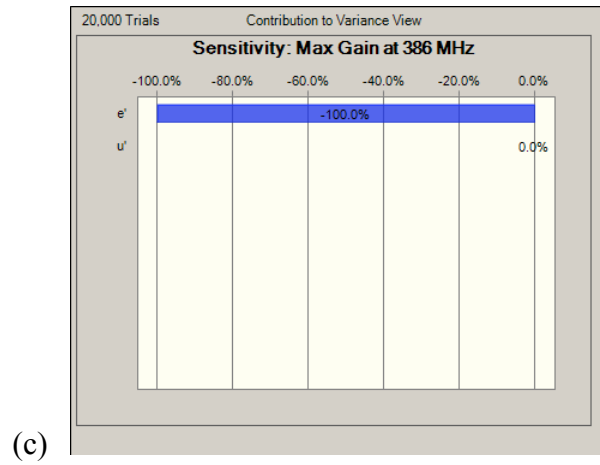
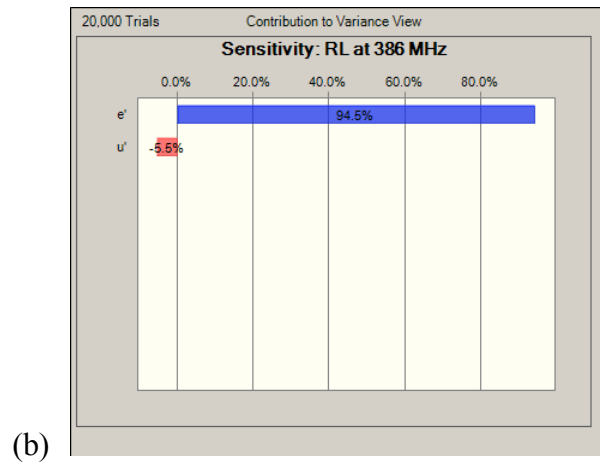
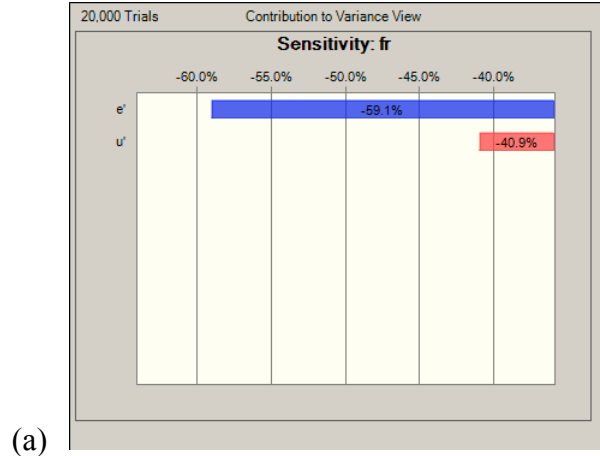


Figure 5.27: Sensitivity charts showing contribution to variance of ϵ' and μ' for the outputs (a) f_r , (b) RL at 386 MHz, and (c) Maximum Gain at 386 MHz

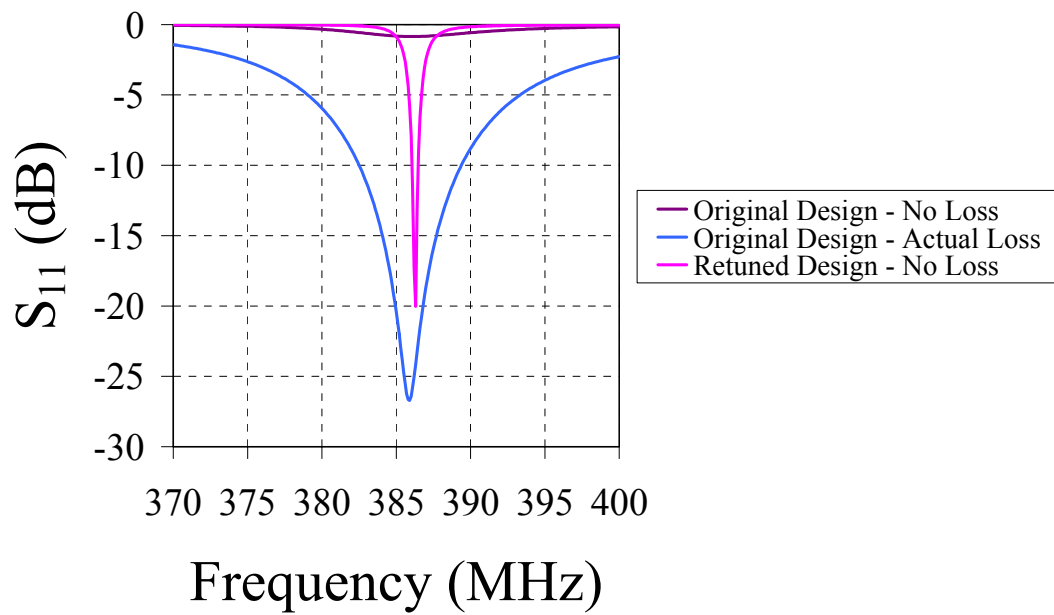


Figure 5.28: S_{11} versus frequency for patch antenna on magnetic composite assuming the original design with no loss ($\tan\delta_\epsilon$ and $\tan\delta_\mu$ equal to zero), the original design with actual loss ($\tan\delta_\epsilon$ and $\tan\delta_\mu$ equal to measured values), and the retuned design with no loss ($\tan\delta_\epsilon$ and $\tan\delta_\mu$ equal to zero)

Discussion

Radiation Pattern Comparisons

The results of the radiation patterns shown in Figures 5.11 and 5.12 do show a discrepancy for $\phi = 90^\circ$ for the simulated antenna on the magnetic composite substrate. In this $\phi = 90^\circ$ measurement, a full back lobe at 180° is shown, whereas it does not exist for both the measured antenna on the magnetic composite substrate and the simulated antenna on the pure silicone substrate. This discrepancy was investigated by simulating the structure in another EM simulation package, CST Microwave Studio version 2006B.03, which gave the same shape shown here. Additionally, another case was run in Ansoft HFSS for which the product of ϵ_r and μ_r were input as a new ϵ_r , μ_r and $\tan\delta_\mu$ were set to 1 and 0, respectively, and $\tan\delta_\epsilon$ was left the same, and the same radiation pattern shape shown here was once again obtained. Considering these results and the close agreement of the other simulated and measured figures of merit, the discrepancy in the radiation patterns is attributed to the limitation of the software to model the combined high ϵ_r and μ_r case.

Antenna Performance Comparison

The close agreement of results for f_r and RL shown in Table 5.3 for all three cases provides a good foundation on which the other figures of merit can be compared in order to assess differences that may be attributable to addition of the magnetic material. One mostly expected result is the increased bandwidth that was obtained for the patch antenna on the magnetic composite substrate due to the increase in ϵ^* and μ^* , which included increase in the dielectric and magnetic losses. The maximum gain results for the simulated and measured patch antenna on the magnetic composite substrate are in good agreement. The decrease in the maximum gain for the patch antenna on the magnetic composite substrate compared to

the pure silicone substrate may be attributable to both the addition of dielectric and magnetic losses as well as the decrease in the patch size. For these performance tradeoffs, the capability for miniaturization is demonstrated to be 2.4X (i.e., 425/180~2.4) for applying the developed magnetic composite.

The tradeoff of the antenna performance determined here for the capability of miniaturization can be useful in some applications. Applications that warrant miniaturization, increased bandwidth, and lower maximum gain do exist in or near the lower UHF spectrum. For example, indoor location technology and some other ad hoc networks require high directivity for device-to-device isolation [99]. Other possible applications include wireless health monitoring and pharmaceutical drug tracking, which require small size, lightweight conformal antennas.

Antenna Performance Capability

For the study on effects of material variation on antenna performance, the relatively larger effect of ϵ' on all figures of merit f_r , RL at 386 MHz, and Maximum Gain at 386 MHz is notable. Both ϵ' and μ' were included in the models for f_r and RL at 386 MHz, and only ϵ' was included in the model for Maximum Gain at 386 MHz. The inputs ϵ' and μ' contributed almost equally, with ϵ' having a slightly larger effect, at 59.1% and 40.9%, respectively, to the variation in f_r . For RL at 386 MHz, ϵ' had a much greater contribution, specifically ϵ' and μ' contributed 94.5% and 5.5%, respectively, to the variation in RL at 386 MHz. For Maximum Gain at 386 MHz, ϵ' contributed 100% to the variation in Maximum Gain at 386 MHz, which was expected since the model developed for Maximum Gain at 386 MHz included dependence on ϵ' alone.

A major finding of the third chapter in this work was that large variation of ϵ^* can be observed due to the purity of the Z-phase in the BaCo ferrite. In the third chapter, it was noted that the formulation process of the BaCo ferrite must enable complete and correct conversion to obtain the targeted pure Z-phase. Taking together the relatively larger effect of ϵ' on the antenna figures of merit and that ϵ^* depend greatly on the BaCo ferrite formulation process, the implication is that controlling the variation of ϵ' provides a large opportunity for controlling variation of f_r , RL at 386 MHz, and Maximum Gain at 386 MHz.

A practical note on the study on effects of material variation on antenna performance is that the RL at 386 MHz is arguably the most important figure of merit of the three studied. In practical antenna design, matched bandwidth can be considered any RL less than -10 dB at the targeted operating frequency. Therefore, because the RL at 386 MHz was found to be 6σ capable with a USL of -10 dB, this antenna design demonstrated 6σ performance with the assumed $\pm 1.0\%$ variation of ϵ' and μ' .

Conclusions

The capability of miniaturization by a factor of 2.4X was demonstrated for a patch antenna structure on a mechanically flexible magnetic composite substrate when compared to a pure silicone substrate. Differences in performance of the antennas included increased bandwidth and reduced gain, both of which were attributed in part to the increase in the dielectric and magnetic losses. These differences can be either beneficial or detrimental, depending on the design motivation, and, in effect, provide further flexibility in radio frequency (RF) system design. A key finding of this study was that a small amount of permeability ($\mu_r \sim 2.5$) can provide relatively substantial capability for miniaturization, while sufficiently low magnetic loss can be introduced for successful application at the targeted

operating frequency. This magnetic composite shows the capability to fulfill this balance and to be a feasible option for RFID applications in the lower UHF spectrum (~300-500 MHz). Another key finding was that controlling the variation of ϵ' provides a large opportunity for controlling variation of f_r , RL at 386 MHz, and Maximum Gain at 386 MHz.

CHAPTER VI: CONCLUSIONS AND FUTURE RECOMMENDATIONS

In the chapter on characterization of magnetic particles, the main purpose was to characterize the ferrite powders in terms of structure and permittivity, which is a critical material property for antenna applications. The ferrite powders targeted for this work were a cubic ferrite and a hexagonal ferrite, which were supplied by separate manufacturers. The cubic spinel ferrite was a NiZn ferrite. The hexagonal ferrite was a Z-phase BaCo ferrite from the ternary $\text{BaO} \cdot \text{MeO} \cdot \text{Fe}_2\text{O}_3$ system, which may also be properly referred to as Co_2Z and Z-phase Co hexaferrite. It was cited that NiZn ferrites can have applicability up to 200 MHz, whereas Z-phase BaCo ferrite show applicability to the lower UHF spectrum (~300-500 MHz). A major finding of this chapter was that both the structure and the permittivity property for one batch of the BaCo ferrite, specifically the BaCo Ferrite 02 batch, was different than the other batches of BaCo ferrite. The observed structure difference detected by XRD was linked to the permittivity results. The strong dependence of ϵ' on frequency and higher ϵ' and ϵ'' values across the frequency sweep were attributed to this batch having less pure Z-phase compared to the other batches. Additionally, the BaCo ferrite batch with a particle size distribution that included larger particles (that is, BaCo Ferrite 02L) showed dielectric relaxation within the frequency sweep. The observed decreased purity provided evidence that the process did not completely or correctly convert all materials to the targeted Z-phase. The mechanism for the observed permittivity behavior of the BaCo Ferrite 02 batch was proposed to be polarons produced from availability of reduced species, such as Fe^{2+} , Co^{2+} , and Ba^{2+} , due to the relatively lower O-content in the compound. For this work, the favored properties for the antenna application in the lower UHF spectrum (~300-500

MHz) include constant ϵ' values up to and over the targeted operating frequency range, low and constant ϵ'' values up to and over the targeted operating frequency range, and the dielectric relaxation to occur at frequencies well above the targeted operating frequency range. The NiZn Ferrite 01, BaCo Ferrite 01, and BaCo Ferrite 04 batches demonstrated these favorable permittivity properties.

In the chapter on formulation and characterization of magnetic composites, the main purpose was to formulate magnetic composites with optimum electromagnetic properties and low loss by a combination of three approaches. The approaches included formulating magnetic composites and characterizing both ϵ^* and μ^* as a function of frequency to determine (1) the optimum ferrite for the targeted operating frequency, (2) the effect of functionalizing the ferrite particles with silane as part of the composite formulation process, and (3) the effect of ferrite particle size distribution. For their application to antenna design, the favored behavior of the magnetic composites is constant ϵ^* and μ^* properties with frequency, extending to the targeted operating frequency, and low loss quantified by ϵ'' , $\tan\delta_\epsilon$, μ'' , and $\tan\delta_\mu$. The magnetic composites were comprised of 40 vol% ferrite particles in a silicone matrix. A major finding of this chapter was that the magnetic composite properties were largely dominated by the bulk properties of the ferrite filler. In particular, the ϵ^* properties measured for the composite closely mimic those for the ferrite from which they are made and as observed in the previous chapter. Additionally, any effect due to treating the ferrite filler with silane in the composite formulation process was not detectable, which further supports that the ϵ^* and μ^* properties of the composites were dominated more by the bulk properties of the ferrite filler compared to the filler-matrix interface. The effect of the ferrite particle size distributions of 45-150 μm and 45-250 μm were statistically compared,

and it was found that the 45-250 μm particle size distribution of gave larger values of ϵ' , μ' , $\tan\delta_\epsilon$, and $\tan\delta_\mu$ than the 45-150 μm particle size distribution at the 95% confidence level. It is likely that the larger particle sizes preserved a larger proportion of domains, providing higher values of μ' . These results support the previously stated approach for this work, which is to use particle sizes that are sufficiently large in order to not disrupt the magnetic domains, therefore avoiding undesirable hysteresis loss and preserving μ_r values. To continue onto the antenna application study, candidate materials for the antenna application in the targeted lower UHF spectrum ($\sim 300\text{-}500$ MHz) were identified to be the BaCo Ferrite 01 and BaCo Ferrite 04 composites.

In the chapter on antenna EM simulation and evaluation, the main purpose was to investigate the antenna performance and miniaturization capability attributable to the developed flexible magnetic composite and feasibility of applying the developed material to the lower UHF spectrum ($\sim 300\text{-}500$ MHz). This investigation was carried out by designing patch antenna structures on both pure silicone and the developed magnetic composite and then comparing their performance. The developed magnetic composite was comprised of ferrite particles from the BaCo Ferrite 04 batch in a matrix of silicone. Additionally, the effects of material property variation on antenna performance were also studied. The results in the chapter showed the capability of miniaturization by a factor of 2.4X for a patch antenna structure on a mechanically flexible magnetic composite substrate when compared to a pure silicone substrate. Differences in performance of the antennas included increased bandwidth and reduced gain, both of which were attributed in part to the increase in the dielectric and magnetic losses. These differences can be either beneficial or detrimental, depending on the design motivation, and, in effect, provide further flexibility in radio

frequency (RF) system design. A key finding of this study was that a small amount of permeability ($\mu_r \sim 2.5$) can provide relatively substantial capability for miniaturization, while sufficiently low magnetic loss can be introduced for successful application at the targeted operating frequency. The developed magnetic composite showed the capability to fulfill this balance and to be a feasible option for RFID applications in the lower UHF spectrum (~ 300 -500 MHz). Another key finding was that controlling the variation of ϵ' provides a large opportunity for controlling variation of f_r , RL at 386 MHz, and Maximum Gain at 386 MHz. This last finding complements a finding of the previous chapter, in which it was observed that ϵ' for the BaCo ferrite can be highly variable due to its dependence on the formulation process. Taking these two findings together, the implication is that the formulation process can be a major source for controlling the variation of the ϵ' and, therefore, the variation of antenna performance.

The most important future recommendation is for material and electrical engineering to work together for co-design of materials and RF structures. By working together, limitations of materials and RF design can be understood and opportunities for use and improvement can be identified. To practical use this material in RF design, the magnetic composite and formulation process would have to be further characterized for mass production in order to control the critical properties. Further characterization could include investigating effects of silane and titanate on both mechanical and electromagnetic properties of the magnetic composite. It is possible that the effects of silane in this study were not detectable because of the high loading of ferrite powder in the silicone matrix. With respect to RF design, the effect of both dielectric and magnetic loss, namely $\tan\delta_\epsilon$ and $\tan\delta_\mu$, can be further quantified with use of statistical tools and methods, as done for ϵ' and μ' in this work. Additionally,

with further optimization, the composite could be made thinner for additional mechanical flexibility and as a laminate for enhancing processability. Electrical engineers would have to work with material engineers to successfully include the magnetic composite in their RF designs. A materials engineer involved in the characterization of the magnetic composite could provide guidance on the material limitations, such as upper operating frequency. The attempt to apply the magnetic composite at a frequency at which it can not efficiently operate and generates excessive magnetic and dielectric losses will prohibit a successful RF design. Without materials understanding, the electrical engineers could possibly overlook use the magnetic composite material in their RF designs. The proper application, as guided by the knowledgeable materials engineer, could prevent this oversight and drive successful implementation of the magnetic composite into standard use.

APPENDIX A

Author's Awards, Honors, Patents, and Publications

Awards and Honors

Invited speaker at IEEE Microwave Theory and Techniques Society (MTT-S) International Microwave Symposium (IMS) Workshop in Atlanta, Georgia, June 2008

Motorola Women's Business Council Peer Award for Excellence in Leadership, March 2008

Invited speaker at the Monie Ferst Award Symposium in honor of award recipient Dr. C. P. Wong in Atlanta, Georgia, September 2007

Invited Speaker at Society of Plastics Engineers, South Florida Chapter Meeting in Fort Lauderdale, Florida, January 2007

IEEE Components, Packaging and Manufacturing Technology (CPMT) Outstanding Young Engineer Award, May 2005

Elected to The Georgia Institute of Technology Council of Outstanding Young Engineering Alumni, November 2004

Invited speaker at Motorola Science Advisory Board Fall Meeting, October 2003

Motorola Six Sigma Master Black Belt - 17th Certified Master Black Belt in the Corporation, August 2003

Inducted as Motorola Science Advisory Board Associate Member (representing one of the top 1.5% of Motorola's top technical resources), April 2003

Motorola Six Sigma Black Belt Steering Committee Member, January 2003

Motorola University Certified Instructor, March 2002

Cover Story in Industry Publication *PC Fab*, January 2002

Invited Speaker at IPC Expo Technical Conference in Anaheim, California, April 2001

Motorola Six Sigma Black Belt, January 2001

Motorola Distinguished Students Program Participant for M.S. Degree, 1998-2000

Scholarship Recipient of Motorola Summer Student Achievement Award, 1993

Patents

“Communication Device Having a Reduced Level of Hazardous Substances,” U.S. patent number 5,933,765

“Method of Rapidly Charging a Lithium Ion Cell,” U.S. patent number 5,481,174

Publications

Lara J. Martin, S.L. Ooi, Daniela Staiculescu, Michael D. Hill, Haiying Li, C. P. Wong, and Manos M. Tentzeris, “Effect of Permittivity and Permeability of a Flexible Magnetic Composite Material on the Performance and Miniaturization Capability of Planar Antennas for RFID and Wearable Wireless Applications,” *IEEE Transactions on Components, Packaging, and Manufacturing Technology*, to be submitted.

Li Yang, Lara J. Martin, Daniela Staiculescu, C. P. Wong, and Manos M. Tentzeris, “Comprehensive Study on the Impact of Dielectric and Magnetic Loss on Performance of a Novel Flexible Magnetic Composite Material,” *38th European Microwave Conference*, Amsterdam, The Netherlands; October (2008); submitted.

Lara J. Martin, Li Yang, Daniela Staiculescu, Haiying Li, S.L. Ooi, C. P. Wong, and Manos M. Tentzeris, “Investigation of the Impact of Magnetic Permeability and Loss of Magnetic Composite Materials on RFID Miniaturization for Conformal Medical Applications,” *International Journal of Numerical Modeling*; submitted.

Li Yang, Lara J. Martin, Daniela Staiculescu, C.P. Wong, and Manos M. Tentzeris, “Design and Development of Compact Conformal RFID Antennas Utilizing Novel Flexible Magnetic Composite Materials for Wearable RF and Biomedical Applications,” *2008 IEEE International Symposium on Antennas and Propagation*, San Diego, California; July (2008); submitted.

Li Yang, Lara J. Martin, Daniela Staiculescu, C. P. Wong, and Manos M. Tentzeris, “A Novel Flexible Magnetic Composite Material for RFID, Wearable RF and Bio-monitoring Applications,” *2008 IEEE MTT-S International Microwave Symposium*, Atlanta, Georgia; June (2008); submitted.

Daniela Staiculescu, Lara J. Martin, C.P. Wong, and Manos M. Tentzeris, “Study of Metamaterial Miniaturization Using Magnetic Composites,” *24th International Review of Progress in Applied Computational Electromagnetics*, Niagara Falls, Canada; March-April (2008); submitted.

Chisang You, Daniela Staiculescu, Lara J. Martin, and Manos M. Tentzeris, “A Novel Hybrid Electrical/Mechanical Optimization Technique Using Time-Domain Modeling, Finite Element Method and Statistical Tools for the Co-Design and Optimization of RF Integrated

Mechanical Structures,” *International Journal of Numerical Modeling*, Vol. 21, No. 1-2, (2008), pp. 91-101.

Lara J. Martin, Daniela Staiculescu, Haiying Li, S. L. Ooi, C. P. Wong, and Manos M. Tentzeris, “Magnetic Nanocomposite Materials for RFID and RF Passives Miniaturization,” *2007 IEEE International Symposium on Antennas and Propagation*, Niigata, Japan; August (2007).

Lara J. Martin, Daniela Staiculescu, Haiying Li, S. L. Ooi, C. P. Wong, and Manos M. Tentzeris, “Investigation of the Impact of Magnetic Permeability and Loss of Magnetic Composite Materials on RFID and RF Passives Miniaturization,” *2007 IEEE Workshop on Computational Electromagnetics in Time-Domain*, Perugia, Italy; October (2007); pp.1-4.

Gerald DeJean, Daniela Staiculescu, Lara J. Martin, U. Onyewuchi, R.L. Li, and Manos M. Tentzeris, “Hybrid Statistical/Electromagnetic Optimization and Performance Capability Modeling of an LTCC Compact Soft/Hard Surface Structure,” *2007 IEEE International Symposium on Antennas and Propagation*, Honolulu, Hawaii; June (2007); pp. 5749-5752.

Francesco Placentino, Daniela Staiculescu, Symeon Nikolaou, Lara J. Martin, Andrea Scarponi, Federico Alimenti, Luca Roselli, and Manos M. Tentzeris, “Concurrent Circuit-Level/System-Level Optimization of a 24 GHz Mixer for Automotive Applications Using a Hybrid Electromagnetic/Statistical Technique,” *2007 IEEE MTT-S International Microwave Symposium*, Honolulu, Hawaii; June (2007); pp. 1217-1220.

Daniela Staiculescu, Lara J. Martin, and Manos M. Tentzeris, “Performance Capability Modeling And Optimization Of RF/Millimeter Wave Integrated Functions And Modules Using A Hybrid Statistical/Electromagnetic Technique That Includes Process Variations,” *36th European Microwave Conference*, Manchester, United Kingdom; September (2006); pp. 474-477.

Daniela Staiculescu, Lara J. Martin, and Manos M. Tentzeris, “Multilayer Embedded Metamaterial Optimization for 3D Integrated Module Applications,” *2006 IEEE International Symposium on Antennas and Propagation*, Albuquerque, New Mexico; July (2006); pp. 4137-4140.

Chisang You, Daniela Staiculescu, Lara J. Martin, Woonbong Hwang, and Manos M. Tentzeris, “Efficient Co-design of Composite Smart Structures (Antennas and Mechanical Structures) Using a Novel Hybrid Optimization Technique,” *2006 IEEE International Symposium on Antennas and Propagation*, Albuquerque, New Mexico; July (2006); pp. 569-572.

Daniela Staiculescu, Chisang You, Lara J. Martin, Woonbong Hwang, and Manos M. Tentzeris, “Hybrid Electrical/Mechanical Optimization Technique Using Time-Domain Modeling, Finite Element Method and Statistical Tools for Composite Smart Structures,” *2006 IEEE MTT-S International Microwave Symposium*, San Francisco, California; June (2006); pp.288-291.

Daniela Staiculescu, Lara J. Martin, and Manos M. Tentzeris, "40 GHz Metamaterial Development Using Hybrid Electromagnetic/Statistical Tools," *2005 IEEE Workshop on Computational Electromagnetics in Time-Domain*, Atlanta, Georgia; September (2005); pp. 110-113.

Lara J. Martin, Daniela Staiculescu, and Manos M. Tentzeris, "Design and Optimization of 3D Multilayer Balun Architectures Using the Design of Experiments Technique," *2005 IEEE International Symposium on Antennas and Propagation*, Washington, D. C.; July (2005); pp. 93-96.

Daniela Staiculescu, Lara J. Martin, Nathan Bushyager, and Manos M. Tentzeris, "Design of Millimeter-Wave Metamaterials Using Deterministic Full Wave Electromagnetic Simulators and Path of Ascent Statistical Optimizer," *55th IEEE Electronic Components and Technology Conference*, Lake Buena Vista, Florida; May-June (2005); pp. 1565-1568.

Daniela Staiculescu, Nathan Bushyager, A. Obatoyinbo, Lara J. Martin, and Manos M. Tentzeris, "Design and Optimization of 3-D Compact Stripline and Microstrip Bluetooth/WLAN Balun Architectures Using the Design of Experiments Technique," *IEEE Transactions on Antennas and Propagation*, Vol. 53, Issue 5, (2005), pp. 1805-1812.

Nathan Bushyager, Daniela Staiculescu, A. Obatoyinbo, Lara J. Martin, and Manos M. Tentzeris, "Optimization of 3D Multilayer RF Components Using the Design of Experiments (DOE) Technique," *2005 IEEE MTT-S International Microwave Symposium*, Long Beach, California; June (2004); pp. 1859-1862.

Nathan Bushyager, Daniela Staiculescu, Lara J. Martin, J.-H. Lee, N. Vasiloglou, and Manos M. Tentzeris, "Design and Optimization of 3D RF Modules, Microsystems and Packages Using Electromagnetic, Statistical and Genetic Tools [mm-Wave Interdigitated Passband Filter Application], *54th IEEE Electronic Components and Technology Conference*, Las Vegas, Nevada; June (2004); pp. 1412-1415.

Nathan Bushyager, Daniela Staiculescu, Lara J. Martin, J.-H. Lee, N. Vasiloglou, and Manos M. Tentzeris, "Fast Hybrid Electromagnetic/Statistical Approach for Design and Optimization of RF Systems and Packages, *9th IEEE International Symposium on Advanced Packaging Materials: Processes, Properties and Interfaces*, Atlanta, Georgia; March (2004); pp. 107-111.

Nathan Bushyager, Lara J. Martin, S. Khushrushahi, Serkan Basat, and Manos M. Tentzeris, "Design of RF and Wireless Packages Using Fast Hybrid Electromagnetic/Statistical Methods, *53rd IEEE Electronic Components and Technology Conference*, New Orleans, Louisiana; May (2003); pp. 1546-1549.

Lara J. Martin and John Frei, "Forecasting Supply Chain Components with Time Series Analysis," *53rd IEEE Electronic Components and Technology Conference*, New Orleans, Louisiana; May (2003); pp. 269-278.

Lara J. Martin and John Frei, "Application of Statistical Tools and Methods for High Density Substrate Process Development," *52nd IEEE Electronic Components and Technology Conference*, San Diego, California; May (2002); pp. 690-699.

Lara J. Martin and C. P. Wong, "Chemical and Mechanical Adhesion Mechanisms of Sputter-Deposited Metal on Epoxy Dielectric for High Density Interconnect Printed Circuit Boards," *PC Fab*, CMP United Business Media, January (2002); pp. 18-34.

Lara J. Martin and C. P. Wong, "Chemical and Mechanical Adhesion Mechanisms of Sputter-Deposited Metal on Epoxy Dielectric for High Density Interconnect Printed Circuit Boards," *IEEE Transactions on Components, Packaging, and Manufacturing Technology*, Vol. 24, No. 3 (2001), pp. 416-424.

Lara J. Martin and C. P. Wong, "Sputter-Deposited Metallization System for Fine Feature High Density Interconnect Printed Circuit Boards," *IPC Expo 2001*, Anaheim, California; April (2001); pp. S16-4-1 to S16-4-14.

Kevin Arledge and Lara J. Martin, "Statistical Tools and Engineering Judgment: A Photolithographic Process Development Case Study," *Motorola 2000 Hermes Symposium*, Fort Lauderdale, Florida; October (2000).

Lara J. Martin, "Adhesion Mechanisms of Sputter-Deposited Metal on Epoxy Dielectric for Fine Feature High Density Interconnect Printed Circuit Boards," *Motorola 2000 Hermes Symposium*, Fort Lauderdale, Florida; October (2000).

Lara J. Martin and C. P. Wong, "Study on Metal Adhesion Mechanisms in High Density Interconnect Printed Circuit Boards," *50th IEEE Electronic Components and Technology Conference*, Las Vegas, Nevada; May (2000); pp. 549-557.

Brian Lee, Roger Callanan, Kevin Pieper, Mark Newton, Tom Swirbel, Lynn Davis, Lara J. Martin, and Rob Mulligan, "Evaluation of FRN Non-Brominated PCB Board Material," *1997 Motorola Winter AMT Symposium*, Tempe, Arizona; January (1997).

REFERENCES

1. Klaus Finkenzeller, RFID Handbook, 2nd ed., John Wiley & Sons Inc. (New Jersey, 2003), pp. 2-7.
2. Steven Shepard, RFID Radio Frequency Identification, McGraw-Hill (New York, 2005), pp. 52-53.
3. Steven Shepard, RFID Radio Frequency Identification, McGraw-Hill (New York, 2005), p. 41.
4. Klaus Finkenzeller, RFID Handbook, 2nd ed., John Wiley & Sons Inc. (New Jersey, 2003), pp. 161-166.
5. Steven Shepard, RFID Radio Frequency Identification, McGraw-Hill (New York, 2005), pp. 61-63.
6. Klaus Finkenzeller, RFID Handbook, 2nd ed., John Wiley & Sons Inc. (New Jersey, 2003), pp. 22-24.
7. Manish Bhuptani and Shahram Moradpour, RFID Field Guide: Deploying Radio Frequency Identification Systems, Prentice Hall (New Jersey, 2005), p. 142.
8. <http://www.netcaucus.org/events/2005/rfid/demonstrators.shtml>, "Demonstrators at the 2005 ICAC RFID Exhibition & Policy Primer," Advisory Committee to the Congressional Internet Caucus; (accessed May 31, 2005).
9. <http://www.networkworld.com/news/2004/112904walmart.html>, Ann Bednarz, "Leeway found in Wal-Mart's RFID mandate," Network World: Research Center: Wireless/Mobile, November 29, 2004; (accessed June 24, 2005).
10. http://www.atmel.com/dyn/resources/Prod_documents/secref_largemem_3_04.pdf, David Dressen, "Large Memory RFID System Solutions," Atmel Application Journal, pp. 48-49; (accessed May 31, 2005).
11. http://www.tdk.co.jp/tf2005/pdf_e/2f0215e.pdf, "Magnetic Materials for RFID," TechnoForum 2005, TDK; (accessed June 26, 2005).
12. James Masi and William Thibault, "New, High Frequency Transformer Topologies," *Electrical Electronics Insulation Conference and Electrical Manufacturing and Coil Winding Conference*, Rosemont, Illinois, September (1995); pp. 157-161.

13. N. Das and A. K. Ray, "Magneto Optical Technique for Beam Steering by Ferrite Based Patch Arrays," *IEEE Transactions on Antennas and Propagation*, Vol. 49, No. 8, (2001); pp. 1239-1241.
14. W. A. Roshen, C. S. Korman, and W. Daum, "Embedded Magnetics for Integrated Power," *35th Annual IEEE Power Electronics Specialists Conference*, Aachen, Germany, June (2004); pp. 2467-2473.
15. www.legco.gov.hk/yr07-08/english/panels/itb/papers/itb1210cb1-383-4-e.pdf, "Frequency Allocation for Radio Frequency Identification Equipment (II) – For Discussion on 16 May 2007," Office of the Telecommunications Authority (OFTA), Hong Kong Special Administrative Region; (accessed January 4, 2008).
16. Klaus Finkenzeller, *RFID Handbook*, 2nd ed., John Wiley & Sons Inc. (New Jersey, 2003), p. 47.
17. Manish Bhuptani and Shahram Moradpour, *RFID Field Guide: Deploying Radio Frequency Identification Systems*, Prentice Hall (New Jersey, 2005), pp. 39-40.
18. Klaus Finkenzeller, *RFID Handbook*, 2nd ed., John Wiley & Sons Inc. (New Jersey, 2003), p. 41.
19. Klaus Finkenzeller, *RFID Handbook*, 2nd ed., John Wiley & Sons Inc. (New Jersey, 2003), p. 47.
20. Jong-Sung Kim, Kwang-Ho Shin, Seung-Mo Park, Won-Kyu Choi, and Nak-Seon Seong, "Polarization and Space Diversity Antenna Using Inverted-F Antennas for RFID Reader Applications," *IEEE Antennas and Wireless Propagation Letters*, Vol. 5, (2006); pp. 265-268.
21. Klaus Finkenzeller, *RFID Handbook*, 2nd ed., John Wiley & Sons Inc. (New Jersey, 2003), pp. 112-114.
22. S. Cichos, J. Haberland, and H. Reichl, "Performance Analysis of Polymer Based Antenna-Coils for RFID," *2nd International IEEE Conference on Polymers and Adhesives in Microelectronics and Photonics - Polytronic*, Zalaegerszeg, Hungary, June (2002); pp. 120-124.
23. Klaus Finkenzeller, *RFID Handbook*, 2nd ed., John Wiley & Sons Inc. (New Jersey, 2003), pp. 14-16.
24. Klaus Finkenzeller, *RFID Handbook*, 2nd ed., John Wiley & Sons Inc. (New Jersey, 2003), pp. 18-21.

25. Chris Bowick, RF Circuit Design, Butterworth-Heinemann (Boston, 1982), pp. 18-20.
26. <http://ww1.microchip.com/downloads/en/DeviceDoc/21299E.pdf>, “microID® 13.56 MHz RFID System Design Guide,” Microchip Technology Inc., Chandler, 2004, pp. 113-118; (accessed June 26, 2005).
27. Klaus Finkenzeller, RFID Handbook, 2nd ed., John Wiley & Sons Inc. (New Jersey, 2003), pp. 108-109.
28. J. Y. Park and M. G. Allen, “Low Temperature Fabrication and Characterization of Integrated Packaging-Compatible, Ferrite Core Magnetic Devices,” *Proceedings of the Applied Power Electronics Conference and Exposition Conference*, Atlanta, Georgia, February (1997); pp. 361-367.
29. C. K. Liu, T. W. Law, P. L. Cheng, I. T. Chong, and David C. C. Lam, “Low Temperature Processing and Electrical Properties of Embedded Ferrite-cored Inductor,” 52nd *IEEE Electronic Components and Technology Conference*, San Diego, California, May (2002); pp. 490-494.
30. C. K. Liu, P. L. Cheng, T. W. Law, I. T. Chong, and David C. C. Lam, “Development of Low Temperature Processable Core Material for Embedded Inductor,” 2nd *International IEEE Conference on Polymers and Adhesives in Microelectronics and Photonics - Polytronic*, Zalaegerszeg, Hungary, June (2002); pp. 104-109.
31. Chris Bowick, RF Circuit Design, Butterworth-Heinemann (Boston, 1982), p. 36.
32. Chris Bowick, RF Circuit Design, Butterworth-Heinemann, (Boston, 1982) p. 31.
33. S. Basat, K. Lim, I. Kim, M. M. Tentzeris, and J. Laskar, “Design and Development of a Miniaturized Embedded UHF RFID Tag for Automotive Tire Applications,” 55th *IEEE Electronic Components and Technology Conference*, Lake Buena Vista, Florida, May (2005); pp. 867-870.
34. Constantine Balanis, Antenna Theory: Analysis and Design, 3rd ed., John Wiley & Sons Inc. (New Jersey, 2005), p. 811.
35. Constantine Balanis, Antenna Theory: Analysis and Design, 3rd ed., John Wiley & Sons Inc. (New Jersey, 2005), p. 191.
36. Sri Das and Santosh Chowdhury, “Rectangular Microstrip Antenna on a Ferrite Substrate,” *IEEE Transactions on Antennas and Propagation*, Vol. AP-30, No. 3, (1982); pp. 499-502.

37. Junho Yeo, Raj Mittra, and Sourav Chakravarty, "A GA-based Design of Electromagnetic Bandgap (EBG) Structures Utilizing Frequency Selective Surfaces for Bandwidth Enhancement of Microstrip Antennas," *IEEE International Antennas and Propagation Symposium*, San Antonio, Texas, June (2002); pp. 400-403.
38. Junho Yeo, Ji-fu Ma, and Raj Mittra, "Design of Artificial Magnetic Ground Planes (AMGs) Utilizing Frequency Selective Surfaces Embedded in Multilayer Structures with Electric and magnetic Losses," *IEEE International Antennas and Propagation Symposium*, Columbus, Ohio, June (2003); pp. 343-346.
39. A. B. Smolders, "Broadband Microstrip Array Antennas," *IEEE International Antennas and Propagation Symposium*, Seattle, Washington, June (1994); pp. 1832-1835.
40. N. P. Mahalik, "Tuning Procedure in Microstrip Antennas on Ferrite Substrate," *IEEE International Antennas and Propagation Symposium*, Edinburgh, U.K., April (1997); pp. 1.294-1.297.
41. James Schaffer, Ashok Saxena, Stephen Antolovich, Thomas Sanders, Jr., and Steven Warner, The Science and Design of Engineering Materials, 2nd ed., McGraw-Hill (New York, 1999), pp. 523-535.
42. Nicola Spaldin, Magnetic Materials: Fundamentals and Device Applications, Cambridge University Press (Cambridge, U.K., 2003), pp.18-33.
43. Nicola Spaldin, Magnetic Materials: Fundamentals and Device Applications, Cambridge University Press (Cambridge, U.K., 2003), pp.113-119.
44. James Schaffer, Ashok Saxena, Stephen Antolovich, Thomas Sanders, Jr., and Steven Warner, The Science and Design of Engineering Materials, 2nd ed., McGraw-Hill (New York, 1999), pp. 533-535.
45. Erik Brandon, Emily Wesseling, Vincent Chang, and William Kuhn, "Printed Microinductors on Flexible Substrates for Power Applications," *IEEE Transactions on Components and Packaging Technologies*, Vol. 26, No. 3, (2003); pp. 517-523.
46. Jiongxin Lu and C.P. Wong, "Tailored Dielectric Properties of High-k Polymer Composites via Nanoparticle Surface Modification for Embedded Passives Applications," *57th IEEE Electronic Components and Technology Conference*, Reno, Nevada, May-June, (2007); pp. 1033-1039.
47. Jianwen Xu and C.P. Wong, "Dielectric Behavior of Ultrahigh-k Carbon Black Composites for Embedded Capacitor Applications," *55th IEEE Electronic*

- Components and Technology Conference*, Lake Buena Vista, Florida, May, (2005); pp. 1864-1869.
48. Hongjin Jiang, Kyoung-sik Moon, Yi Li, and C.P. Wong, "Ultra High Conductivity of Isotropic Conductive Adhesives," *56th IEEE Electronic Components and Technology Conference*, San Diego, California, May-June, (2006); pp. 485-490.
 49. Nicola Spaldin, Magnetic Materials: Fundamentals and Device Applications, Cambridge University Press (Cambridge, U.K., 2003), pp.136-140.
 50. N.H. Hur, J.Y. Park, J. Dho, S.J. Kim, and E.K. Lee, "Magnetic and Microstructural Properties on Mn- and Ru-Doped Hexagonal Barium Ferrites," *IEEE Transactions on Magnetics*, Vol. 40, No. 4, (2004); pp. 2790-2792.
 51. Tetsuji Inui and Naoyuki Ogasawara, "Grain-Size Effects on Microwave Ferrite Magnetic Properties," *IEEE Transactions on Magnetics*, Vol. MAG-13, No. 6, (1977); pp. 1729-1744.
 52. Shannon Morrison, Christopher Cahill, Everett Carpenter, Scott Calvin, Raja Swaminathan, Michael McHenry, and Vincent Harris, "Magnetic and Structural Properties of Nickel Zinc Ferrite Nanoparticles Synthesized at Room Temperature," *Journal of Applied Physics*, Vol. 95, No. 11, (2004); pp. 6392-6395.
 53. Hai Dong, Fuhan Liu, Qing Song, Z. John Zhang, and C. P. Wong, "Magnetic Nanocomposite for High Q Embedded Inductor," *IEEE International Symposium and Exhibition on Advance Packaging Materials: Process, Properties, and Interfaces*, Atlanta, Georgia, March (2004); pp. 171-174.
 54. Chao-Ming Fu, Yuh-Feng Wang, Yu-Chiang Chao, Shih-Hung Hung, and Ming-Da Yang, "Directly Labeling Ferrite Nanoparticles with Tc-99m Radioisotope for Diagnostic Applications," *IEEE Transactions on Magnetics*, Vol. 40, No. 4, (2004); pp. 3003-3005.
 55. <http://scitation.aip.org/getpdf/servlet/GetPDFServlet?filetype=pdf&id=MAECES000501000001000055000001&idtype=cvips&prog=normal>, T. Kim and M. Shima, "Yttrium Iron Garnet Nanoparticles Synthesized from Aqueous Solution," *207th Electrochemical Society Meeting*, Quebec City, Canada, May (2005); (accessed June 26, 2005).
 56. T. Kim, Teruyoshi Hirano, Yoshitaka Kitamoto, and Yohtaro Yamazaki, "Novel Nanoparticle Milling Process for Bi-YIG Dispersed Transparent Films," *IEEE Transactions on Magnetics*, Vol. 39, No. 4, (2003); pp. 2078-2080.

57. P. Markondeya Raj, Prathap Muthana, T. Danny Xiao, Lixi Wan, Devarajan Balaraman, Isaac Robin Abothu, Swapan Bhattacharya, Madhavan Swaminathan, and Rao Tummala, "Magnetic Nanocomposite for Organic Compatible Miniaturized Antennas and Inductors," *IEEE International Symposium and Exhibition on Advance Packaging Materials: Process, Properties, and Interfaces*, Irvine, California, March (2005); pp. 272-275.
58. J. Gieraltowski and A. Globus, "Domain Wall Size and Magnetic Losses in Frequency Spectra of Ferrites and Garnets," *IEEE Transactions on Magnetics*, Vol. MAG-13, No. 5, (1977); pp. 1357-1359.
59. S. O. Kasap, Principles of Electronic Materials and Devices, 2nd ed., McGraw-Hill (New York, 2002), p. 625.
60. Kevin Buell, Hossein Mosallaei, and Kamal Sarabandi, "A Substrate for Small Patch Antennas Providing Tunable Miniaturization Factors," *IEEE Transactions on Microwave Theory and Techniques*, Vol. 54, No. 1, (2006); pp. 135-146.
61. Michael M. Schieber, Selected Topics in Solid State Physics Series: Experimental Magnetochemistry, Vol. 8, John Wiley & Sons Inc. (New York, 1967), pp. 198-213.
62. James Schaffer, Ashok Saxena, Stephen Antolovich, Thomas Sanders, Jr., and Steven Warner, The Science and Design of Engineering Materials, 2nd ed., McGraw-Hill (New York, 1999), pp. 533-534, 538-539.
63. Nicola Spaldin, Magnetic Materials: Fundamentals and Device Applications, Cambridge University Press (Cambridge, U.K., 2003), pp. 114-115, 119.
64. JCPDS-International Centre for Diffraction Data, PCPDFWIN v. 1.30, Card 08-0234 (NiZn)Fe₂O₄, Nickel Zinc Iron Oxide, (1997).
65. Nicola Spaldin, Magnetic Materials: Fundamentals and Device Applications, Cambridge University Press (Cambridge, U.K., 2003), pp. 114-115.
66. G.H. Jonker, H.P.J. Wijn, and P.B. Braun, "Ferroxplana, Hexagonal Ferromagnetic Iron-Oxide Compounds for Very High Frequencies," *Philips Technical Review*, Vol. 18, No. 6, (1956-1957); pp. 145-154.
67. Hongguo Zhang, Longtu Li, Ji Zhou, Zhenxing Yue, and Xhilun Gui, "Dielectric Characteristics of Cu Modified Z-type Plana Hexaferrite," *12th IEEE International Symposium on Applications of Ferroelectrics*, Vol. 2, Honolulu, Hawaii, July-August (2000); pp. 859-862.

68. L.L. Hench and J.K. West, Principles of Electronic Ceramics, John Wiley & Sons Inc. (New York, 1990), pp. 96-98.
69. C. Kittel, Introduction to Solid State Physics, John Wiley & Sons Inc. (New York, 1976), pp. 312-315.
70. J. J. Went and E. W. Gorter, "The Magnetic and Electrical Properties of Ferrocube Materials," *Philips Technical Review*, Vol. 13, No. 7, (1952); pp. 181-193.
71. Y. C. Hung, W. S. Ko, M. J. Tung, L. K. Chen, and W. C. Chang, "Effects of Additives on the Orientation and Strength of Plastic Ferrite Magnet," *IEEE Transactions on Magnetics*, Vol. 25, No. 5, (1989); pp. 3287-3289.
72. L. Y. Gao, W. Y. Guo, and D. M. Tu, "Interfacial, Microstructure and Withstand Voltage of Polyethylene for Power Cables," *IEEE Transactions on Dielectrics and Electrical Insulation*, Vol. 10, No. 2, (2003); pp. 233 - 239.
73. Xiaohong Zhang, Hengkun Xie, Xiongwei Jiang, Qinggou Chen, and Qingquan Lei, "The Voltage Endurance of Low Density Polyethylene with Surface Treated Inorganic Filler," *International Symposium on Electrical Insulating Materials*, Toyohashi, Japan, September (1998); pp. 215-217.
74. Shengtao Li, Jianying Li, G. Chen, and A. E. Davis, "Interfacial Space Charge Between ZnO Varistor Ceramics and Coating Materials," *IEEE International Symposium on Electrical Insulation and Dielectric Phenomena*, Boston, Massachusetts, April (2002); pp. 478-481.
75. W. Pan, W. Li, L. Y. Cui, X. M. Li, and Z. H. Guo, "Rare Earth Magnets Resisting Eddy Currents," *IEEE Transactions on Magnetics*, Vol. 35, No. 5, (1999); pp. 3343-3345.
76. C. P. Wong and Richard McBride, "Robust Titanate-Modified Encapsulants for High Voltage Potting Application of Multichip Module/Hybrid IC," *IEEE Transactions on Components, Hybrids, and Manufacturing Technology*, Vol. 16, No. 8, (1993); pp. 868-875.
77. JMP Software, Version 6.0.3, SAS Institute, Cary, North Carolina.
78. George E. P. Box, William G. Hunter, and J. Stuart Hunter, Statistics for Experimenters: An Introduction to Design, Data Analysis, and Model Building, John Wiley and Sons (New York, 1978).

79. John Neter, Michael H. Kutner, Christopher J. Nachtsheim, and William Wasserman, Applied Linear Statistical Models, 4th Ed., The McGraw-Hill Companies (Chicago, 1996).
80. Lara J. Martin, Li Yang, Daniela Staiculescu, Haiying Li, S.L. Ooi, C. P. Wong, and Manos M. Tentzeris, "Investigation of the Impact of Magnetic Permeability and Loss of Magnetic Composite Materials on RFID Miniaturization for Conformal Medical Applications," *International Journal of Numerical Modeling*; submitted.
81. Chisang You, Daniela Staiculescu, Lara J. Martin, and Manos M. Tentzeris, "A Novel Hybrid Electrical/Mechanical Optimization Technique Using Time-Domain Modeling, Finite Element Method and Statistical Tools for the Co-Design and Optimization of RF Integrated Mechanical Structures," *International Journal of Numerical Modeling*, Vol. 21, No. 1-2, (2008), pp. 91-101.
82. Lara J. Martin, Daniela Staiculescu, Haiying Li, S. L. Ooi, C. P. Wong, and Manos M. Tentzeris, "Magnetic Nanocomposite Materials for RFID and RF Passives Miniaturization," *2007 International Symposium on Antennas and Propagation*, Niigata, Japan; August (2007).
83. Lara J. Martin, Daniela Staiculescu, Haiying Li, S. L. Ooi, C. P. Wong, and Manos M. Tentzeris, "Investigation of the Impact of Magnetic Permeability and Loss of Magnetic Composite Materials on RFID and RF Passives Miniaturization," *2007 IEEE Workshop on Computational Electromagnetics in Time-Domain*, Perugia, Italy; October (2007); pp. 1-4.
84. Gerald DeJean, Daniela Staiculescu, Lara J. Martin, U. Onyewuchi, R.L. Li, and Manos M. Tentzeris, "Hybrid Statistical/Electromagnetic Optimization and Performance Capability Modeling of an LTCC Compact Soft/Hard Surface Structure," *2007 IEEE International Symposium on Antennas and Propagation*, Honolulu, Hawaii; June (2007); pp. 5749-5752.
85. Francesco Placentino, Daniela Staiculescu, Symeon Nikolaou, Lara J. Martin, Andrea Scarponi, Federico Alimenti, Luca Roselli, and Manos M. Tentzeris, "Concurrent Circuit-Level/System-Level Optimization of a 24 GHz Mixer for Automotive Applications Using a Hybrid Electromagnetic/Statistical Technique," *2007 IEEE MTT-S International Microwave Symposium*, Honolulu, Hawaii; June (2007); pp. 1217-1220.
86. Daniela Staiculescu, Lara J. Martin, and Manos M. Tentzeris, "Performance Capability Modeling And Optimization Of RF/Millimeter Wave Integrated Functions And Modules Using A Hybrid Statistical/Electromagnetic Technique That Includes Process Variations," *36th European Microwave Conference*, Manchester, United Kingdom; September (2006); pp. 474-477.

87. Daniela Staiculescu, Lara J. Martin, and Manos M. Tentzeris, "Multilayer Embedded Metamaterial Optimization for 3D Integrated Module Applications," *2006 IEEE International Symposium on Antennas and Propagation*, Albuquerque, New Mexico; July (2006); pp. 4137-4140.
88. Chisang You, Daniela Staiculescu, Lara J. Martin, Woonbong Hwang, and Manos M. Tentzeris, "Efficient Co-design of Composite Smart Structures (Antennas and Mechanical Structures) Using a Novel Hybrid Optimization Technique," *2006 IEEE International Symposium on Antennas and Propagation*, Albuquerque, New Mexico; July (2006); pp. 569-572.
89. Daniela Staiculescu, Chisang You, Lara J. Martin, Woonbong Hwang, and Manos M. Tentzeris, "Hybrid Electrical/Mechanical Optimization Technique Using Time-Domain Modeling, Finite Element Method and Statistical Tools for Composite Smart Structures," *2006 IEEE MTT-S International Microwave Symposium*, San Francisco, California; June (2006); pp. 288-291.
90. Daniela Staiculescu, Lara J. Martin, and Manos M. Tentzeris, "40 GHz Metamaterial Development Using Hybrid Electromagnetic/Statistical Tools," *2005 IEEE Workshop on Computational Electromagnetics in Time-Domain*, Atlanta, Georgia; September (2005); pp. 110-113.
91. Lara J. Martin, Daniela Staiculescu, and Manos M. Tentzeris, "Design and Optimization of 3D Multilayer Balun Architectures Using the Design of Experiments Technique," *2005 IEEE International Symposium on Antennas and Propagation*, Washington, D. C.; July (2005); pp. 93-96.
92. Daniela Staiculescu, Lara J. Martin, Nathan Bushyager, and Manos M. Tentzeris, "Design of Millimeter-Wave Metamaterials Using Deterministic Full Wave Electromagnetic Simulators and Path of Ascent Statistical Optimizer," *55th IEEE Electronic Components and Technology Conference*, Lake Buena Vista, Florida; May-June (2005); pp. 1565-1568.
93. Daniela Staiculescu, Nathan Bushyager, A. Obatoyinbo, Lara J. Martin, and Manos M. Tentzeris, "Design and Optimization of 3-D Compact Stripline and Microstrip Bluetooth/WLAN Balun Architectures Using the Design of Experiments Technique," *IEEE Transactions on Antennas and Propagation*, Vol. 53, Issue 5, (2005), pp. 1805-1812.
94. Nathan Bushyager, Daniela Staiculescu, A. Obatoyinbo, Lara J. Martin, and Manos M. Tentzeris, "Optimization of 3D Multilayer RF Components Using the Design of Experiments (DOE) Technique," *2005 IEEE MTT-S International Microwave Symposium*, Long Beach, California; June (2004); 1859-1862.

95. Nathan Bushyager, Daniela Staiculescu, Lara J. Martin, J.-H. Lee, N. Vasiloglou, and Manos M. Tentzeris, "Design and Optimization of 3D RF Modules, Microsystems and Packages Using Electromagnetic, Statistical and Genetic Tools [mm-Wave Interdigitated Passband Filter Application], *54th IEEE Electronic Components and Technology Conference*, Las Vegas, Nevada; June (2004); pp. 1412-1415.
96. Nathan Bushyager, Daniela Staiculescu, Lara J. Martin, J.-H. Lee, N. Vasiloglou, and Manos M. Tentzeris, "Fast Hybrid Electromagnetic/Statistical Approach for Design and Optimization of RF Systems and Packages, *9th IEEE International Symposium on Advanced Packaging Materials: Processes, Properties and Interfaces*, Atlanta, Georgia; March (2004); pp. 107-111.
97. Nathan Bushyager, Lara J. Martin, S. Khushrushahi, Serkan Basat, and Manos M. Tentzeris, "Design of RF and Wireless Packages Using Fast Hybrid Electromagnetic/Statistical Methods, *53rd IEEE Electronic Components and Technology Conference*, New Orleans, Louisiana; May (2003); 1546-1549.
98. Crystal Ball Software, Version 7.3, Decisioneering, Denver, Colorado.
99. Gentian Jakllari, Ioannis Broustis, Thanasis Korakis, Srikanth V. Krishnamurthy, and Leandros Tassioulas, "Handling Assymetry in Gain in Directional Antenna Equipped Ad Hoc Networks," *2005 IEEE 16th International Symposium on Personal, Indoor and Mobile Radio Communications*, Berlin, Germany, September (2005); pp. 1284-1288.